PROTON RESONANCE SPECTROSCOPY IN ^{28}Si AND ^{30}P

RONALD OWEN NELSON

Triangle Universities Nuclear Laboratory
Department of Physics
Duke University

1983

PROTON RESONANCE SPECTROSCOPY IN ^{28}Si AND ^{30}P

by

Ronald Owen Nelson

Department of Physics
Duke University

Date: _____

Approved:

_____
E. G. Bilpuch, Supervisor

_____

_____

_____

_____

Dissertation submitted in partial fulfillment of
the requirements for the degree of Doctor
of Philosophy in the Department of
Physics in the Graduate School
of Duke University

1983

ABSTRACT

(Physics-Nuclear)

PROTON RESONANCE SPECTROSCOPY IN ^{28}Si AND ^{30}P

by

Ronald Owen Nelson

Department of Physics
Duke University

Date: _____

Approved:

_____
E. G. Bilpuch, Supervisor

_____

_____

_____

_____

An abstract of a dissertation submitted in partial fulfillment of the requirements for the degree of Doctor of Philosophy in the Department of Physics in the Graduate School of Duke University

1983

ABSTRACT

Excitation functions for proton elastic scattering and for proton induced reactions were measured with the KN Van de Graaff and associated high resolution system at TUNL for two odd-mass targets. Excitation functions for ^{29}Si(p,p), (p,p_1), and (p,p_2) were obtained in the range E_p = 1.29 to 3.30 MeV, and the ^{27}Al(p,p), (p,p_1), (p,p_2), (p,α_0), and (p,α_1) differential cross sections were measured in the range E_p = 0.92 to 3.05 MeV. The data were measured at four angles with an overall resolution that varied between 350 - 450 eV, full width at half maximum.

The measured excitation functions were analyzed with a multi-level, multi-channel R-matrix formalism. The parameters extracted from the data include the resonance energy, total angular momentum, partial elastic and reaction widths, and channel spin and orbital angular momentum mixing ratios. Resonance parameters were determined for 66 resonances in ^{30}P in the range E_x = 6.85 to 8.79 MeV, and for 104 resonances in ^{28}Si in the range E_x = 12.47 to 14.53 MeV. The dependence of the resonance shapes on the channel spin mixing ratio and on the ℓ-mixing ratio was investigated for proton scattering on target nuclei with $J^\pi = \frac{1}{2}^+$ and $\frac{5}{2}^+$.

Seven isobaric analog states were identified in ^{30}P and eighteen analog states were identified in ^{28}Si. Coulomb energies and proton spectroscopic factors were determined and the analog strengths compared with the parent state (d,p) spectroscopic factors.

The proton elastic scattering width of the 6^-, T = 1, stretched state at E_x = 14.36 MeV in ^{28}Si was measured. Results of calculations relating the measured width to the strength of this state in intermediate

energy inelastic scattering are presented.

A precise value of the ℓ-mixing ratio was determined for the 2^+ resonance at $E_p = 1.365$ MeV from a measurement of the $^{27}Al(p,\alpha_0)$ reaction. This measurement is relevant to a previous test of time reversal invariance.

ACKNOWLEDGEMENTS

I would like to thank my adviser, Dr. E.G. Bilpuch, for his unfailing support and encouragement during my graduate studies. I am very grateful to Dr. G.E. Mitchell for his guidance and encouragement, and especially for his assistance in the preparation of this dissertation.

The assistance and patience of C.R. Westerfeldt during the course of these experiments is deeply appreciated. Special thanks are due Dr. J.F. Shriner, Jr. for numerous helpful discussions and for his assistance with the experiments and the typing of this dissertation. The encouragement of Dr. K.B. Sales and fruitful discussions with Dr. W.A. Watson III during the early phases of this research are gratefully acknowledged. The assistance of Dr. K.M. Whatley, Dr. B.H. Chou, P. Ramakrishnan, B.J. Warthen, and J.R. Vanhoy in taking portions of the data is appreciated.

I would like to thank Mr. S.E. Edwards for his help in maintaining the electronics used in these experiments. Thanks go to Mr. R. Rummel and Mr. P. Carter for their help in maintaining the accelerator systems. The superior work of Mr. A.W. Lovette and the instrument shop staff is greatly appreciated. Special thanks are due Mrs. Joseph Bailey for the professional preparation of the figures in this dissertation.

I would especially like to thank G. Adams and J. Adams for their help in typing portions of this dissertation. Without their help I would never have finished on time. The moral support of G. Mitev and B. Haas, especially during the past month, is also appreciated.

To my parents I offer my sincere appreciation for their support and guidance throughout my life.

This work was supported in part by the United States Department of Energy.

TABLE OF CONTENTS

ABSTRACT iii

ACKNOWLEDGEMENTS v

LIST OF FIGURES ix

LIST OF TABLES xiv

I. INTRODUCTION 2

II. R-MATRIX THEORY AND ANGULAR CORRELATION THEORY 5

A. Introduction 5

B. R-matrix Theory 7

C. Properties of the Angular Distributions of Reaction Products 19

III. EXPERIMENTAL EQUIPMENT AND PROCEDURES 21

A. The KN Van de Graaff Accelerator and High Resolution System 21

B. Scattering Chamber and Detectors 25

C. Data Acquisition Electronics 29

D. Targets 36

E. Procedure 37

IV. DATA REDUCTION AND PRIMARY ANALYSIS 44

A. Preparation of Yield Curves 44

1. Energy Calibrations 45

2. Correction for Isotopic Impurities 47

B. R-matrix Fitting Procedure 48

1. Analysis of Resonances in ^{30}P 51

2. Analysis of Resonances in ^{28}Si 65

C. Data Presentation 96

1. Proton Scattering from ^{29}Si 96

2. Proton Scattering from ^{27}Al 113

V. ANALYSIS AND RESULTS 156

A. Analog States in ^{30}P and ^{28}Si 156

B. The $J^{\pi} = 6^{-}$, $T = 1$ Stretched State at $E_x = 14.36$ MeV in ^{28}Si 168

C. Entrance Channel ℓ-Mixing for a 2^{+} Resonance in ^{28}Si 171

VI. SUMMARY 185

APPENDIX 187

BIBLIOGRAPHY 200

LIST OF FIGURES

3.1 Floor Plan of the KN Van de Graaff Accelerator Laboratory 23

3.2 Top View of the Charged Particle Scattering Chamber and Collimator Assembly 27

3.3 Block Diagram of the Proton Detection and Counting Electronics 31

3.4 Block Diagram of the Alpha Particle Detection and Counting Electronics 35

3.5 Typical Spectra for Proton Scattering from ^{29}Si 39

3.6 Typical Spectra for Proton Scattering from ^{27}Al 41

4.1 Coulomb Penetrabilities Versus Energy for the $^{29}Si(p,p)$ and $^{29}Si(p,p_1)$ Reactions 54

4.2 Resonance Shapes for Proton Elastic Scattering from ^{29}Si 59

4.3 Data with R-matrix Fits for Three Values of ξ for a 1^- Resonance in ^{29}Si 62

4.4 Data with R-matrix Fits for Positive and Negative Values of γ for a 1^+ Resonance in ^{29}Si 64

4.5 Resonance Shapes for Proton Elastic Scattering from ^{27}Al 70

4.6 Variation with ξ of the $^{27}Al(p,p)$ Resonance Shapes for a 2^- p-wave Resonance 72

4.7 Variation with ξ of the $^{27}Al(p,p)$ Resonance Shapes for a 3^- p-wave Resonance 74

4.8 Variation with ξ of the $^{27}Al(p,p)$ Resonance Shapes for a 4^+ d-wave Resonance 76

4.9 Variation with ξ of the $^{27}Al(p,p)$ Resonance Shapes for a 4^- f-wave Resonance 78

4.10 Coulomb Penetrabilities Versus Energy for the $^{27}Al(p,p)$ and $^{27}Al(p,p_1)$ Reactions 82

4.11 Coulomb Penetrabilities Versus Energy for the $^{27}Al(p,p_2)$ and $^{27}Al(p,p_3)$ Reactions 84

4.12 Coulomb Penetrabilities Versus Energy for the $^{27}Al(p,\alpha_0)$ and $^{27}Al(p,\alpha_1)$ Reactions 86

4.13 Variation with P of the $^{27}Al(p,p)$ Resonance Shapes for a 2^+, $s = 2$ Resonance 88

4.14 Variation with P of the $^{27}Al(p,p)$ Resonance Shapes for a 3^-, $s = 2$ Resonance 91

4.15 Data with R-matrix Fits for Four Values of ξ for a 3^- Resonance in $^{27}Al(p,p)$ 93

4.16 Data with R-matrix Fits for Three Values of J for a 3^- Resonance in $^{27}Al(p,p)$ 95

4.17 Data and R-matrix Fit for $^{29}Si(p,p)$ for E_p = 1.29 - 2.50 MeV 109

4.18 Data and R-matrix Fit for $^{29}Si(p,p)$ and $^{29}Si(p,p_1)$ for E_p = 2.40 - 3.31 MeV 112

4.19 Data and R-matrix Fit for $^{27}Al(p,p)$ and $^{27}Al(p,\alpha_0)$ for E_p = 0.92 - 1.68 MeV at 90° and 105° 128

4.20 Data and R-matrix Fit for $^{27}Al(p,p)$ and $^{27}Al(p,\alpha_0)$ for E_p = 0.92 - 1.68 MeV at 135° and 160° 130

4.21 Data and R-matrix Fit for $^{27}Al(p,p)$, (p,p_1), (p,p_2) and (p,α_0) for E_p = 1.67 - 2.42 MeV at 90° 133

4.22 Data and R-matrix Fit for $^{27}Al(p,p)$, (p,p_1), (p,p_2) and (p,α_0) for E_p = 1.67 - 2.42 MeV at 105° 135

4.23 Data and R-matrix Fit for $^{27}Al(p,p)$, (p,p_1), (p,p_2) and (p,α_0) for E_p = 1.67 - 2.42 MeV at 135° 137

4.24 Data and R-matrix Fit for $^{27}Al(p,p)$, (p,p_1), (p,p_2) and (p,α_0) for E_p = 1.67 - 2.42 MeV at 160° 139

4.25 Data and R-matrix Fit for $^{27}Al(p,p)$, (p,p_1), (p,p_2), and (p,α_0) for E_p = 2.42 - 3.05 MeV at 90° 141

4.26 Data and R-matrix Fit for $^{27}Al(p,p)$, (p,p_1), (p,p_2), (p,α_0) and (p,α_1) for E_p = 2.42 - 3.05 MeV at 105° 143

4.27 Data and R-matrix Fit for $^{27}Al(p,p)$, (p,p_1), (p,p_2), (p,α_0) and (p,α_1) for E_p = 2.42 - 3.05 MeV at 135° 145

4.28 Data and R-matrix Fit for $^{27}Al(p,p)$, (p,p_1), (p,p_2), (p,α_0) and (p,α_1) for E_p = 2.42 - 3.05 MeV at 160° 147

4.29 The 160° Data and R-matrix Fit for $^{27}Al(p,p)$ and $^{27}Al(p,\alpha_0)$ in the Region of the 2^+ Resonance at E_p = 1.365 MeV 150

4.30 The 160° Data and R-matrix Fit for $^{27}Al(p,p)$ Resonances in the Range E_p = 1.65 - 1.85 MeV 152

4.31 The 160° Data and R-matrix Fit for $^{27}Al(p,p)$, (p,p_1), (p,p_2), (p,α_0) and (p,α_1) in the Region of the 6^-, T = 1 Resonance at E_p = 2.875 MeV 154

5.1 Energy Level Diagram Showing the Relation between the Parent State and the Analog State 158

5.2 Reduced Widths Versus Energy for Resonances in ^{30}P 161

5.3 Reduced Widths Versus Energy for Resonances in ^{28}Si 163

5.4 Spectrum for the $^{27}Al(p,\alpha_0)$ Reaction at E_p = 1.365 MeV . . . 178

5.5 Angular Distribution for the E_p = 1.365 MeV Resonance in $^{27}Al(p,\alpha_0)$ 180

5.6 The 160° Data and R-matrix Fits for the $^{27}Al(p,p)$ Resonance at E_p = 1.365 MeV 183

A.1 Block Diagram of the High Resolution System Electronics 189

A.2 Schematic Diagram of the Terminal Stabilizer Power Supplies 196

A.3 Schematic Diagram of the Terminal Stabilizer High Voltage Amplifier 198

LIST OF TABLES

4.1 Allowed Entrance and Exit Channels for Resonances in ^{30}P 55

4.2 Allowed Entrance and Exit Channels for Resonances in ^{28}Si 66

4.3 Legendre Coefficients for Angular Distributions of the $^{27}Al(p,p_1)$ Reaction 97

4.4 Legendre Coefficients for Angular Distributions of the $^{27}Al(p,p_2)$ Reaction 98

4.5 Legendre Coefficients for Angular Distributions of the $^{27}Al(p,\alpha_0)$ Reaction 100

4.6 Legendre Coefficients for Angular Distributions of the $^{27}Al(p,\alpha_1)$ Reaction 101

4.7 Resonance Parameters for $^{29}Si(p,p)$ and $^{29}Si(p,p_1)$ 103

4.8 Resonance Parameters for $^{29}Si(p,p_2)$ 107

4.9 Resonance Parameters for $^{27}Al(p,p)$ and $^{27}Al(p,\alpha_0)$ 114

4.10 Resonance Parameters for $^{27}Al(p,p_1)$ and $^{27}Al(p,p_2)$ 121

4.11 Resonance Parameters for $^{27}Al(p,\alpha_1)$ 123

4.12 Estimated Errors in ξ for Resonances in $^{27}Al(p,p)$ 125

4.13 Estimated Errors in P for Resonances in $^{27}Al(p,p)$ 126

5.1 Analog State Parameters for ^{30}P 165

5.2 Analog State Parameters for ^{28}Si 166

"For Mike's sake, Soddy, don't call it transmutation. They'll have our heads off as alchemists."

---Ernest Rutherford

from Pioneer Research on the Atom
by Muriel Howorth

PROTON RESONANCE SPECTROSCOPY IN ^{28}Si AND ^{30}P

CHAPTER I

INTRODUCTION

Compound nuclear resonances have been studied with proton beams of high energy resolution at Triangle Universities Nuclear Laboratory for many years. A wealth of spectroscopic information has been obtained from R-matrix analysis of proton elastic scattering data and from angular correlation measurements on proton induced reactions. The early studies provided the first measurement of the fine structure of isobaric analog states (Keyworth 1968). An extensive series of experiments on analog fine structure was then performed. In addition, information on strength functions and level densities was obtained. More recently predictions of the statistical model and of random matrix theory have been tested.

All of this previous research was performed with even-even target nuclei. Since the ground state spin of these nuclei is zero, only a single entrance channel is allowed. This restriction greatly simplifies the data analysis. In addition, for proton scattering at energies below 4 MeV, only one or two decay channels contribute strongly.

In this dissertation results are presented for the first measurements of high resolution proton resonance spectroscopy for targets with spin. Odd-mass targets in the nuclear 2s-1d shell are the most suitable for such studies. For odd-mass targets in the 1f-2p shell the neutron threshold is generally less than 2 MeV, leading to many open neutron channels and a resulting increase in the complexity of both the experiment and the analysis. In addition, the level densities obtained with targets in the

1f-2p shell are often very high. There are no odd-odd nuclei suitable as targets for proton resonance spectroscopy studies. In the scattering of low energy (< 3.5 MeV) protons from odd-mass targets in the mass range 19 < A < 39, the analysis is complicated by several factors. There are usually several open inelastic channels and sometimes open alpha channels, although the neutron channels are closed. In addition, the analysis of proton scattering from odd-mass targets is complicated by the possibilities of channel spin mixing and orbital angular momentum mixing in both the entrance and exit channels.

The new spectroscopic information obtainable with odd-mass targets provided part of the motivation for the present experiments. The nucleus ^{29}Si was chosen for the first study for several reasons: (1) the most information was available, (2) the level density was relatively low, and (3) the ^{29}Si ground state spin $\frac{1}{2}$ reduces the complexity of the analysis from that for targets with higher spins.

The measurement and analysis of 66 resonances in ^{30}P established that the analysis of these more complicated data was possible, and that the added complexity of the analysis did not lead to an unusual number of ambiguities in the extracted resonance parameters. The additional complexity of these data makes this spectroscopy even more rewarding. For example, the determination of channel spin mixing ratios is important in tests of parity mixing in nuclei, and measurement of orbital angular momentum mixing is crucial in the analysis of tests of time reversal invariance with nuclear resonances.

During the analysis of the ^{29}Si(p,p) data a preliminary measurement was made of the width of the $J^{\pi} = 6^{-}$, T = 1 stretched state in ^{28}Si via the ^{27}Al(p,p) reaction. Due to the theoretical interest in ^{28}Si and the results of the preliminary analysis, ^{27}Al was chosen as the second odd-mass target

to be studied.

Since ^{27}Al has a ground state spin $\frac{5}{2}$ and the (p,p), (p,p_1), (p,p_2), (p,α_0), and (p,α_1) channels contribute significantly, the measurement and analysis of proton scattering from ^{27}Al represented another large increase in the complexity of the analysis. The results of this analysis have been very interesting. The implications of the measured width of the $J^{\pi} = 6^{-}$, T = 1 stretched state are presented in section B of chapter V. A precise determination of the orbital angular momentum mixing ratio for a resonance in the ^{27}Al(p,α) reaction and its relation to a previous test of time reversal invariance are described in section C of chapter V, while the identification of a number of analog states in both ^{30}P and ^{28}Si is discussed in section A of chapter V. The R-matrix theory utilized in the analysis is outlined in chapter II, while the high resolution system and experimental equipment are described in chapter III. The details of the analysis procedure and the spectroscopic results are presented in chapter IV. A brief summary of the results is given in chapter VI.

CHAPTER II

R-MATRIX AND ANGULAR CORRELATION THEORY

A. Introduction

The discovery of slow neutron resonances in 1935 (Moon) demonstrated that long-lived virtual states were formed in low energy nuclear scattering. A typical time for a nuclear process had previously been assumed to be on the order of 10^{-21} s, the time for a nucleon to cross a volume of nuclear dimensions. The observation of resonances indicated the existence of states with lifetimes on the order of 10^{-15} s, which is very long on the nuclear time scale.

In 1936 Bohr proposed a mechanism for the formation of a long-lived compound nuclear state. The basic assumption was that the energy of the incident nucleon is rapidly distributed among the other protons and neutrons in the target nucleus so that the probability of any one nucleon gaining sufficient energy to be ejected is very small. Thus the compound system undergoes many exchanges of energy before the system decays by emitting a particle or electromagnetic radiation.

Perturbation theory was employed in the initial descriptions of nuclear processes; an analogy was drawn with the theory of radiative decay in atomic systems. Although this treatment yielded the famous Breit-Wigner formula for the cross section, the use of perturbation theory to describe the strong nuclear interaction was clearly not correct, and difficulties arose in assigning physical meaning to the quantities which appeared in the theory.

Major effort was placed on the development of the theory of the

compound nucleus. By the mid 1930's Kapur and Peierls (1938) had formulated a rigorous theory of the compound nucleus, and in the late 1940's Wigner and Eisenbud (Wigner 1946a; Wigner 1946b; Wigner and Eisenbud 1947) produced a similar theory. The theory of Wigner and Eisenbud has proved more convenient for the analysis of compound nuclear resonance data. This theory, with modifications and additions, is described in a comprehensive review by Lane and Thomas (1958).

The R-matrix theory is usually formulated in the channel spin representation. In this representation the spin of the target and projectile are coupled to form a channel spin. The channel spin may then be coupled with the relative orbital angular momentum of the target and projectile to form the spin of the compound state. This representation is convenient when dealing with unpolarized beams and targets because the cross section may be expressed as a weighted sum of the cross sections for each channel spin, i.e., the cross sections are incoherent in channel spin.

One alternative approach is to couple the projectile spin and the relative orbital angular momentum of the target and projectile to form a total angular momentum. This may be combined with the target spin to form the spin of the compound state. This representation is usually called the total angular momentum representation. Because contributions to the cross section for different orbital angular momenta add coherently, the cross sections for different values of the total angular momentum also add coherently. This representation is convenient when discussing the shell model description of the compound state or for the description of gamma decay where the intrinsic spin can not be separated from the orbital angular momentum. The transformation between reduced width amplitudes in the channel spin representation and the angular momentum representation is given by Devons and Goldfarb (1957). Except for Chapter 5, the channel spin

representation will be employed throughout this dissertation.

In the following sections the basic features of the R-matrix theory as formulated by Lane and Thomas are presented without proof, and the features of the differential scattering cross sections which are particularly important to the work in this dissertation are emphasized. A brief discussion of the general features of the angular distributions of reaction products is also included.

B. R-Matrix Theory

The R-matrix theory assumes the applicability of non-relativistic quantum mechanics in describing low energy nuclear reactions. This is a valid assumption since the nucleon kinetic energies inside the nucleus are less than a few percent of the rest mass energy. The theory treats only two-body nuclear reactions and does not include processes of creation or annihilation, such as gamma decay. In addition, it is assumed that a pair of nuclei experience no mutual nuclear interaction beyond some finite separation distance; the forces are short range.

The projectile and target nucleus which form the compound nucleus are called the entrance pair, and the two nuclei into which the compound state decays are called the exit pair. The letter α, used to label a pair of nuclei, specifies the quantum states of each of the members of the pair. For two nuclei with spins I_1 and I_2 (with corresponding projections, i_1 and i_2), the channel spin s (with component ν) is formed by vector-coupling I_1 and I_2. The resultant channel spin may therefore assume values between $|I_1-I_2|$ and $|I_1+I_2|$. In addition, the relative orbital angular momentum ℓ (and its component m) of the pair may be specified. The letter c is used to denote the set $[\alpha(I_1,I_2)s\nu\ell m]$ which specifies a given pair of nuclei. The channel spin and ℓ value may be combined to give a resultant total angular

momentum J (with component M), in which case c implies the set $[\alpha(I_1, I_2)s\ell JM]$. The following quantities are also useful:

$a_c = a_\alpha$, the interaction radius beyond which the pair feels no mutual nuclear interaction,

$E_c = E_\alpha$, the energy of relative motion,

$M_c = M_\alpha = M_{\alpha_1} M_{\alpha_2} / (M_{\alpha_1} + M_{\alpha_2})$, the reduced mass,

$k_c = k_\alpha = \left[2M_\alpha E_\alpha / \hbar^2\right]^{1/2}$, the wave number,

$v_c = v_\alpha = \hbar k_c / M_c$, the relative velocity,

$\eta_c = \eta_\alpha = Z_{\alpha_1} Z_{\alpha_2} e^2 / \hbar v_\alpha$, the Coulomb field parameter,

$\rho_c = \rho_\alpha = k_c r_c$, a dimensionless parameter.

The problem is to solve the Schroedinger equation. The procedure for this is to partition the radial space into an external region ($r_c > a_c$) and an internal region ($r_c < a_c$). In the external region only the Coulomb force is present and the Schroedinger equation can be solved exactly. The resulting external wave functions are

$$\underline{\Psi}_c^{ext} = \chi_c(r_c) u_{\alpha\ell}(r_c) / v_c^{1/2} \quad ,$$

where

$$\chi_c(r_c) = \left[i^\ell Y_\ell^m(\theta_\alpha, \phi_\alpha) / r_c\right] \underline{\Psi}_{\alpha s \nu}$$

are the surface wave functions which are mutually orthogonal and normalized on the nuclear surface at $r_c = a_c$. The Y_ℓ^m are the usual spherical harmonics, and $\underline{\Psi}_{\alpha s \nu}$ are the channel spin wave functions formed by vector

coupling of the spin wave functions of the two nuclei. The function $u_{a\ell}$ is the radial wave function which solves

$$u''_{a\ell}(r_a)+[2M_a/\hbar^2][E_c-V_c]u_{a\ell}(r_c) = 0 \ ,$$

where the prime denotes differentiation with respect to r_c, and

$$V_c = Z_{a_1}Z_{a_2}e^2/r_c + \hbar^2\ell((\ell+1)/2M_c r_c^2$$

includes terms for the Coulomb and "centrifugal" potential energies.

Considering only open channels ($E_c > 0$), the radial equation has two linearly independent solutions, F_c and G_c, which are the regular and irregular Coulomb functions (Jahnke 1960). General solutions of the radial equation can be expressed as linear combinations of the regular and irregular Coulomb functions. The combinations

$$I_c^+ = [G_c - F_c] \exp(i\omega_c),$$

and

$$O_c^+ = [G_c + F_c] \exp(-i\omega_c),$$

where

$$\omega_c = \omega_{a\ell} = \sum_{n=1}^{\ell} \tan^{-1}(\eta_a/n),$$

represent incoming and outgoing waves.

The complete channel wave functions of the external region are then

$$I_c = \chi_c(r_c)I_c^+/v_c^{1/2} \ ,$$

and

$$O_c = \chi_c(r_c)O_c^+/v_c^{1/2}$$

which represent incoming and outgoing waves of unit flux.

A general solution in the external region can be expressed as a linear combination of I_c and O_c. For convenience the solution

$$\underline{\Psi}_c^{ext} = I_c - \sum_{c'} U_{cc'} O_{c'} ,$$

is chosen because it represents the external wave function for a particular incoming wave. The summation is over all channels and U is the collision or scattering matrix. The collision matrix element $U_{cc'}$, is the amplitude of the outgoing wave in channel c' that is associated with the particular incoming wave in channel c. For example, if c' = c this collision matrix element describes elastic scattering. The cross section may be expressed in terms of the collision matrix. Thus the problem is reduced to determining an analytical expression for $U_{cc'}$.

A form could be assumed for the nuclear potential in the internal region, the Schroedinger equation solved, and the internal and external solutions matched at the nuclear surface ($r_c = a_c$) to obtain $U_{cc'}$, but the results of this procedure would be dependent upon the parameters chosen for the nuclear potential. The R-matrix theory proceeds in a more formal manner by postulating a complete set of states which are eigenstates of the Hamiltonian in the internal region;

$$H_\lambda \underline{\Psi}_\lambda = E_\lambda \underline{\Psi}_\lambda ,$$

with

$$\int \underline{\Psi}_\lambda^* \underline{\Psi}_{\lambda'} dr = \delta_{\lambda\lambda'} .$$

This complete set of states covers all possible resonances of the compound nuclear system.

The channel wave functions can be expressed in terms of the overlap integral of the internal λ states with the appropriate external wave functions on the nuclear surface

$$\chi_\lambda(r_c) = \int_{a_c} \chi_c^* \underline{\Psi}_\lambda \, dS ,$$

where the integration is over the surface of radius a_c. The $\chi_\lambda(r_c)$ are eigenfunctions with eigenenergies E_λ in channel c and have arbitrary, real, energy independent boundary conditions

$$\left[\rho_c \chi_c'/\chi_c\right]_{r_c=a_c} = B_c$$

where the prime denotes differentiation with respect to ρ_c.

The wave functions in the internal region for any energy E can be expressed in terms of an expansion of the eigenfunctions, $\chi_\lambda(r_c)$. An application of Green's theorem may be used to determine the coefficients of this expansion. The resulting expression for the internal wave function is

$$\underline{\Psi}_c^{int}(r_c) = R_{cc'}\left[a_c \frac{d\underline{\Psi}_c^{int}(r_c)}{dr} - B_c \underline{\Psi}_c^{int}(r_c)\right]_{r_c=a_c}$$

where

$$R_{cc'} = \sum_\lambda \frac{\gamma_{\lambda c}\gamma_{\lambda c'}}{(E_\lambda - E)}, \qquad 2.1$$

is the Green's function that relates the value of the wave function in the internal region to its derivative on the surface, and

$$\gamma_{\lambda c} = \left[\hbar^2/2M_c a_c\right]^{1/2} \chi_\lambda(a_c)$$

$$= [\hbar^2/2M_c a_c]^{1/2} \int_{a_c} \chi_c^* \Psi_\lambda \, dS \, .$$

These equations define the elements of the R-matrix, $R_{cc'}$, and the reduced width amplitudes, $\gamma_{\lambda c}$. The U-matrix is expressed in terms of the R-matrix by equating the logarithmic derivatives (the usual continuity condition) of the internal and external wave functions at $r_c = a_c$. The result is

$$U_{cc'} = \exp[i(\omega_c+\omega_{c'}-\phi_c-\phi_{c'})]\left[\delta_{cc'}+2iP_c^{1/2}\,[1-R_{cc'}L_{c'}]^{-1}R_{cc'}P_{c'}^{1/2}\right] \quad 2.2$$

where

$$L_c = \left[\rho_c \frac{O_c'}{O_c}\right]_{r_c=a_c} - B_c$$

$$= [S_c^\lambda - B_c] + iP_c \, ,$$

and the quantities P_c, S_c, and ϕ_c may be expressed in terms of the Coulomb functions as

$$P_c = \left[\rho_c/(F_c^2+G_c^2)\right]_{r_c=a_c} \, ,$$

$$S_c = \left[\rho_c (F_c F_c'+G_c G_c')/(F_c^2+G_c^2)\right]_{r_c=a_c} \, ,$$

and

$$\phi_c = \tan^{-1}(F_c/G_c).$$

P_c is the called the penetrability and is proportional to the probability of transmission through the external barrier. S_c is called the shift function because it appears in the expression for the level shift, to be discussed next. The phases ω_c and ϕ_c are the Coulomb and hard sphere phases for channel c. The following definitions are useful in applying the theory:

$$\Delta_\lambda = -\sum_{c'} [S_{c'}^{\lambda} - B_{c'}] \gamma_{\lambda c'}^2 ,$$

and

$$\Gamma_\lambda = \sum_c \Gamma_{\lambda c} \; ; \quad \Gamma_{\lambda c} = 2P_c \gamma_{\lambda c}^2 \; . \qquad 2.3$$

The quantity Δ_λ is the total energy shift from the eigenenergy E_λ and results from a mismatch of the external and internal boundary conditions. The quantities Γ_λ and $\Gamma_{\lambda c}$ are the total and partial laboratory (or natural) widths. The partial width can be interpreted as the transition probability from the state λ to the configuration c. The laboratory width consists of the product of a factor which accounts for the kinematic effects in the external region (the penetrability) and a factor which describes the internal properties (the reduced width). Since the penetrability decreases with increasing ℓ values, the laboratory widths for states formed by the higher angular momenta will, statistically, be smaller than the widths of states of lower angular momenta. The reduced widths allow comparison of the strength of the nuclear coupling to the entrance channel with the kinematic effects of the external region removed. The total width is inversely proportional to the lifetime of the level, i.e.

$$\Gamma_\lambda \sim \frac{\hbar}{T_{1/2}}$$

From time reversal invariance (or reciprocity) the collision matrix must be symmetric, as is the R-matrix. In addition, conservation of parity and angular momentum requires that the R-matrix and the collision matrix be diagonal in the total spin and in parity. The cross section, of course, includes contributions from all spins and parities. Lane and Thomas derive the relationship between the elements of the collision matrix and the differential cross section. The resulting equation which is programmed in

the computer code MULTI is

$$\frac{d\sigma_{\alpha s,\alpha' s'}}{d\Omega_{\alpha'}} = \pi k_\alpha^{-2} |C_{\alpha'}(\theta_{\alpha'})|^2 \delta_{\alpha' s',\alpha s}$$

$$+ [k_\alpha^2(2s+1)]^{-1} \sum_L B_L(\alpha' s',\alpha s) P_L(\cos\theta_{\alpha'}) \qquad 2.4$$

$$+ \pi^{1/2}[k_\alpha^2(2s+1)]^{-1} \sum_{J\ell} (2J+1)\delta_{\alpha' s'\ell',\alpha s\ell} \mathrm{Re}\left[iT^J_{\alpha' s'\ell',\alpha s\ell} C_{\alpha'}(\theta_{\alpha'}) P_\ell(\cos\theta) \right]$$

where

$$B_L(\alpha' s',\alpha s) = \frac{1}{4}(-)^{(s-s')} \sum_{J_1 J_2 \ell_1 \ell_2 \ell_1' \ell_2'} \bar{Z}(\ell_1 J_1 \ell_2 J_2, sL)$$

$$\cdot \bar{Z}(\ell_1' J_1 \ell_2' J_2, s' L) \left(T^{J_1}_{\alpha' s'\ell_1',\alpha s\ell_1}\right) \left(T^{J_2}_{\alpha' s'\ell_2',\alpha s\ell_2}\right)^*, \qquad 2.5$$

$$T^J_{\alpha' s'\ell',\alpha s\ell} = \exp(2i\omega_{\alpha'\ell'}) \delta_{\alpha' s'\ell',\alpha s\ell} - U^J_{\alpha' s'\ell',\alpha s\ell} \qquad 2.6$$

and

$$C_\alpha = [4\pi]^{-1/2} \eta_\alpha \csc^2(\theta_\alpha/2) \exp\left[-2i\eta_\alpha \log[\sin(\theta_\alpha/2)]\right] \qquad 2.7$$

The $\bar{Z}$ coefficients are the Z coefficients of Biedenharn et al. (1952) with the phase convention of Huby (1954). The $P_\ell(\cos\theta)$ are the Legendre polynomials with the phase convention of Condon and Shortly (1951).

The first term in the cross section expression represents pure Coulomb

scattering, the second term describes resonance scattering and reaction, and the third term is due to the interference between the first two. The Coulomb and the interference term vanish except in the case of pure elastic scattering (scattering without change of energy or channel spin). The experimentally measured cross section for an unpolarized beam and target is given by eqn. 2.4 summed over s' and averaged over s

$$\frac{d\sigma_{a,a'}}{d\Omega_{a'}} = [(2I_1+1)(2I_2+1)]^{-1}\sum_{ss'} \frac{d\sigma_{as,a's'}}{d\Omega_{a'}}.$$

MULTI also performs these averages and sums.

It is useful to examine the dependence of the cross section on energy, on the magnitudes and phases of the reduced width amplitudes, and on the values of the channel spin, orbital angular momentum, and total angular momentum. The simplest case to be considered is that of a single, isolated (all other levels far away in energy) level with two channels. The result for the single level case (the Breit-Wigner form of the cross section) will be derived first and then the two-level, two-channel cross section formula will be obtained.

In the single level, two-channel case, the elements of the R-matrix are, from eqn. 2.1,

$$R_{cc'} = \frac{\gamma_c \gamma_{c'}}{(E_0 - E)},$$

for $E_\lambda = E_0$.

The matrix inversion implied in eqn. 2.2 may be performed to find the elements of the collision matrix

$$U_{cc'} = \exp[i(\omega_c+\omega_{c'}-\phi_c-\phi_{c'})]\left[\delta_{cc'} + \frac{i\Gamma_c^{1/2}\Gamma_{c'}^{1/2}}{(E_o+\Delta_o-E)-\frac{i}{2}\Gamma_o}\right], \qquad 2.8$$

where $\Gamma_\lambda = \Gamma_o$ is the total width of eqn. 2.3.

The effect of the level shift, mentioned previously, is apparent in eqn. 2.8. To simplify the notation, and in keeping with the assumptions made in the analysis, the level shift Δ_o will always be set equal to zero for each resonance (i.e., the boundary condition parameter B_c will be set equal to the shift factor S_c). For the analysis of the data in this dissertation this assumption yields the least error in extracting a physically meaningful width. Using eqn. 2.6 for the T-matrix elements, the products in eqns. 2.4 and 2.5 are

$$\mathrm{Re}\left[iT^J_{\alpha's'\ell',\alpha s\ell}C_{\alpha'}(\theta_{\alpha'})\right] = -2\sin(\phi)\cos(2\omega-2\beta-\phi)\delta_{\alpha's'\ell',\alpha s\ell} + C'_{\alpha'}(\theta_{\alpha'})\Gamma_{s\ell}\frac{[(E_o-E)\cos(\tau) - \frac{1}{2}\sin(\tau)\Gamma_o]\delta_{\alpha's'\ell',\alpha s\ell}}{(E_o-E)^2+(\Gamma_o/2)^2} \qquad 2.9$$

and

$$(T^{J_1}_{\alpha's'\ell_1',\alpha s\ell_1})(T^{J_2}_{\alpha's'\ell_2',\alpha s\ell_2})^* = 4\sin^2(\phi_\ell)\delta_{\alpha's'\ell',\alpha s\ell} - 2\,\delta_{\alpha's'\ell',\alpha s\ell}\Gamma_{s\ell}\frac{\left[(E_o-E)\sin(2\phi_\ell) + \frac{1}{2}\Gamma_o(1-\cos(2\phi_\ell))\right]}{(E_o-E)^2+(\Gamma_o/2)^2}$$

$$+ \frac{\Gamma_{s\ell_1}^{1/2}\Gamma_{s\ell_2}^{1/2}\Gamma_{s'\ell_1'}^{1/2}\Gamma_{s'\ell_2'}^{1/2}}{(E_o-E)^2+(\Gamma_o/2)^2}\cos(\omega_{\ell_1}+\omega_{\ell_1'}-\omega_{\ell_2}-\omega_{\ell_2'}+\phi_{\ell_1}+\phi_{\ell_1'}-\phi_{\ell_2}-\phi_{\ell_2'}) \qquad 2.10$$

where $\tau = 2(\omega_\ell - \phi_\ell - \beta)$, $\beta = \exp\left[-2i\eta_\alpha\log[\sin(\theta_\alpha/2)]\right]$,
and $C'_{\alpha'} = [4\pi]^{-1/2}\eta_\alpha\,\mathrm{cosec}^2(\theta_\alpha/2)$.

The first and second terms of eqn. 2.10 represent the nuclear potential (or hard sphere) scattering and the corresponding interference with

resonance scattering, respectively. Since the nuclear potential scattering cross section increases with energy while the Coulomb scattering cross section decreases rapidly with energy, the nuclear potential scattering becomes more important relative to the Coulomb scattering as the reaction energy increases. The third term of eqn. 2.10 represents the resonance and reaction scattering. Note that from eqn. 2.3, $\Gamma_{s\ell}^{1/2} = \pm [2P(\ell)]^{1/2}\gamma_{s\ell}$, so the products in eqns. 2.9 and 2.10 may be written in terms of reduced width amplitudes and penetrabilities.

From eqns. 2.4, 2.5, 2.9 and 2.10 the dependence of the cross sections on the various parameters can be determined. First consider pure elastic scattering where $\alpha' = \alpha$, $s' = s$, and $\ell' = \ell$. Both of the potential scattering terms and their corresponding interference terms contribute to the cross section. The contribution due to the interference terms depends on the spin as $(2J+1)$, and the interference effects decrease with energy away from E_0 as $(E_0-E)^{-1}$. For pure elastic scattering the resonance term depends on energy as $(E_0-E)^{-2}$, on the spin J only through the $\bar{Z}$ coefficients, and is independent of the relative signs of the reduced width amplitudes.

The experimentally measured elastic scattering cross section also includes spin flip (change of channel spin) terms. Formally, these terms are considered to be part of the reaction cross section. The sign of these terms is determined by the phase $(-)^{s-s'}$ and the signs of the corresponding $\bar{Z}$ coefficients. Note that although spin flip events occur, the entrance and exit channel spin admixtures must be the same due to the symmetry of the collision matrix.

For nonelastic scattering ($\alpha' \neq \alpha$) only the reaction term remains. This term has the same energy and spin dependence as the resonance term. The reaction cross sections for different channel spins add incoherently,

i.e., there are no cross terms. Interference between different ℓ values occurs in both the entrance and exit channels. The relative signs of the reduced width amplitudes of the two ℓ values can, in principle, be determined from a measurement of the differential cross sections. Conservation of parity implies that the cross section for an isolated resonance will contain only terms with even order Legendre polynomials. This result follows from the properties of the $\bar{Z}$ coefficients. For $J_1 = J_2 = J$, the $\bar{Z}$ coefficients vanish unless $\ell_1 + \ell_2$ is even.

The single level formula can also be applied in the case of two levels of different spins or parities. This is possible because the R-matrix and the collision matrix are diagonal in spin and parity. Each submatrix can be treated as a single level. The resonance and reaction term of the cross section contains cross terms for the different spins and parities. The sign of the cross terms depends on the phases of the $\bar{Z}$ coefficients, on the phase $(-)^{s-s'}$, and, if two ℓ values contribute, on the relative phases of the reduced width amplitudes. If two overlapping resonances have different parities, then parity is no longer a good quantum number in the region of overlap, and the usual limitation to even order Legendre polynomial terms in the cross sections does not hold.

The two-level, two-channel cross section expression is much more complicated but has some important interference features. The elements of the two-level R-matrix are

$$R_{cc'} = \frac{\gamma_{1c}\gamma_{1c'}}{(E_1-E)} + \frac{\gamma_{2c}\gamma_{2c'}}{(E_2-E)} ,$$

and the reaction elements of the two-level, two-channel collision function are

$$U_{cc'} = \frac{i \exp[i(\omega_c+\omega_{c'}-\rho_c-\rho_{c'})]\left[(E_2-E)\Gamma_{1c}^{1/2}\Gamma_{1c'}^{1/2}+(E_1-E)\Gamma_{2c}^{1/2}\Gamma_{2c'}^{1/2}\right]}{(E_1-E)(E_2-E)-\frac{i}{2}(E_2-E)\Gamma_1-\frac{i}{2}(E_1-E)\Gamma_2-\frac{1}{4}\left[(\Gamma_{1c}\Gamma_{2c'})^{1/2}-(\Gamma_{2c}\Gamma_{1c'})^{1/2}\right]^2}$$

for $c \neq c'$.

Calculating the corresponding T-matrix elements and substituting into eqns. 2.4 and 2.5 the angle integrated cross section expression becomes

$$\sigma_{\alpha\alpha'} = \frac{\pi g_J}{k_\alpha^2} \sum_{s\ell s'\ell'} \frac{\left[(E_2-E)\Gamma_{1c}^{1/2}\Gamma_{1c'}^{1/2}+(E_1-E)\Gamma_{2c}^{1/2}\Gamma_{2c'}^{1/2}\right]^2}{\left[(E_1-E)(E_2-E)+\frac{1}{4}(\Gamma_{12}^2-\Gamma_1\Gamma_2)\right]^2+\frac{1}{4}\left[\Gamma_1(E_2-E)+\Gamma_2(E_1-E)\right]^2}$$

where $\Gamma_{12} = \Gamma_{1c}^{1/2}\Gamma_{2c}^{1/2}+\Gamma_{1c'}^{1/2}\Gamma_{2c'}^{1/2}$ and $g_J = \frac{(2J+1)}{(2I_1+1)(2I_2+1)}$, and Γ_1 and Γ_2 are the total widths for $\lambda = 1$ and 2.

The important feature of the two level, two channel cross section for reactions and resonance scattering is that, for the reaction terms (spin flip, etc.), the cross section between resonances will vanish if $\gamma_{1c}\gamma_{1c'}$ and $\gamma_{2c}\gamma_{2c'}$ have the same sign but not otherwise. This can be seen by examining the numerator of the angle integrated cross section above. For elastic scattering this two level interference will only appear if two channels contribute to at least one of the resonances. In the single channel case both of the reduced width products are always positive. These interference terms can produce noticeable differences in the cross sections over energy regions several times the widths of the resonances. For two level interference in reactions, the relative signs of each of the products above must be considered in fitting the data.

C. Properties of the Angular Distributions of Reaction Products

A general theorem (Yang 1948) of angular correlation theory states that the complexity of any angular distribution is limited by the spin of the

state and the contributing ℓ values. The highest order of Legendre polynomial that appears must be less than or equal to the smallest of $2\ell_1$, $2\ell_2$, $2\ell_1'$, $2\ell_2'$, and 2J. This result is implicit in the cross section expressions above, following from the properties of the $\bar{Z}$ coefficients.

As discussed in the previous section, only even order Legendre polynomials appear in the cross section formula for an isolated resonance. Thus, the angular distribution may be written as

$$W(\theta) \propto 1 + a_2 P_2 + a_4 P_4 + \ldots$$

where the normalized a_L coefficients depend upon the reduced width amplitudes and the angular momentum coupling coefficients, and the $P_L(\cos\theta)$ are the Legendre polynomials. Since the even order Legendre polynomials are functions of $\cos^2(\theta)$, it is often convenient to plot the angular distribution, $W(\theta)$, versus $\cos^2(\theta)$. Thus, a reaction angular distribution will be isotropic if the entrance or exit ℓ values are zero or if J = 0. The distribution of the decay of a resonance with $\ell = 1$, only, or J = 1, will be linear in $\cos^2(\theta)$, and a resonance for which $\ell_{max} = 2$, or J = 2, will be quadratic in $\cos^2(\theta)$. These results aid in determining the resonance parameters from the angular distribution data, although interference between resonances may obscure the single level angular distributions.

CHAPTER III

EXPERIMENTAL EQUIPMENT AND PROCEDURES

A. The KN Van de Graaff Accelerator and High Resolution System

The experiments described in this dissertation were performed with the HVEC model KN Van de Graaff accelerator and associated high resolution system at Triangle Universities Nuclear Laboratory (TUNL). The homogenizer high resolution system is a modern version of the system originally described by Parks (1958). Elastic and inelastic scattering from ^{29}Si were studied with the high resolution system described in detail by Wells (1978). For this system the maximum working proton energy was 3.3 MeV due to the electrostatic analyzer bias supply limit and to the maximum electrostatic potential obtainable with the aluminum-electrode accelerator tube. During the course of this work a stainless steel-electrode accelerator tube was installed, and modified analyzer biasing and feedback circuits were implemented which allow operation at 4.0 MeV or higher. This most recent system, employed in the study of proton scattering from ^{27}Al, is described briefly here and in more detail in the Appendix.

A block diagram of the accelerator and feedback systems is shown in figure 3.1. A radio-frequency (RF) ion source in the terminal of the accelerator produces H^+ and HH^+ hydrogen ions which are focused and accelerated into an analyzing magnet. In the magnet the proton beam (H^+) is deflected 25^o and thus separated from the heavier molecular (HH^+) beam which is deflected 17^o. The molecular beam passes into a one meter radius, 90^o cylindrical electrostatic analyzer while the proton beam is transported

Figure 3.1 Layout of the KN Van de Graaff accelerator laboratory showing the major feedback systems.

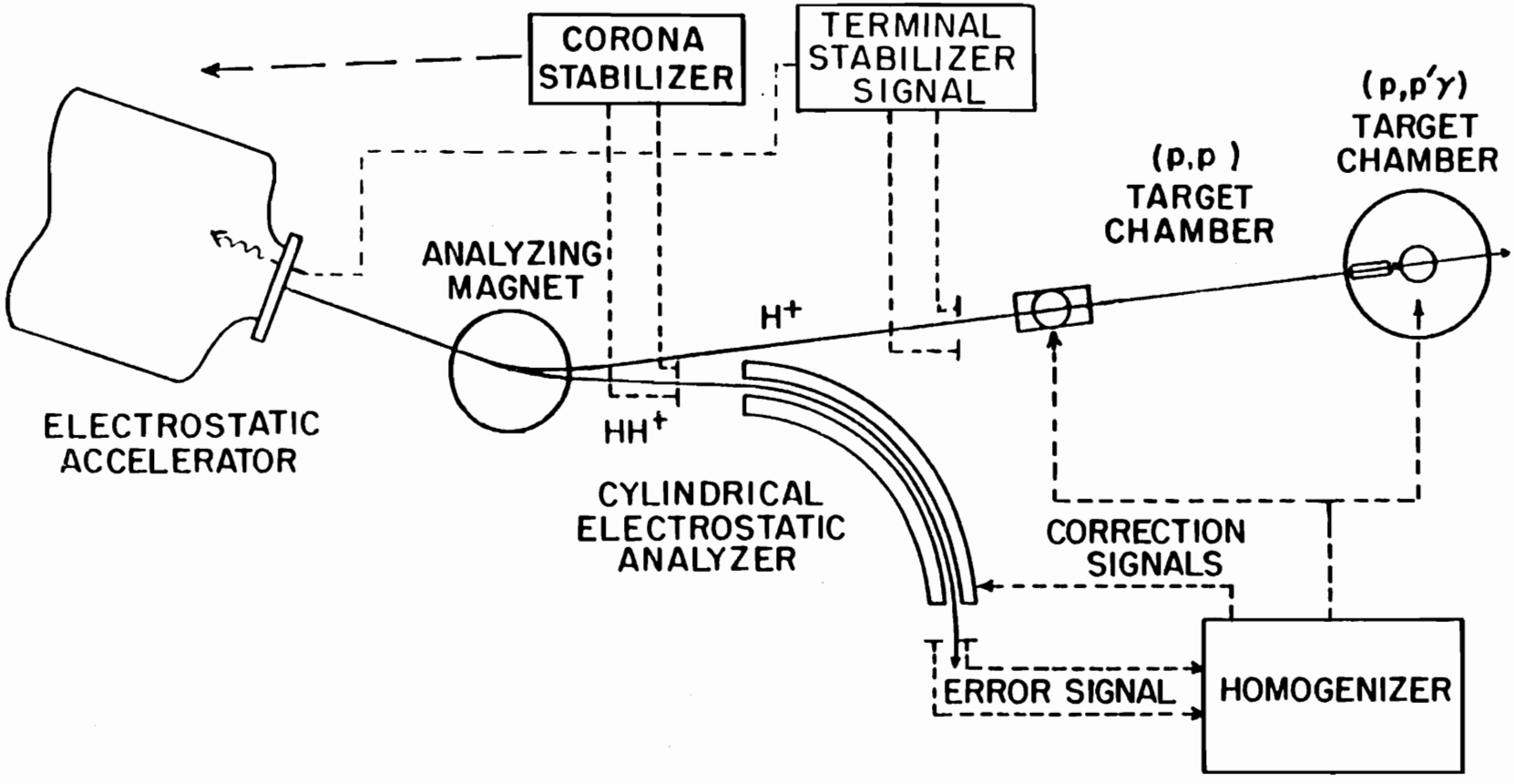
CORONA STABILIZER
TERMINAL STABILIZER SIGNAL
(p,p'γ) TARGET CHAMBER
(p,p) TARGET CHAMBER
ANALYZING MAGNET
H+
HH+
ELECTROSTATIC ACCELERATOR
CYLINDRICAL ELECTROSTATIC ANALYZER
CORRECTION SIGNALS
ERROR SIGNAL
HOMOGENIZER

through the experimental beam line to the scattering chamber.

A pair of vertically oriented slits in front of the analyzer serve as both object slits for the analyzer and as feedback slits for the corona control circuit. The error signal generated at the corona feedback slits reflects fluctuations in the terminal potential. This error signal is amplified and applied to the grid of the corona tube to control the rate of emission of electrons from the corona needles. Electrons emitted from the corona needles combine with molecules of the high pressure insulating gas to form negatively charged ions which drift to the positively charged terminal, thus closing the corona control feedback loop. Due to the relatively low dispersion of the analyzing magnet and to the finite drift time of the ions in traveling from the corona needles to the accelerator dome, the corona circuit removes only large, low frequency ($\lesssim$ 10 Hz) terminal voltage fluctuations. Residual fluctuations are typically two to three kV peak-to-peak (pp) in magnitude, while unregulated terminal voltage fluctuations are usually about 10 kV (pp) in magnitude.

The greater dispersion at the image slits of the electrostatic analyzer provides an error signal which may be used to reduce the remaining fluctuations. This reduction may be accomplished either by sending a fast correction signal to modulate the accelerator tube potential with respect to the terminal, as in the system due to Bloch (1968), or by applying the correction signal to the target, as is done with the TUNL homogenizer. The latter method was utilized in performing these experiments, although a Bloch-style terminal stabilizer has been constructed and is described in the Appendix.

The analyzer plates are biased with large (about 1/222 times the terminal voltage), equal and opposite voltages to radially accelerate the beam through the analyzer. This dual-sided operation is new and allows

larger potentials to be applied across the analyzer plates. Dual-sided operation also eliminates the tangential acceleration of the beam into the analyzer since the net potential at the input is now essentially zero. The image slits at the analyzer output provide a correction signal which is amplified and applied via optical coupling to the analyzer outer plate. This closes the feedback loop to keep the beam centered in the analyzer and yields an outer plate signal which is proportional to the beam energy fluctuations (of both the H^+ and HH^+ beams). The ratio of the beam energy fluctuations to the outer plate signal is determined by the analyzer geometry and is approximately 111. Thus, the signal on the outer plate is amplified with a gain of 111 and applied to the target rod which is biased at +4 kV. With this bias voltage energy errors of up to 8 keV (pp) can be corrected.

The overall resolution in an experiment is given approximately by the sum in quadrature of the target Doppler broadening and energy straggling, the beam energy spread due to remaining terminal voltage fluctuations, and the intrinsic ion source beam energy spread. The best resolution obtained with an early version of this system was 110 eV (Keyworth 1968) with a cryogenically cooled gas target. Recent experiments with thin solid targets have achieved resolutions of 300–400 eV.

B. Scattering Chamber and Detectors

The charged particle scattering chamber used in these experiments was designed by Browne (1969). A top view of the chamber showing the collimators and detector mounts is given in figure 3.2. The beam collimation confined the beam spot to a small area at the center of the target. This minimizes the yield changes which occur with variations in beam position and spot size. The first three collimators define the beam

Figure 3.2 Top view of the charged particle scattering chamber and collimator assembly.

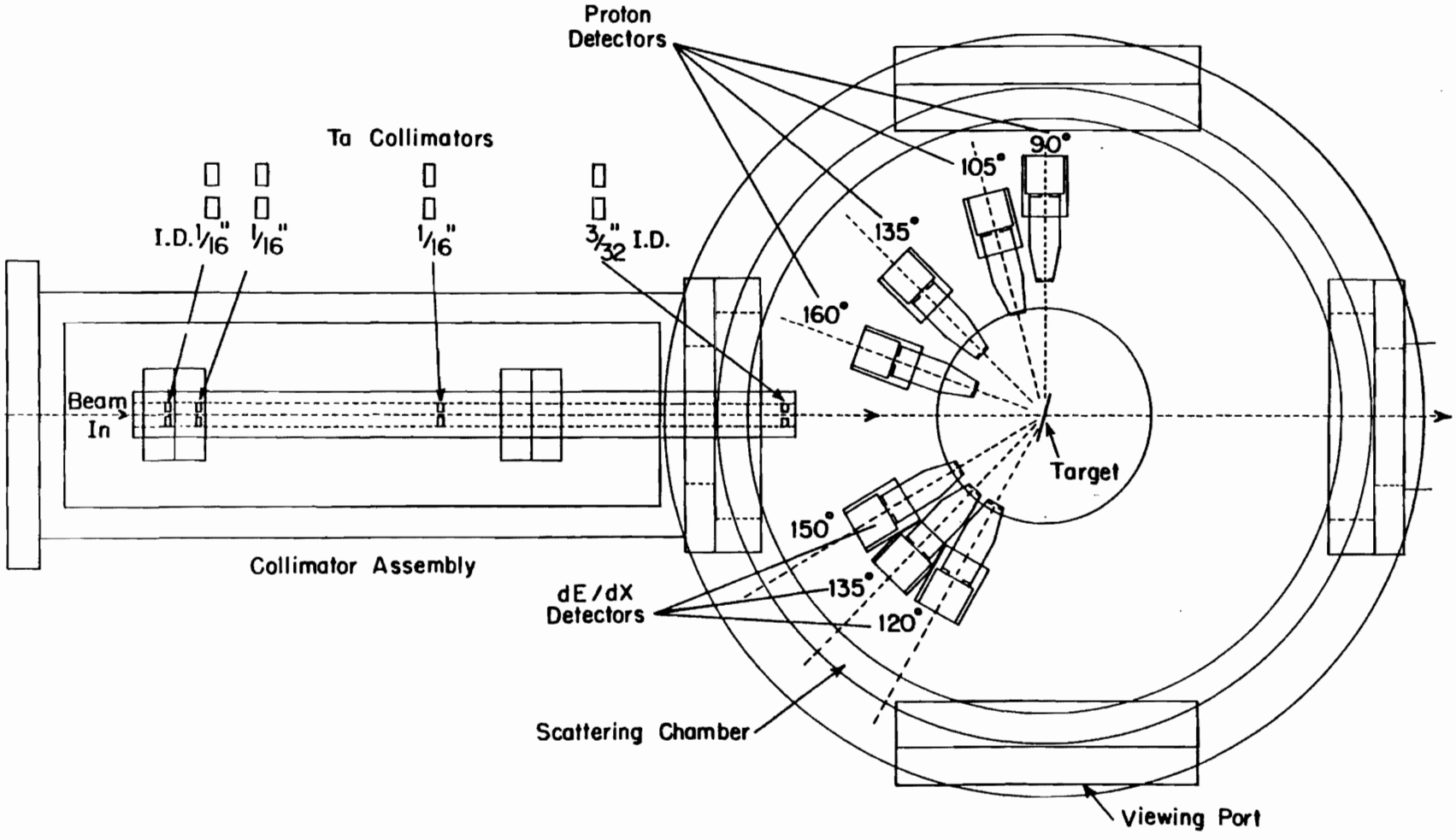
Proton
Detectors
Ta Collimators
I.D. 1/16"
1/16"
1/16"
3/32" I.D.
Beam
In
Collimator Assembly
90°
105°
135°
160°
Target
150°
135°
120°
dE/dX
Detectors
Scattering Chamber
Viewing Port

size and position and the final, slightly larger collimator, reduces background due to scattering from the slit and collimator apertures. An oil diffusion pump with a freon cooled baffle and a liquid nitrogen cold trap in the top of the chamber maintained a vacuum of better than 10^{-6} Torr in the chamber during the experiments. This system reduced the buildup of contaminants on the target surface which would degrade the energy resolution.

In both experiments the scattered protons were detected by standard Ortec silicon surface barrier detectors at laboratory angles of 90°, 105°, 135°, and 160°. The kinematics of the $^{27}Al(p,\alpha)^{24}Mg$ reaction are such that alpha particles which decay to the ground state of ^{24}Mg could also be detected in the proton detectors. Unfortunately, alpha particles which decay to the first excited state of ^{24}Mg overlapped in energy with protons elastically scattered from ^{16}O. Therefore, three Ortec transmission surface barrier (dE/dx) detectors were employed to measure this alpha decay. These detectors were mounted at laboratory angles of 120°, 135°, and 150°.

The proton detectors had an active area of 50 mm^2 and a depletion depth of 100 μm when properly biased. This depletion depth is sufficient to stop a proton with an energy of 3.2 MeV. For elastic scattering from Al or Si this yields a maximum incident beam energy of 3.5 MeV (at 160°). The dE/dx detectors were about 40 μm thick with 50 mm^2 active area. This thickness is sufficient to stop a 7 MeV alpha particle. The maximum proton energy loss is about 2 MeV since protons of higher energy are not completely stopped in the detector. For energies greater than 2.4 MeV the alpha particle peaks were well separated from the proton peaks in the spectra of the dE/dx detectors.

The proton detector resolutions were between 15 and 20 keV

full-width-at-half-maximum (FWHM). The dE/dx detectors had resolutions of 25 to 40 keV (FWHM) due to the increased noise (from the large capacitance) of these detectors. These resolutions were adequate to separate the peaks of interest from the major contaminant peaks in the spectra.

In order to achieve similar counting statistics at all angles for elastic scattering the proton detectors were positioned so that equal counting rates were obtained for Rutherford scattering. This was accomplished by choosing the detector collimators and the radial target to detector distances to give appropriate solid angles. The solid angles used were: 90^{o} - 1.0 msr, 105^{o} - 1.5 msr, 135^{o} - 2.4 msr, and 160^{o} - 2.7 msr. A detailed description of the detector collimators is given by Sales (1980). The dE/dx detectors each subtended a solid angle of 1.8 msr. This was the maximum solid angle allowed by the detector holders and the largest collimators. Due to the relatively small $^{27}Al(p,\alpha)$ cross sections a large solid angle was desired to obtain the best counting statistics possible.

C. Data Acquisition Electronics

The original Prime 300 interface is described by Chandler (1978). This original data acquisition system and the associated electronics have undergone two significant changes during the course of this work. The first of these modifications was the replacement of the eight input router and its associated interface with a Borer ADC buffer module and a new interface (utilized in all of these experiments). In addition, the dual sum and invert modules, used to sum the linear signals from all angles, have been replaced by an eight input multiplexer (utilized to obtain the Al(p,p) data).

A block diagram of the data acquisition electronics for the proton detectors is shown in figure 3.3. The silicon surface barrier detectors

Figure 3.3 Block diagram of the proton detection and counting electronics.

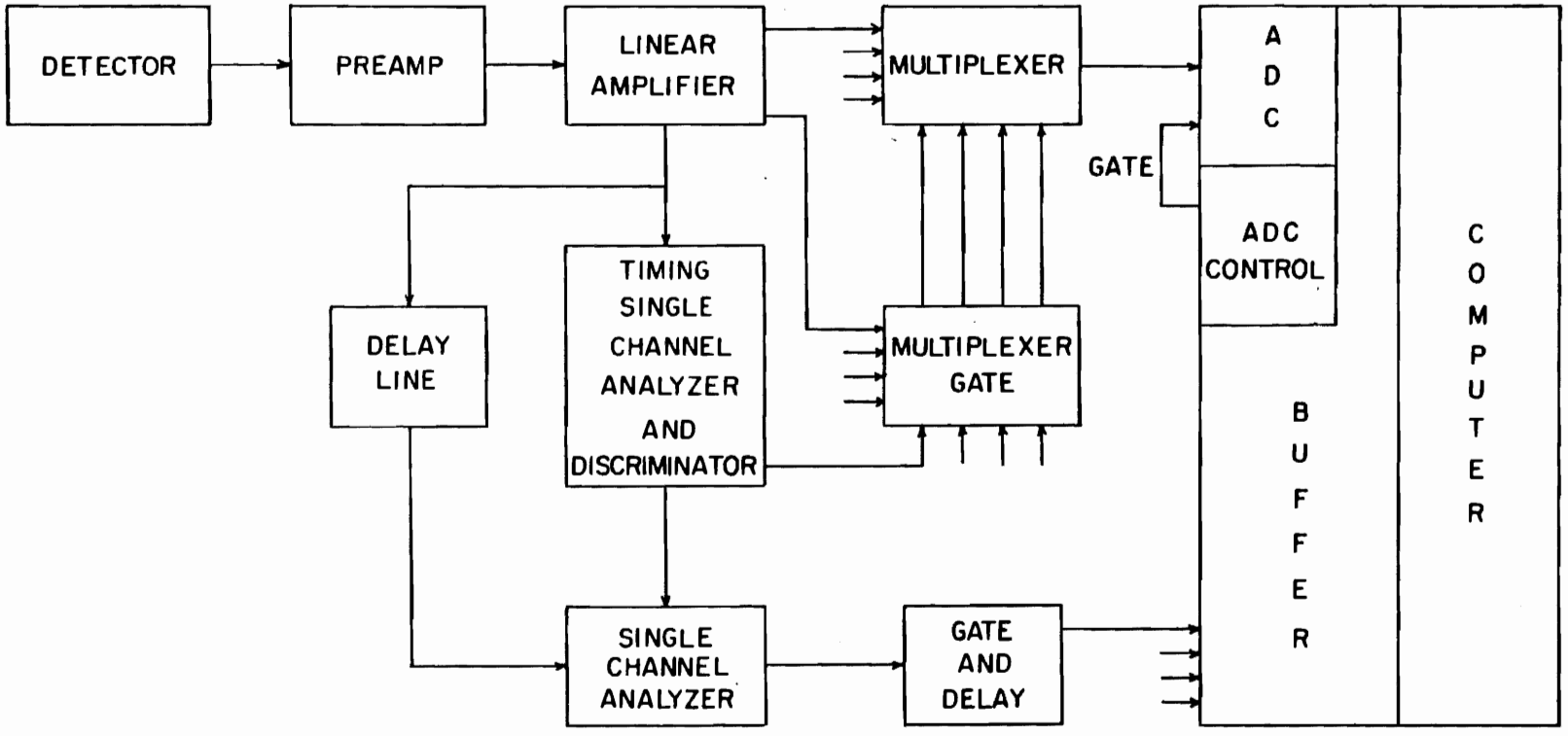
DETECTOR
PREAMP
LINEAR AMPLIFIER
MULTIPLEXER
A D C
GATE
ADC CONTROL
DELAY LINE
TIMING SINGLE CHANNEL ANALYZER AND DISCRIMINATOR
MULTIPLEXER GATE
B U F F E R
C O M P U T E R
SINGLE CHANNEL ANALYZER
GATE AND DELAY

produce a small electrical signal with a pulse height which is proportional to the energy of the incident charged particle. This signal is processed by an Ortec Model 142A Preamplifier with unity gain, and then sent to a spectroscopy amplifier (Ortec Model 572). The gain of the spectroscopy amplifier is adjusted to provide a unipolar output signal between zero and ten volts that is suitable for processing by an analog to digital converter (ADC). The unipolar signals are multiplexed by an Ortec Model 476-8 Multiplexer the output of which is sent to a Northern Model NS-621 ADC.

The spectroscopy amplifiers provide two additional outputs-- a bipolar output which precedes the unipolar output by 2 μs and an inhibit output which is generated whenever the internal circuitry senses distortion of the output due to pulse pileup. The bipolar output is utilized to enable the ADC and buffer to accept a pulse and also to reject the numerous signals from the target backing. The inhibit output may be used to reject pileup events. The high counting rate due to elastic scattering from the carbon target backings is removed to decrease the system dead time (primarily due to the finite ADC conversion time) and to reduce problems with peak broadening. The bipolar output is sent through a 900 ns delay line to a Hewlett Packard Model 5583A Single Channel Analyzer (SCA). The SCA outputs a logic pulse if the input is between the upper and lower level discriminator settings. This logic output is lengthened by an Ortec Model 416A Gate and Delay Generator and applied to the buffer input to signal an event and provide routing information. The bipolar signal is also sent directly to an Ortec Model 551 Timing Single Channel Analyzer and Discriminator (TSCA). The discriminator levels on the TSCA are adjusted so that an output is produced only for input pulse heights within a small range, or "window", around the carbon pulses. This output is used to gate off the HPSCA and also the unipolar output at the multiplexer (via the multiplexer gate) thus

rejecting the signals due to scattering from the carbon backings. If it is necessary to reject pileup events the inhibit output may be applied to the multiplexer gate to reject the pileup signals.

The ADC is operated in the coincidence mode, accepting an input only if it is accompanied by a gate signal. Overlapping signals are rejected by the ADC-buffer interface. Once digitized by the ADC a data point is stored in the buffer memory along with the routing information. The buffer contains two 256 word memory areas so that one 256 word data block may be transferred to computer memory while the second area is being filled. This eliminates dead time due to the computer interrupt cycle time. Finally, the transferred data are sorted into the proper data matrices by the data acquisition program and displayed on a real-time CRT display. Both 256 and 512 channel spectra are available with the present system.

The dE/dx detector electronics operate in a manner similar to the proton detector electronics. Figure 3.4 shows a block diagram of the dE/dx detector electronics. The TSCA discriminators are adjusted to produce an output only for those pulses with a peak height greater than the majority of the proton signals. This output is connected to a gate and delay module to generate the buffer gate and also to enable an Ortec Model 418 Linear Gate. Thus signals predominantly from alpha particle events are sent to the multiplexer and buffer. The inhibit output of the amplifier is sent to the multiplexer gate to remove pileup events from the spectra.

An Ortec Model 439 Current Digitizer measures the beam current incident on the Faraday cup beyond the scattering chamber. The output pulses of the digitizer are counted by a preset scaler which automatically prevents the ADC from acquiring more data upon reaching a preset value. A pulse generated by the ADC-buffer interface gates off the current digitizer to correct for dead time of the ADC and buffer system.

Figure 3.4 Block diagram of the alpha particle detection and counting electronics.

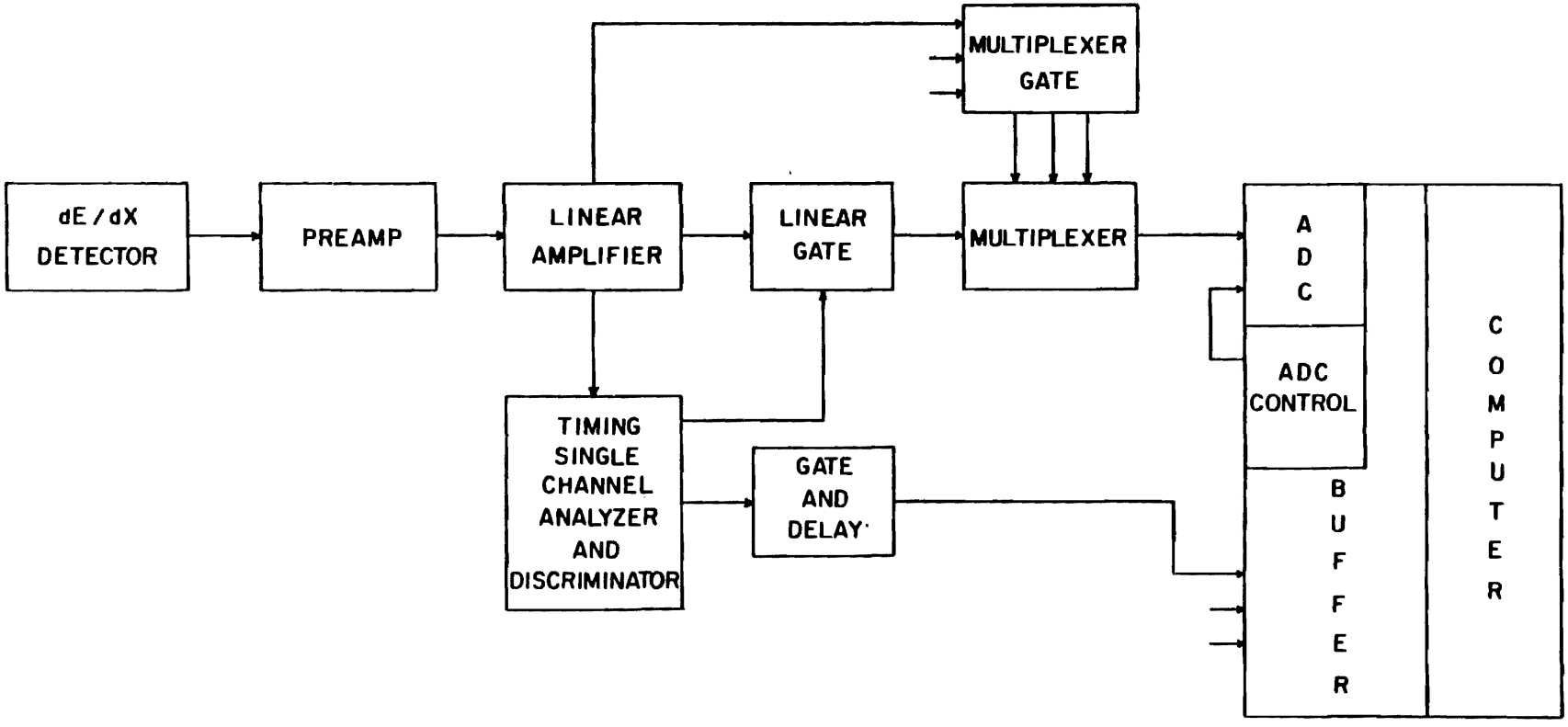
dE / dX
DETECTOR
PREAMP
LINEAR
AMPLIFIER
LINEAR
GATE
MULTIPLEXER
GATE
MULTIPLEXER
TIMING
SINGLE
CHANNEL
ANALYZER
AND
DISCRIMINATOR
GATE
AND
DELAY
A
D
C
ADC
CONTROL
B
U
F
F
E
R
C
O
M
P
U
T
E
R

D. Targets

The ^{29}Si targets consisted of 0.8 to 1.3 $\mu g/cm^2$ of Si enriched to 95.28% in ^{29}Si evaporated onto 2 $\mu g/cm^2$ carbon foils coated with collodion. The isotope was obtained from Oak Ridge National Laboratory in the form SiO_2. The evaporation was performed with a high current evaporator utilizing a closed Ta boat and Ta powder as a reducing agent. Performing the evaporation at temperatures just above the melting point of SiO_2 kept the Ta contamination to a minimum. It is believed that the silicon was deposited in the forms Si and SiO. The electron gun method of evaporation was also tried but appeared to give greater oxygen contamination. The electron gun technique deposits predominantly SiO with some Si and SiO_2 (Holland 1966). Because SiO and SiO_2 are colorless, determination of the target thickness by discoloration of blank glass slides was difficult. A slight difference in the refraction and sometimes a slight yellowish discoloration of the glass slides were the only indications of a successful evaporation for the range of target thicknesses used in this experiment.

The Sloan Vacuum Deposition Meter which became available after these targets were prepared would undoubtedly have made easier the production of targets of suitable thickness. The Sloan meter consists of a quartz crystal oscillator in a bridge circuit. The face of the quartz crystal is exposed to the evaporant resulting in a change in the mass of the crystal and a corresponding change in its frequency of oscillation. This change in frequency is linearly related to the change in areal density and is displayed on the meter.

The very thin C foils (obtained from the Arizona Carbon Foil Co.) were chosen to reduce the high counting rates encountered at 160° due to the strong resonances in $^{12}C(p,p)$ around $E_p = 1.74$ MeV. The carbon foils were coated with collodion, which burns off in the proton beam, to provide

strength during the evaporation and handling. The collodion was applied to the C coated slides by dipping the slides in a mixture of 10 parts amyl acetate to 1 part flexible collodion.

The production of ^{27}Al targets was relatively easy. Pure Al metal is very inexpensive and has a moderately low melting point, and natural Al is monoisotopic. A high current evaporator with an open Ta boat melted small pieces of pure Al wire, with the evaporant deposited on 2 $\mu g/cm^2$ collodion coated C foils and also on uncoated 5 $\mu g/cm^2$ C foils. Target thicknesses were 0.6 to 1.4 $\mu g/cm^2$, in good agreement with results from the Sloan meter. The only major contaminant was oxygen from oxidation of the Al upon exposure to air.

For all evaporations a Ta aperture and shutter were positioned above the boat to shield the foils from heat and damage while the target material was outgassed. Glass slides were placed on top of the foils to ensure that no material was deposited on the back side of the targets. Both the Si and Al targets were uniform and stable in the proton beam.

Typical spectra for these experiments are shown in figures 3.5 and 3.6. Except for the low energy ^{29}Si spectrum the ^{12}C peaks have been gated out.

E. Procedure

All of the data in these experiments was measured at least twice. This ensured reproduciblity and permitted improvement of the equipment and procedures between runs. Data were taken in steps of 400 eV or less on the first pass through all energies. On subsequent passes the maximum step size was 600 eV. When near or on a small resonance the step size was 100 or 200 eV.

To minimize energy shifts (Wilson 1973) the analyzer was usually

Figure 3.5 Typical proton spectra from the $^{29}Si(p,p)$ experiment. The ADC conversion gain was 1024 in the lower energy spectrum and the ^{12}C peak was not gated out. In the higher energy spectrum the ADC gain was 512 and the ^{12}C peak was gated out.

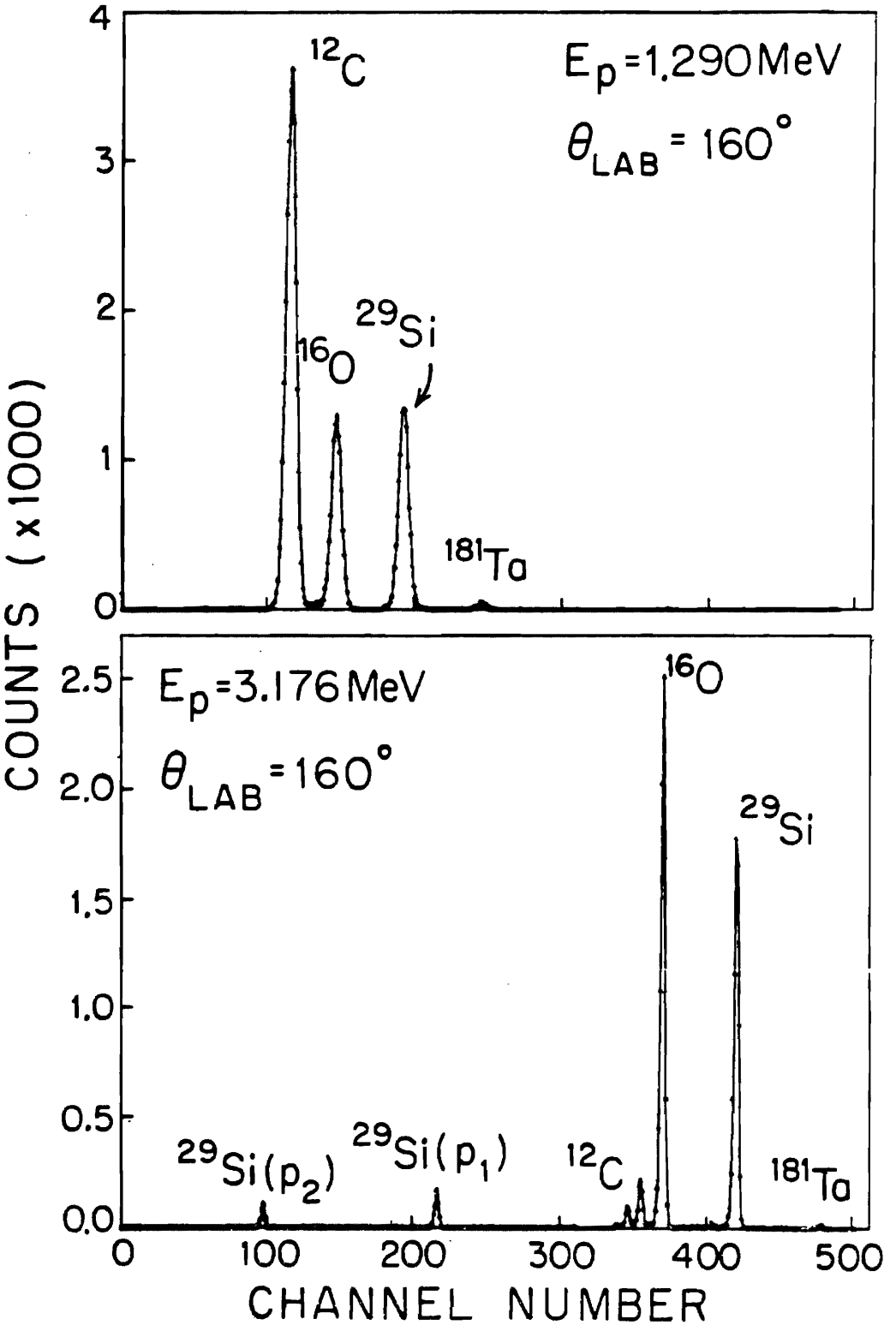
^{12}C
E_p=1.290MeV
θ_{LAB} = 160°
^{16}O
^{29}Si
^{181}Ta
E_p=3.176MeV
θ_{LAB}=160°
^{16}O
^{29}Si
$^{29}Si(p_2)$
$^{29}Si(p_1)$
^{12}C
^{181}Ta
COUNTS (x1000)
CHANNEL NUMBER
0
100
200
300
400
500
0.0
0.5
1.0
1.5
2.0
2.5
1
2
3
4

Figure 3.6 Typical spectra for proton scattering from ^{27}Al. The top spectrum shows the pileup which remains after inhibit gating. At this energy the pileup is above the alpha decay peak in the spectrum. The lower figure is from a transmission detector. Almost all of the proton signals were gated out of this spectrum.

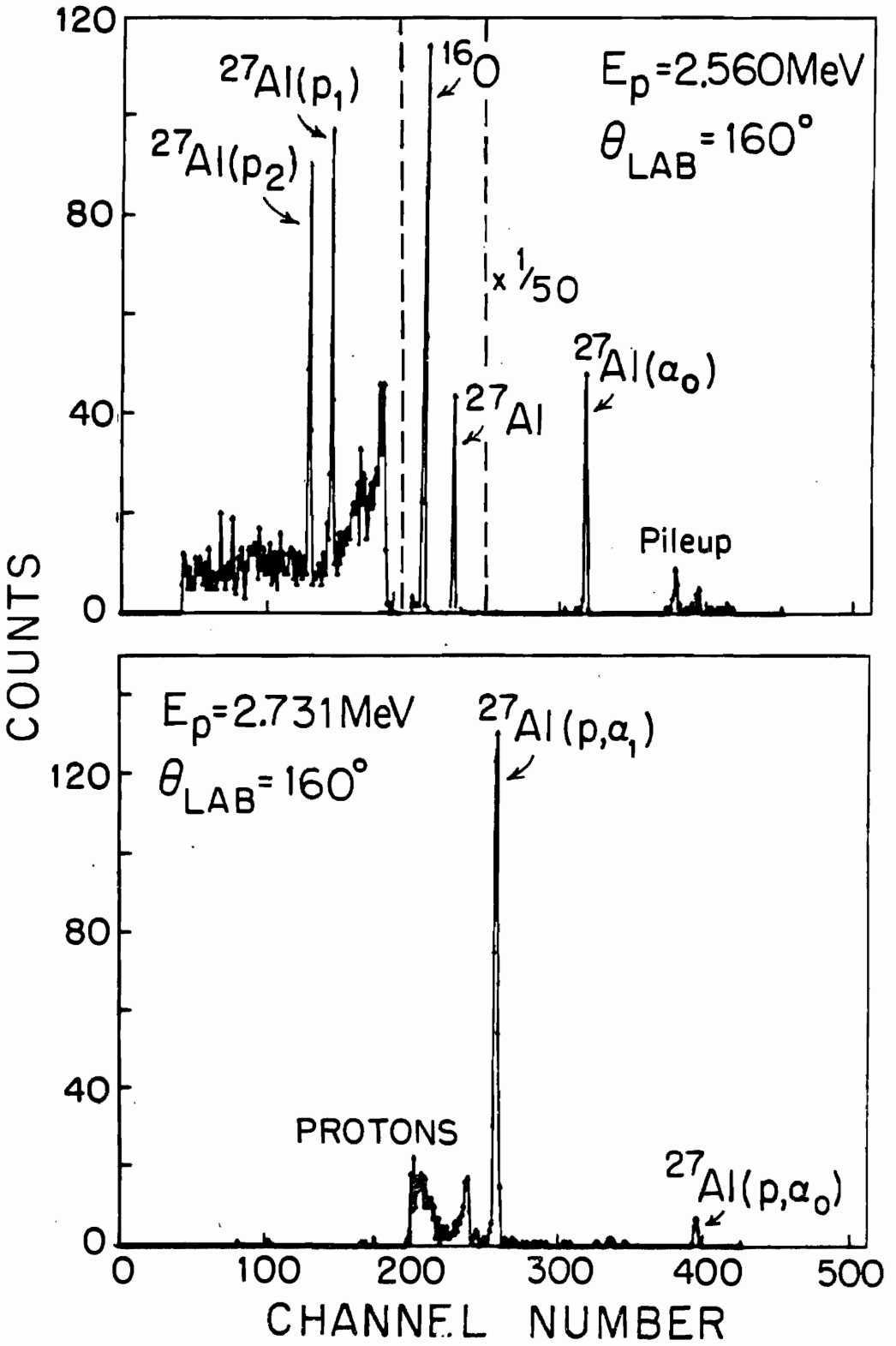
120
80
40
0
COUNTS
$^{27}Al(p_1)$
$^{27}Al(p_2)$
^{16}O
E_p=2.560MeV
θ_{LAB}=160°
x 1/50
^{27}Al
$^{27}Al(\alpha_0)$
Pileup
E_p=2.731MeV
θ_{LAB}=160°
$^{27}Al(p,\alpha_1)$
PROTONS
$^{27}Al(p,\alpha_0)$
0
100
200
300
400
500
CHANNEL NUMBER

allowed to "warm up" for a few hours before data was acquired and, if possible, data were taken continuously from the lowest energy to the highest. When extending a data set to other energies at least one resonance was overlapped in the previous data to fix the energy scale of the new data set.

Targets were usually replaced only when broken. Normally a small energy region was repeated to allow determination of the change in target thickness. Repetition of an energy region was especially necessary when a target broke while data was being taken on or very near a resonance.

For the ^{29}Si experiment the data acquisition program displayed the current spectrum for each angle. In addition, the program summed up to two peaks from each spectrum, including a simple background subtraction, and displayed the resulting yield curve for online monitoring of the data. The energies, run numbers, and spectra were written on magnetic tape for later, more careful analysis. An energy calibration of the spectra and a kinematics subroutine allowed automatic energy shifting of the summed windows with the peaks of interest. The spectrum length was 512 channels for this experiment.

At low energies the Si and O peaks were not well separated in the 90^{o} and 105^{o} spectra. To make the background subtraction easier and setting of the windows less critical, the ADC conversion gain was increased to 1024 to spread the peaks over more channels. At higher energies where inelastic decay was present the conversion gain was reduced to 512 to retain all of the peaks in the spectrum over as large an energy range as possible.

The data acquisition program was expanded for the ^{27}Al experiment to display yield curves for up to three groups at seven angles. The three proton groups were monitored at four angles and the two alpha groups were displayed at the other three angles. Below 1.68 MeV the ADC conversion gain

was 1024. At higher energies the ADC gain was reduced to 512. The spectrum size was 512 channels throughout the experiment.

For both of the experiments typical beam currents of 3 to 6 μA and counting times of 30 to 60 seconds yielded 1 to 2 % counting statistics off of resonance. This corresponded to 100 to 200 μC of integrated charge per point. Around the strong $^{12}C(p,p)$ resonances near 1.74 MeV the beam in the Al study was decreased to 200 to 500 nA to reduce the ^{12}C pulse pileup at 135^{o} and 160^{o}. This pileup overlapped with the peak from $^{27}Al(p,\alpha)$ decay and was not rejected by the amplifier inhibit output due to the almost exact overlap of the pulses.

CHAPTER IV

DATA REDUCTION AND PRIMARY ANALYSIS

A. Preparation of Yield Curves

The yields of the appropriate peaks were extracted from the spectra on magnetic tape with a modified version of the yield curve generating program originally written by Outlaw (1974). This program reads a set of spectra from the data tape, sums the counts in the channels covered by the peak or peaks, subtracts a background, and displays the resulting yield curve. This yield curve may then be transferred via magnetic tape to another computer for R-matrix analysis.

The channels over which the sums are performed (the windows) are automatically shifted in energy by a relativistic kinematics subroutine to remain centered on the elastic scattering peaks. Although these energy shifts are only approximately correct for the inelastic scattering peaks and the alpha decay peaks, the difference was noticeable only for the alpha decay peaks. The alpha decay windows were shifted manually from time to time to keep them centered on the peaks.

The background in the spectra around the elastic scattering peaks for Al and Si was usually less than 2% of the total number of counts in the peak. A simple average of two sample background points from each side of the peak was employed to determine the background to be subtracted from these peaks. For the alpha decay to the ground state of ^{24}Mg there was essentially no background present except in the energy region where overlap occurred with the pileup from proton elastic scattering. The peaks due to

inelastic scattering of protons were always located on a continuous low energy background. At times this background was comparable in size to the relatively weak inelastic scattering peaks.

Watson (1980) incorporated a routine into his yield curve generating program which fit a functional form to a large number of background points in order to determine the background to be subtracted. This method of background subtraction is necessary if the inelastic peak is not separated from other large peaks in the spectrum. However, for inelastic peaks that are located on a relatively flat portion of the background it was found that the local background could vary significantly from the average background. These variations give rise to excessive point scatter when utilizing a general background fit to extract the inelastic yields. Thus all of the inelastic yields were obtained with a simple background subtraction which averaged two points on each side of the inelastic peak and subtracted this average background from the total number of counts in each channel of the peak.

1. Energy Calibrations

The energy calibrations for $^{29}Si(p,p)$ were based on the $^{7}Li(p,n)$ threshold at 1.8806 MeV and the $^{13}C(p,n)$ threshold at 3.2357 MeV (Marion 1966). The lower energy calibration was performed by locating a secondary standard, an s-wave resonance at 1.8440 MeV in $^{44}Ca(p,p)$ (Wimpey 1974), calibrating the analyzer system at this energy, and then locating the 1.7715 MeV f-wave resonance in $^{29}Si(p,p)$. This f-wave resonance was chosen because it was the nearest resonance to the calibration point which possessed a width that was small enough to serve as a precise energy reference. The higher energy calibration was performed as an additional check since fairly large energy differences had been observed between these data and previous results (Poirier 1970).

The $^{13}C(p,n)$ threshold was measured at 0^{o} and a secondary standard was located in $^{56}Fe(p,p)$. The energy of the 44 eV d-wave resonance, analyzed by Watson (1980) at E_p = 3.2386 MeV, was determined to be E_p = 3.2369 $\pm$ 0.0004 MeV. The $^{13}C(p,n)$ threshold was fit (Westerfeldt 1981) utilizing a program (Wilkerson 1982) based on the technique of Marion (1966). The silicon energy scale calibration was performed by locating the f-wave resonance at 3.2451 MeV in $^{29}Si(p,p)$ relative to the secondary standard in $^{56}Fe(p,p)$.

The first step in the calibration procedure was to make the corrections (Westerfeldt 1977) for the target rod bias, relativistic effects, and the energy offset in the data at the lower energy calibration point. After the first corrections, the difference between the higher energy calibration and the data was found to be about -4.6 keV. The energies were scaled linearly to match both calibration points. The maximum absolute energy error away from the calibration points is estimated to be $\pm$3keV.

The $^{27}Al(p,p)$ energies were calibrated from the $^{27}Al(p,p)$ resonance at E_p = 991.90 $\pm$ 0.04 keV (Roush 1970), and from the resonance at E_p = 1799.75 $\pm$ 0.09 keV (Maas 1978). Both of these resonances have total widths of less than 200 eV and serve well as calibration points. The calibration procedure was the same as that used for the $^{29}Si(p,p)$ data. First the corrections for the target rod bias, relativistic effects, and energy offset at the lower energy calibration point were made. The correction equations are those given by Adams (1983) for the double-sided analyzer operation used in this experiment. After the initial corrections, the higher energy data were again found to be several keV low in energy, and the energies were scaled linearly to match both calibration points. The maximum error away from the calibration points is estimated to be $\pm$3 keV. The consistently low values for the higher energy data before scaling probably indicate error in the DVM linearity and accuracy.

2. Correction for Isotopic Impurities

For elastic scattering from ^{27}Al there were no appreciable contaminants. However, for elastic scattering from ^{29}Si a significant fraction of the observed cross section was due to ^{28}Si elastic scattering. The isotopic target material contained 4.35% ^{28}Si and 0.36% ^{30}Si. Additional contamination of natural Si (92.2% ^{28}Si) occurred during target preparation. The approximate percentage of ^{28}Si in the targets was determined from the measured yield of the strong inelastic decay (to the first excited state of ^{28}Si) of the resonance at E_p = 3.1 MeV in $^{28}Si(p,p)$ (Vorona 1959). The areal density of ^{28}Si atoms in the target can be calculated from the measured number of counts per unit solid angle, the incident proton flux, and the cross section for the reaction. The cross section for inelastic scattering from the E_p = 3.1 MeV state in $^{28}Si(p,p')$ was calculated by MULTI from the resonance parameters listed by Endt (1978). The amount of ^{28}Si in the targets was determined to be about 7%. The E_p = 3.1 MeV resonance in ^{28}Si also served to fix the energy scale for the background subtraction.

The elastic scattering cross section for $^{28}Si(p,p)$ was calculated with MULTI assuming the resonance parameters listed by Endt (1978) in the energy range E_p = 1.2 to 3.5 MeV. From the ratio of the resonance cross section to the Rutherford cross section, the target thickness and the percentage of ^{28}Si in the target, the background due to $^{28}Si(p,p)$ could be calculated at each energy.

Since the resonances in $^{28}Si(p,p)$ are very broad the background was slowly varying and the details of the subtraction procedure were not critical. Background due to the 0.36% ^{30}Si was neglected. The only evidence of this contaminant was the appearance of a very small peak in the 160° cross section at E_p = 2.187 MeV due to an f-wave analog state (Outlaw

1974) with a differential cross section of over one barn.

B. R-Matrix Fitting Procedure

The R-matrix fitting code MULTI has evolved from a program written by Sellin (1968) based on the differential and total cross section expressions of Lane and Thomas (1958). The program accepts as input the fixed parameters (for both the entrance and exit channels) such as the projectile and target masses and charges, the reaction Q-values, the allowed channel spins and orbital angular momenta, etc., and the variable parameters which describe the resonances such as the energies, angular momenta, channel spins, orbital angular momenta, and widths. The cross section calculation includes Coulomb, hard sphere, and resonance scattering contributions.

In order to accomodate the large number of possible entrance and exit channels, spins, and observed decay channels, the program was expanded. Current dimensions allow 300 levels, 12 J^{π} values, 5 groups of decay channels, ℓ values up to 5, and up to 10 channels for a given J^{π} with a limit of 70 total channels for all J^{π}s. The full size of the current program was necessary to fit the resonances in ^{28}Si. Any of these restrictions may be lifted, if necessary, since the TUNL DEC VAX 11/780 computer does not limit the memory required for program execution. However, the present calculations typically required from one to fifteen minutes of CPU time for a single calculation of the cross sections, thus for a program of this size fitting interactively is a slow process on a time-shared system.

Since the hard sphere phase shifts are calculated only for the spins and parities included in the input of MULTI care must be taken to include all spins and parities for which potential scattering is appreciable. In this analysis the spins for s-wave scattering and p-wave scattering were

always included even though the p-wave phase shifts are negligible at the lower energies.

As discussed in chapter II, the collision matrix is formed with the boundary condition parameter chosen identically equal to the shift function for each resonance. This choice of boundary conditions places the apparent resonance energy exactly at the R-matrix energy eigenvalue position. For a single isolated resonance this procedure gives the least error in extracting the physical information from the fit. However, for overlapping resonances this choice of boundary conditions introduces an incorrect energy dependence in the shift functions. The net effect is to introduce an error in extracting the widths of the resonances. The program also allows the boundary condition parameter to be fixed equal to the shift function at the center energy of the fit region. This condition changes the value of the shift function away from the center energy, and thus the apparent resonance positions vary, depending on the energy region chosen and the ℓ values of the resonances. The widths extracted for a fixed boundary condition are also dependent on the choice of the boundary condition parameter in the multi-level case. Both methods of fixing the boundary were compared and gave about the same values of the widths for reasonable choices of the fitting regions in the present data. Since fixing the boundary condition parameter at each resonance is more convenient, due to the correspondence of the energy eigenvalues and the apparent resonance positions, this type of boundary condition was employed in all of the present analyses.

The cross sections calculated by MULTI were convoluted with a resolution function to simulate the energy loss in the target and the other factors which degrade resolution. A function was chosen which could be conveniently calculated and which empirically reproduced the observed resolution function. The function consisted of a Lorentzian leading edge

curve with a trailing edge Gaussian curve. The resolution function was specified by the Gaussian FWHM and the ratio of the Lorentzian FWHM to the Gaussian FWHM. These quantities were determined by fitting a very small resonance (preferably an inelastic decay peak or an $\ell = 2$ or 3 resonance possessing a total width much smaller than the resolution function) for which the observed shape is essentially just the resolution function. This resolution function was then kept constant while fitting a region of data.

The general fitting procedure consisted of calculating the differential cross sections for a set of resonance parameters, comparing this fit visually with the data, then adjusting the resonance parameters and recalculating the cross sections until the best possible fit was obtained. The resonance parameters adjusted included the resonance energy, angular momentum, and the magnitudes and phases of the reduced width amplitudes for the allowed values of channel spin and orbital angular momentum.

At lower energies, where the off-resonance cross sections were predominantly Rutherford, the data were normalized to the fit by the sums of the areas under the calculated and experimental excitation functions. At higher energies, where the background is largely due to the resonances in the region, normalizing the data to the fit leads to normalizations which are often strongly dependent on the resonance parameters utilized in a particular fit. To avoid this problem the normalizations were fixed at the values determined at lower energies except where corrections were necessary due to a change of target thickness. Only after all of the larger resonances were fit well could the smaller resonances be fit.

^{29}Si was the first target with non-zero spin for which elastic scattering analysis was carried out at our laboratory. Thus this was the first case for which channel spin mixing and orbital angular momentum mixing

were allowed in the elastic scattering channels. The data for proton scattering from ^{27}Al are the most complex data ever analyzed in terms of the number of observed decay channels and the number of possible mixings and resonance spins. Because of this complexity there was sometimes more than one possible solution found to fit a resonance. The level of ambiguity depended, of course, on the amount of information available from the observed decay channels (and possibly from other experimental data). A great deal of effort was required to attempt to determine all possible solutions for each resonance. For isolated resonances this goal could be achieved. In the more complicated higher energy regions the resonance interference and the large number of combinations of widths and relative phases made the determination of all possible solutions extremely difficult. The difficulty in finding a single satisfactory fit, due to the interference between resonances, may indicate uniqueness for some of the fits in this region, although other possible successful combinations of resonance parameters may have been missed. In general, the errors of the resonance parameters are larger in the higher energy regions.

Due to the poor statistics for the reaction channel data the information available from the angular distributions of these decay products was not maximal. However, in many cases the available angular distributions were adequate to distinguish between different solutions and to aid in determining mixing ratios. Of course, if there is sufficient interest in any given resonance, the angular distributions can be accurately measured, and coincidence or polarization experiments can be performed to determine the mixing ratios and relative phases of the reduced width amplitudes.

1. Analysis of Resonances in ^{30}P

For proton scattering from ^{29}Si at incident proton energies below 3.3 MeV there are 5 open particle decay channels. These include elastic

scattering and inelastic scattering to the first four excited states of ^{29}Si. Only the elastic scattering and inelastic scattering to the first two excited states have appreciable yields in the energy range studied. The higher inelastic decays are inhibited due to the low penetrabilities, although the third inelastic yield may begin to be important at the highest energies studied. The penetrabilities for elastic scattering and inelastic decay to the first excited state of ^{29}Si are shown in figure 4.1. Gamma decay is neglected since electromagnetic decay widths are usually extremely small compared to particle decay widths.

Combining the spin of the proton with the ground state spin 1/2 of ^{29}Si gives entrance channel spins of 0 and 1. In the case of ^{29}Si, which has positive parity for the ground state, channel spin mixing is allowed only for resonances with natural parity ($\Pi = (-1)^J$) and orbital angular momentum mixing occurs only for unnatural parity resonances ($\Pi = (-1)^{J+1}$). Since the first excited state of ^{29}Si has spin 3/2, the inelastic decay has exit channel spins of 1 and 2. For decay to the second excited state, with spin 5/2, the exit channel spins are 2 and 3. For the nonelastic exit channels both channel spin mixing and ℓ-mixing are allowed (although not for all values of J^π). The allowed entrance and exit channels are listed in table 4.1.

For elastic scattering the channel spin mixing ratio is defined as

$$\xi = \Gamma_{p,\, s=1,\, \ell} \,/\, \left[\Gamma_{p,\, s=0,\, \ell} + \Gamma_{p,\, s=1,\, \ell}\right]$$

and the ℓ-mixing ratio is

$$\varepsilon = \pm\sqrt{\Gamma_{p,\, s=1,\, \ell+2} \,/\, \Gamma_{p,\, s=1,\, \ell}}$$

where $\Gamma_{p,\, s,\, \ell}$ is the laboratory width for elastic scattering of the ℓ^{th}

Figure 4.1 Coulomb penetrabilities versus energy for the $^{29}Si(p,p)$ and (p,p_1) reactions. The top horizontal axes list the exit energies at which the penetrabilities were calculated. The bottom horizontal axes give the corresponding incident proton energies.

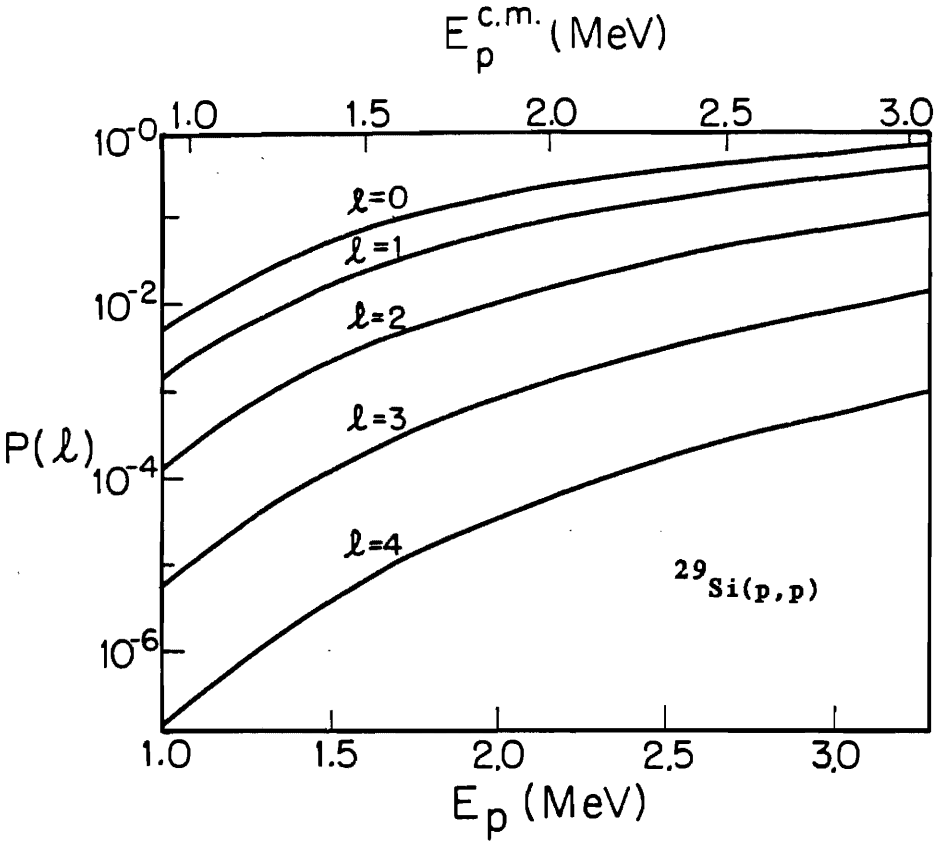
$E_p^{c.m.}$ (MeV)
1.0
1.5
2.0
2.5
3.0
10^{-0}
10^{-2}
10^{-4}
10^{-6}
P(ℓ)
ℓ=0
ℓ=1
ℓ=2
ℓ=3
ℓ=4
^{29}Si(p,p)
1.0
1.5
2.0
2.5
3.0
E_p (MeV)

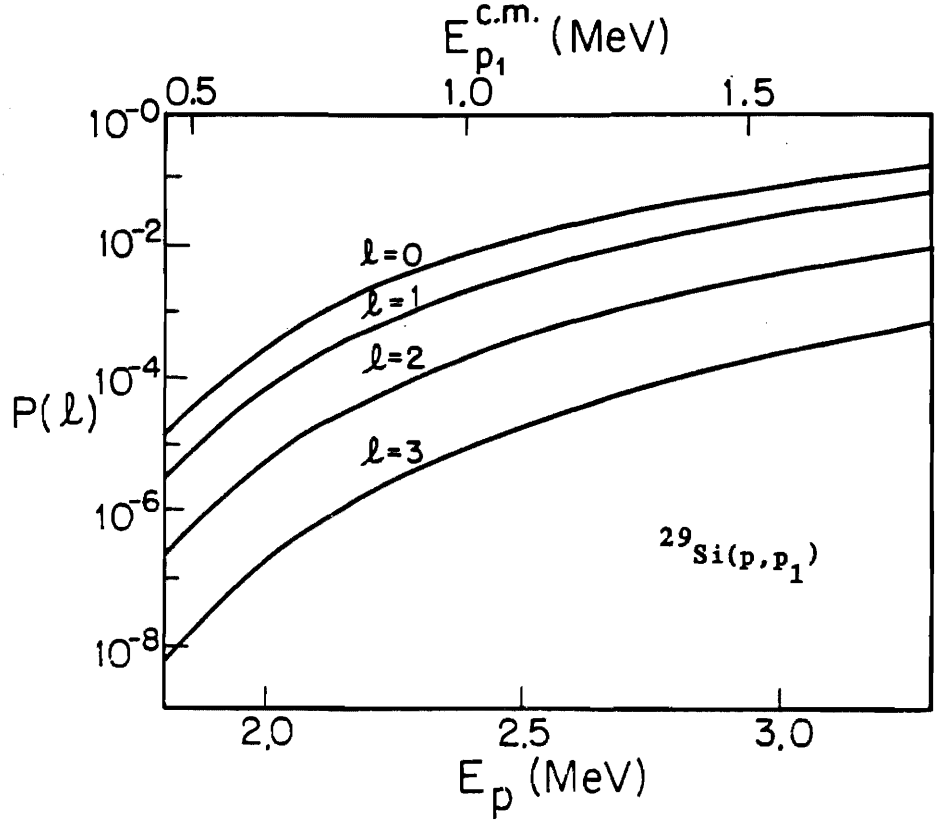
$E_{p_1}^{c.m.}$ (MeV)
0.5
1.0
1.5
10^{-0}
10^{-2}
10^{-4}
10^{-6}
10^{-8}
P(ℓ)
ℓ=0
ℓ=1
ℓ=2
ℓ=3
^{29}Si(p,p_1)
2.0
2.5
3.0
E_p (MeV)

TABLE 4.1

ALLOWED ENTRANCE AND EXIT CHANNELS FOR RESONANCES IN ^{30}P

	p_0		p_1		p_2	
J^π	ℓ	s	ℓ	s	ℓ	s
0^+	0	0	2	2	2	2
0^-	1	1	1	1		
1^+	0	1	0	1	2	2
	2	1	2	1	2	3
			2	2		
1^-	1	0	1	1	1	2
	1	1	1	2		
2^+	2	0	0	2	0	2
	2	1	2	1	2	2
			2	2	2	3
2^-	1	1	1	1	1	2
	3	1	1	2	1	3
			3	1		
			3	2		
3^+	2	1	2	1	0	3
			2	2	2	2
					2	3
3^-	3	0	1	2	1	2
	3	1	3	1	1	3
			3	2		
4^-	3	1	3	1	1	3
			3	2		

partial wave with channel spin s. Thus, ξ varies between zero for pure s = 0 and unity for pure s = 1, while ε is zero for formation with only the lowest ℓ value, and is infinite for formation with pure $\ell + 2$. For convenience we also define an ℓ-mixing angle, Ψ, as

$$\tan(\Psi) = \varepsilon$$

so that Ψ varies from -90^{o} to $+90^{o}$. For the n^{th} inelastic group the channel spin mixing ratio is defined as

$$\xi_n = \sum_{\ell} \Gamma_{p_n, s_>, \ell} \; / \; \Gamma_{p_n}$$

where $s_>$ is the higher channel spin and Γ_{p_n} is the total inelastic width in the n^{th} channel. The two exit ℓ mixing ratios are defined as

$$\varepsilon_{ns} = \pm\sqrt{\Gamma_{p_n, s, \ell+2} \; / \; \Gamma_{p_n, s, \ell}}.$$

The corresponding mixing angles are

$$\tan(\Psi_{ns}) = \varepsilon_{ns}.$$

For a given group, p_1 for example, the ℓ-mixing ratios and the channel spin mixing ratio together with the width Γ_{p_1} serve to parameterize all of the partial widths of a resonance. For scattering of an unpolarized beam from an unpolarized target, ℓ-mixing is a coherent process while channel spin mixing is incoherent. These mixing ratios are defined so that these natural coherence properties are exploited.

From the penetrabilities in figure 4.1, the laboratory widths for higher ℓ values will, on the average, be smaller than those for lower ℓ

values. In addition, the Wigner limit on the reduced widths ensures that ℓ-mixing will be small except at the higher energies studied or for very small resonances at lower energies.

The resonance shapes for elastic scattering from ^{29}Si are shown in figure 4.2 for each channel spin and for ℓ values up to 3. It is important to note that the resonance shapes for channel spin 1/2, encountered in elastic scattering from zero-spin targets, are qualitatively similar to the shapes for channel spins 0 and 1 for a given ℓ value. The general features of the resonance shape for each ℓ value are also independent of the resonance spin. A dip in the 90° excitation function indicates positive parity for a resonance while a rise in the cross section denotes a resonance with negative parity. Both s-wave and p-wave resonances have similar shapes at 160°, dipping on the lower energy side and then rising at higher energies. The 160° excitation function for d-wave resonances rises at the lower energies and then falls off sharply at higher energies, while f-wave resonances give almost symmetrical peaks at 160°. The p-wave resonance with channel spin zero has a somewhat unusual shape for a p-wave resonance, but the shape is distinctive and thus can not be confused with the shape for any other ℓ value.

The combination of the 90° and 160° data is almost always sufficient to determine the ℓ value of a resonance. The differences in shapes for the two channel spins are especially noticeable for p-wave and f-wave resonances, but are not as striking for d-wave resonances. The combination of the 135° and 160° data was very useful in determining the channel spin admixtures. The 105° data aid in determining the spins of p-wave resonances. The data from all four angles were necessary to determine the best solution in the regions with many overlapping levels. The spin of a resonance could usually be determined from the cross sections because the difference in the maximum

Figure 4.2 Theoretically calculated excitation functions for proton elastic scattering from ^{29}Si at four angles. Shapes for ℓ = 0, 1, 2, and 3 resonances are shown for each channel spin with the resonance strength, $(2J+1)\Gamma_p^{\gamma}$ = 1.0 keV for all cases. The 160° cross sections for d-wave, and f-wave resonances have been reduced by a factor of 1/2. The energy axis tick marks are at 5 keV intervals. Note the supressed zero of the cross sections.

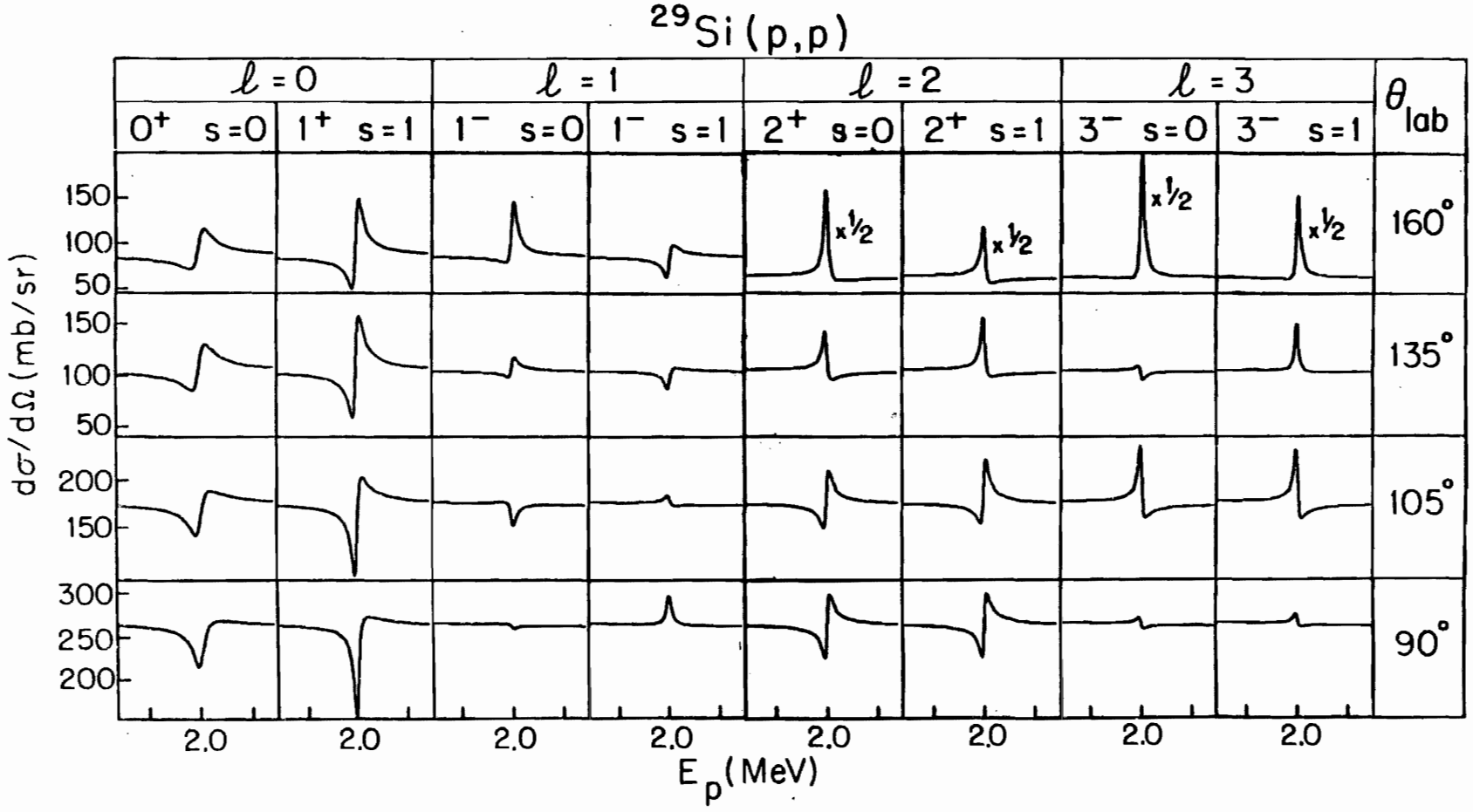
^{29}Si (p,p)
ℓ = 0
ℓ = 1
ℓ = 2
ℓ = 3
θ lab
0+ s=0
1+ s=1
1− s=0
1− s=1
2+ s=0
2+ s=1
3− s=0
3− s=1
160°
135°
105°
90°
x 1/2
dσ/dΩ (mb/sr)
150
100
50
200
150
300
250
200
2.0
E p (MeV)

and minimum values of the cross section depend on $(2J + 1)\Gamma_p$. Of course the spins could not be determined for resonances possessing widths smaller than that of the resolution function, because the finite resolution removed most, or all, of the differences in the cross sections between the various spins.

An example of channel spin mixing for a p-wave resonance is shown in figure 4.3. The lower cross section of the best fit is the result of channel spin cross terms in the expression for the differential scattering cross section. Figure 4.4 shows the $J^\pi = 1^+$, ℓ-mixed resonance near 2.95 MeV. The best fit has the same relative phase for the $\ell = 0$ and the $\ell = 2$ reduced width amplitudes. The fit with opposite relative phase is obviously much poorer. Part of the difference between these fits is due to interference with surrounding resonances.

As discussed in chapter II, coherent interference effects were observed in the elastic scattering cross section, especially between the large, $J^\pi = 1^-$, channel-spin-mixed resonances. Such interference effects can occur in elastic scattering only for resonances for which two or more elastic scattering channels are open. Thus this type of interference was not encountered in the analysis of elastic scattering data from zero-spin targets. Coherent interference between resonances in the reaction channels is also observed.

The broad, overlapping resonances at higher energies were fit in regions as large as 300 keV. To reduce the computation and plotting time, and to keep the number of fit points from exceeding the limit of 1000, large (up to 1.6 keV) energy steps were used in calculating the theoretical cross sections, and correspondingly only every third or fourth data point was read by the program. After satisfactory fits were obtained for the large resonances, the smaller resonances were then fit in sections as small as 10 keV. Final fits were generated in approximately 150 keV sections. All data

Figure 4.3. The excitation function and best R-matrix fit with a channel spin mixing ratio of 0.45 for the $J^{\pi} = 1^{-}$ resonance at E_p=1.799 MeV. The fits for pure channel spins are much poorer. For clarity the two small resonances near E_p = 1.77 MeV have been omitted from the fits with pure channel spins.

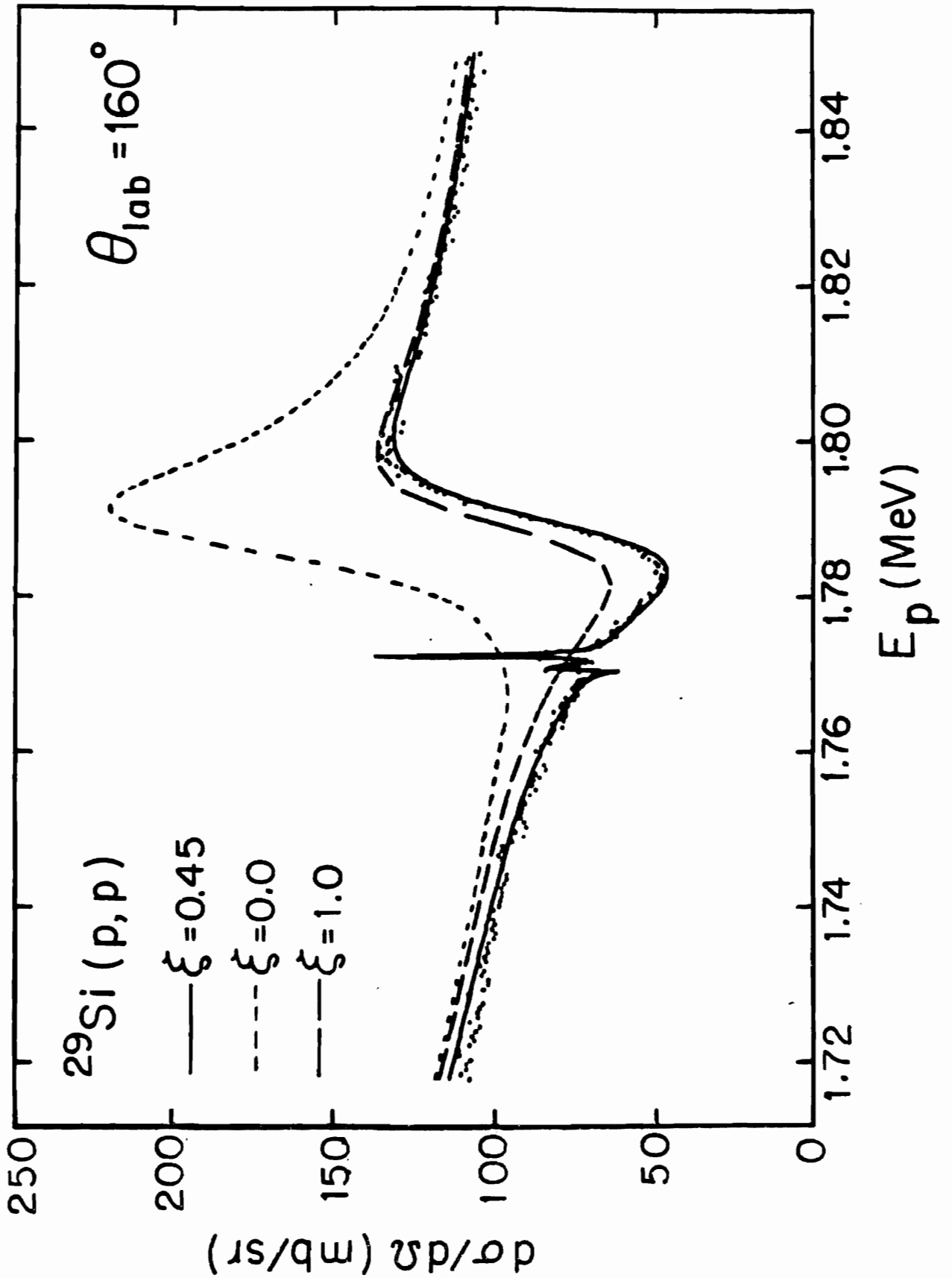
θ_{lab} =160°
^{29}Si (p,p)
ξ=0.45
ξ=0.0
ξ=1.0
dσ/dΩ (mb/sr)
250
200
150
100
50
0
1.72
1.74
1.76
1.78
1.80
1.82
1.84
E_p (MeV)

Figure 4.4. The excitation function and R-matrix fits for the ℓ mixed, $J^{\pi} = 1^{+}$ resonance near $E_p = 2.95$ MeV. The best fit was obtained with the same relative phase for the reduced width amplitudes of the two ℓ values.

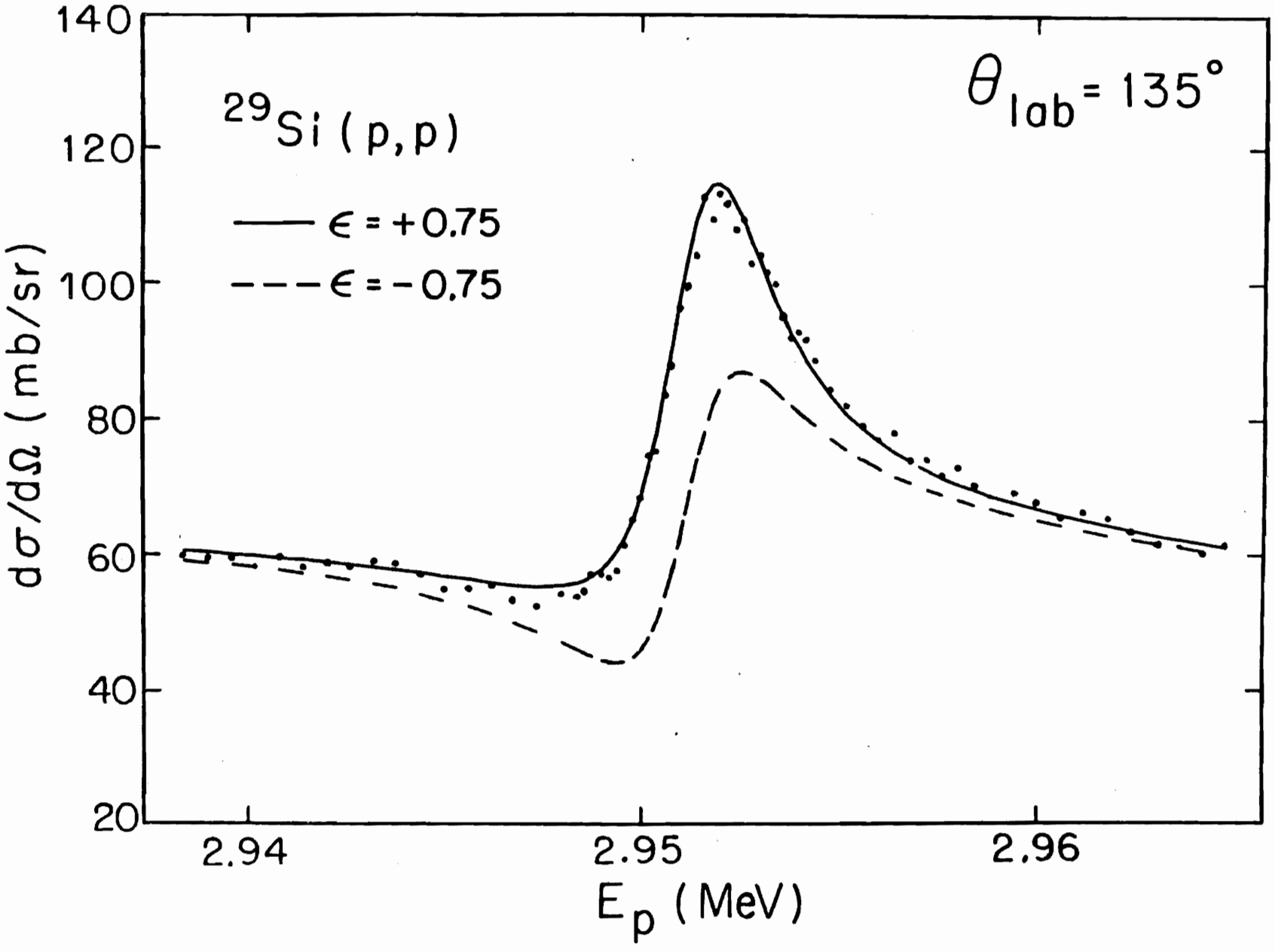
140
120
100
80
60
40
20
^{29}Si (p,p)
θ_{lab} = 135°
ϵ = +0.75
ϵ = −0.75
dσ/dΩ (mb/sr)
2.94
2.95
2.96
E_p (MeV)

points were included in the final fits and all resonance parameters were included in the input when producing the final fits.

2. Analysis of Resonances in ^{28}Si

For proton scattering from ^{27}Al at energies below 3.5 MeV, there are 11 open particle decay channels. These include: elastic scattering, inelastic scattering to the first six excited states of ^{27}Al, and alpha decay to the ground state and the first three excited states of ^{24}Mg. Only elastic scattering, inelastic scattering to the first two excited states of ^{27}Al, and alpha decay to the ground and first excited state of ^{24}Mg were measured in this experiment. For the unmeasured open channels the penetrabilities are extremely small below 3.5 MeV except for inelastic decay to the third excited state of ^{27}Al. These higher inelastic decays have noticeable yields only near the highest energies studied, and were neglected, as was the capture process.

The ^{27}Al data were analyzed in three sections. Below 1.7 MeV only the elastic and α_0 channels were necessary to fit the data. Between 1.7 and 2.7 MeV the inelastic decay to the first two excited states of ^{27}Al was also important in the analysis. Above 2.7 MeV all five of the measured channels were included in the analysis.

The R-matrix analysis of these data was more difficult than that of the $^{29}Si(p,p)$ experiment. The ground state spin 5/2 of ^{27}Al gives entrance channel spins of 2 and 3. For f-wave resonances these entrance channel spins give possible resonance spins from 0 to 6. In addition, for many of the possible spins both channel spin mixing and ℓ-mixing can occur in elastic scattering. The allowed entrance and exit channel parameters for the observed decay modes are listed in table 4.2. From penetrability considerations the ℓ values in table 4.2 are less than 4 for all of the proton channels and for the α_1 channel. The α_0 channel has channel spin 0

TABLE 4.2

ALLOWED ENTRANCE AND EXIT CHANNELS FOR RESONANCES IN ^{28}Si

J^π	p_0		p_1		p_2		α_0		α_1	
	ℓ	s	ℓ	s	ℓ	s	ℓ	s	ℓ	s
0^+	2	2	0	0	2	2	0	0	2	2
0^-	3	3	1	1	1	1				
1^+	2	2	0	1	0	1			2	2
	2	3	2	1	2	1				
					2	2				
1^-	1	2	1	0	1	1	1	0	1	2
	3	2	1	1	1	2			3	2
	3	3			3	2				
2^+	0	2	2	0	0	2	2	0	0	2
	2	2	2	1	2	1			2	2
	2	3			2	2				
2^-	1	2	1	1	1	1			1	2
	1	3	3	1	1	2			3	2
	3	2			3	1				
	3	3			3	2				
3^+	0	3	2	1	2	1			2	2
	2	2			2	2				
	2	3								
3^-	1	2	3	0	1	2	3	0	1	2
	1	3	3	1	3	1			3	2
	3	2			3	2				
	3	3								
4^+	2	2			2	2	4	0	2	2
	2	3								
4^-	1	3	3	1	3	1			3	2
	3	2			3	2				
	3	3								
5^+	2	3								
5^-	3	2			3	2	5	0	3	2
6^-	3	3								

and thus is allowed only for states with natural parity ($\Pi = (-1)^J$). It is clear that the number of possible formation channels is greatest and thus the possible mixing combinations are largest for the J = 2 and J = 3 p-wave resonances. The p_1 channel should be strong only for lower spin states, while the p_2 channel may be strong for somewhat higher spins. The existence of α_0 decay severely limits the possible spin assignments for a resonance. The angular distribution of the α_0 decay is useful in determining the entrance mixing ratios since exit mixing is not possible.

The entrance and exit mixing ratios are defined similarly to the inelastic mixing ratios for $^{29}Si(p,p)$,

$$\xi_n = \sum_{\ell} \Gamma_{p_n, s_>, \ell} \; / \; \Gamma_{p_n}$$

where $s_>$ is the higher channel spin and Γ_{p_n} is the total width in the n^{th} decay channel. The ℓ mixing ratios are defined as

$$\varepsilon_{ns} = \pm\sqrt{\Gamma_{p_n, s, \ell+2} \; / \; \Gamma_{p_n, s, \ell}}.$$

The corresponding mixing angles are

$$\tan(\Psi_{ns}) = \varepsilon_{ns}.$$

The subscript n is omitted for the elastic scattering mixing ratios. Channel spin mixing does not occur for alpha decay due to the zero spin of the alpha particle. The zero channel spin for the (p,α_0) reaction also forbids ℓ mixing. For alpha decay (except to the ground state) the ℓ-mixing ratio is

$$\varepsilon_{cm} = \pm\sqrt{\Gamma_{a_n, \ell+2} / \Gamma_{a_n, \ell}}.$$

The ^{27}Al proton elastic scattering resonance shapes for each channel spin and for ℓ values up to three are shown in figure 4.5. As for the ^{29}Si excitation functions (figure 4.2), the qualitative features of the resonance shapes depend on the ℓ value and not on the channel spin or total angular momentum. For the relatively low angular momenta (J = 2 or 3) in this figure, the resonance shapes for the different channel spins are similar. For lower values of J the shapes are almost identical, but for higher J values the differences between channel spins are more pronounced. Examples of resonance shapes for other angular momenta and for channel spin mixing and ℓ-mixing follow.

To reduce the amount of trial and error fitting and to aid in determining all possible fits for a resonance, catalogs of the resonance shapes were generated. These catalogs included three dimensional (3D) perspective plots of pure channel spin mixing and of pure ℓ-mixing for elastic scattering, along with two dimensional (2D) overlays of the 3D plots for direct comparison. Examples of the channel spin mixing plots from this catalog are shown in figures 4.6, 4.7, 4.8, and 4.9.

In figure 4.6 are shown the excitation functions at two angles for channel spin mixing for a $J^{\pi} = 2^{-}$ p-wave resonance at E_p = 2.5 MeV. The upper plots are 3D perspective plots with the channel spin mixing axis projected out of the page. The excitation functions were generated in 5% increments of the channel spin mixing ratio with $\xi = 0$ located at the coordinate origin. Identifying symbols were placed at the same energy on each curve. The lower plots are the 2D overlays of the upper plots. There is a one to one correspondence of the identifying symbols between the 2D and 3D plots but the symbols on the 2D plots were placed at higher energy points

Figure 4.5. Theoretically calculated excitation functions for proton elastic scattering from ^{27}Al at four angles. Resonance shapes are shown for ℓ = 0, 1, 2, and 3 resonances for each channel spin with J = 2, except for the ℓ = 0, s = 3, resonance where J = 3. The resonance strengths $(2J+1)\Gamma_p$ = 1 keV. Cross sections for each angle are all on the same scale. Note the supressed zeroes on the cross section axes. The energy axis tick marks are at 5 keV intervals.

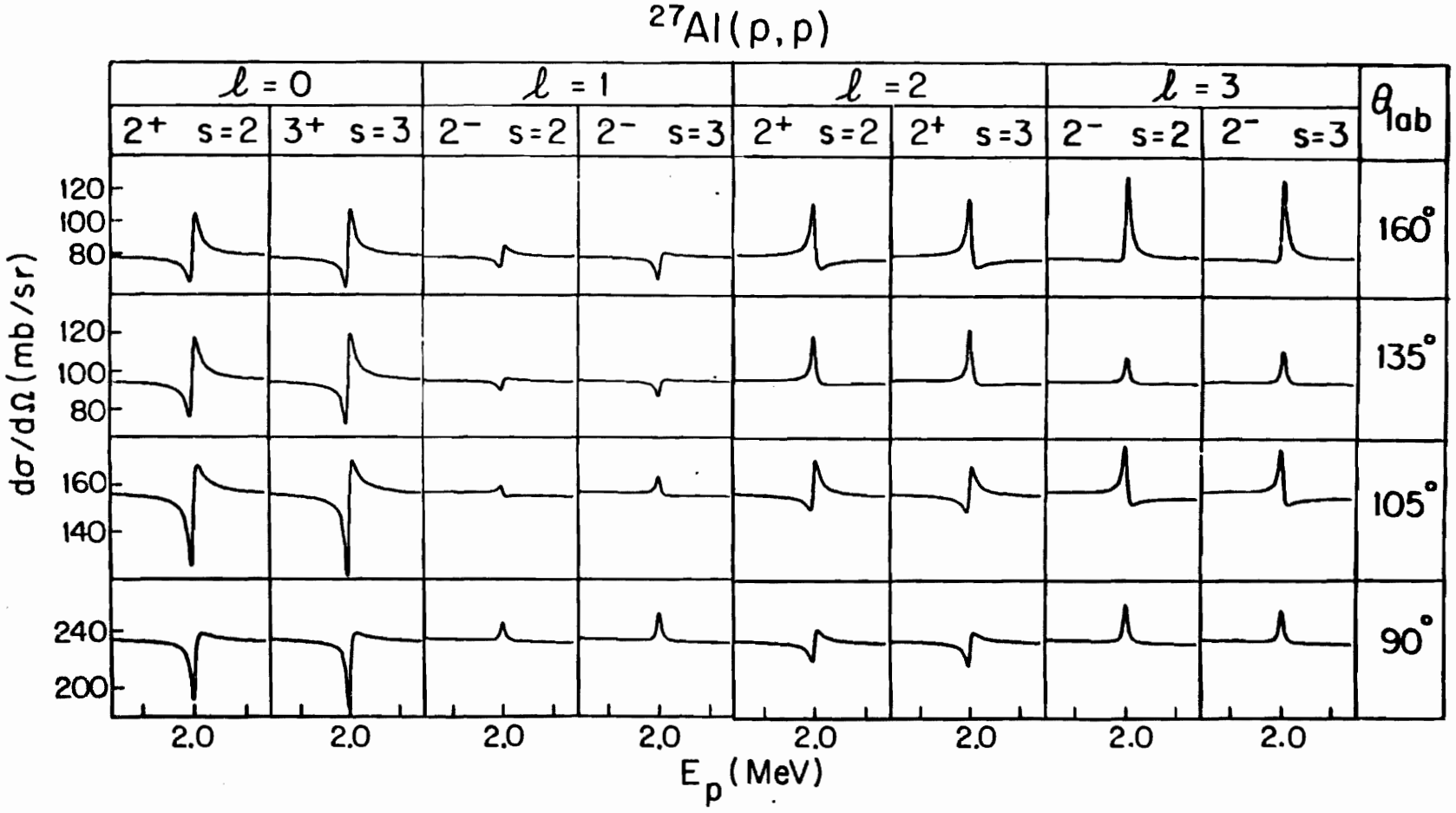
^{27}Al(p,p)
ℓ = 0
ℓ = 1
ℓ = 2
ℓ = 3
θlab
2+ s=2
3+ s=3
2− s=2
2− s=3
2+ s=2
2+ s=3
2− s=2
2− s=3
160°
135°
105°
90°
dσ/dΩ (mb/sr)
120
100
80
160
140
240
200
2.0
Ep (MeV)

Figure 4.6. Three dimensional perspective plots (upper figures) with the corresponding two dimensional overlays (lower figures) show the variation of the resonance shape with the channel spin admixture for a $J^{\pi} = 2^{-}$ p-wave resonance at 90^{o} and 160^{o}.

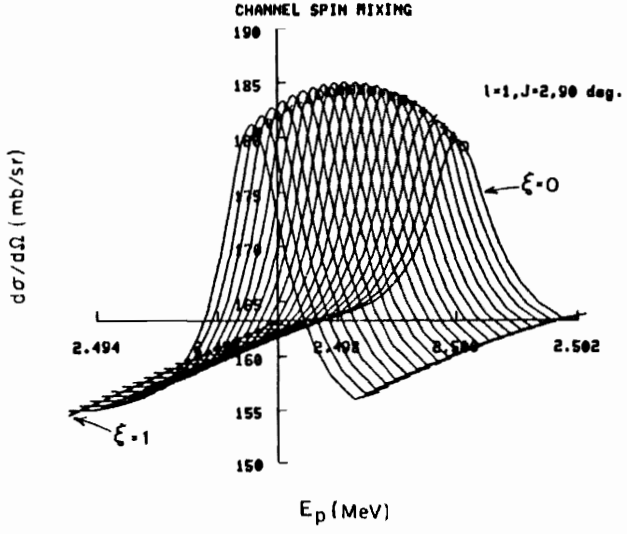
CHANNEL SPIN MIXING
l=1,J=2,90 deg.
ξ=0
ξ=1
dσ/dΩ (mb/sr)
E_p (MeV)

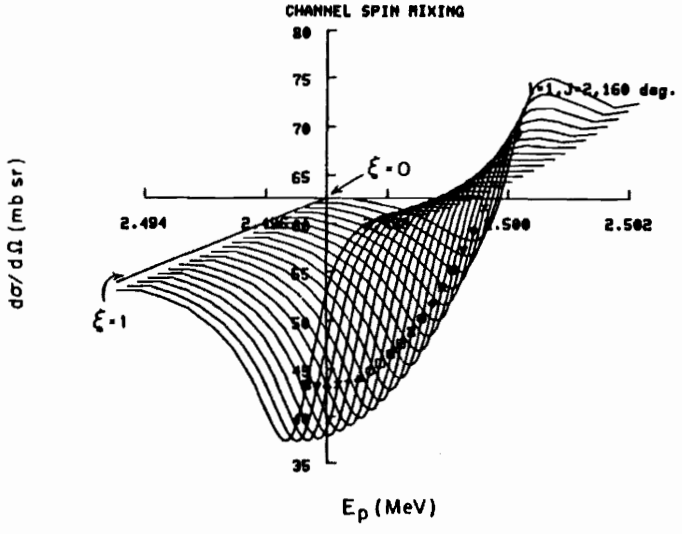
CHANNEL SPIN MIXING
l=1,J=2,160 deg.
ξ=0
ξ=1
dσ/dΩ (mb sr)
E_p (MeV)

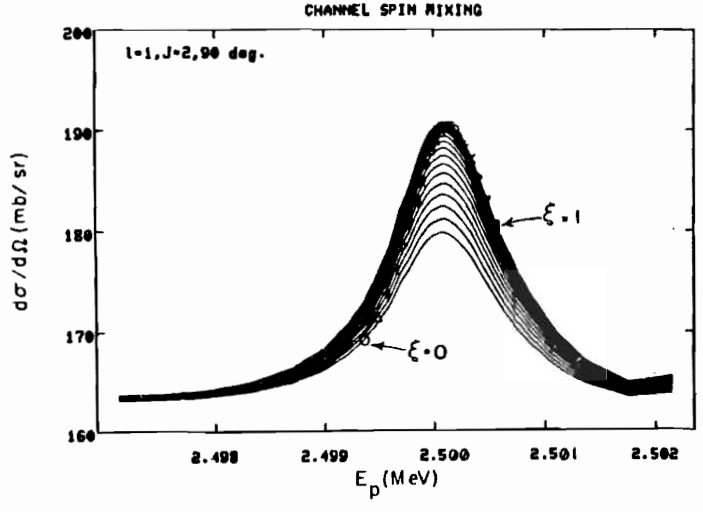
CHANNEL SPIN MIXING
l=1,J=2,90 deg.
ξ=1
ξ=0
dσ/dΩ (mb/sr)
E_p (MeV)

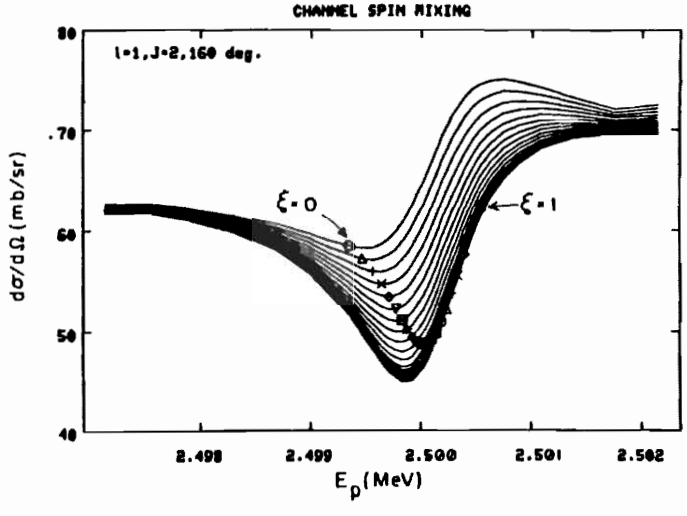
CHANNEL SPIN MIXING
l=1,J=2,160 deg.
ξ=0
ξ=1
dσ/dΩ (mb/sr)
E_p (MeV)

Figure 4.7 Three dimensional perspective plots (upper figures) with the corresponding two dimensional overlays (lower figures) show the variation of the resonance shape with the channel spin admixture for a $J^{\pi} = 3^{-}$ p-wave resonance at 90^{o} and 160^{o}.

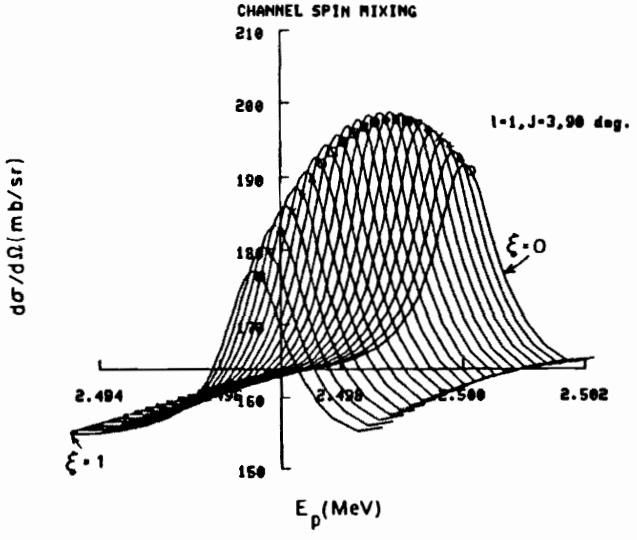
CHANNEL SPIN MIXING
l=1,J=3,90 deg.
ξ=0
ξ=1
dσ/dΩ(mb/sr)
E_p(MeV)

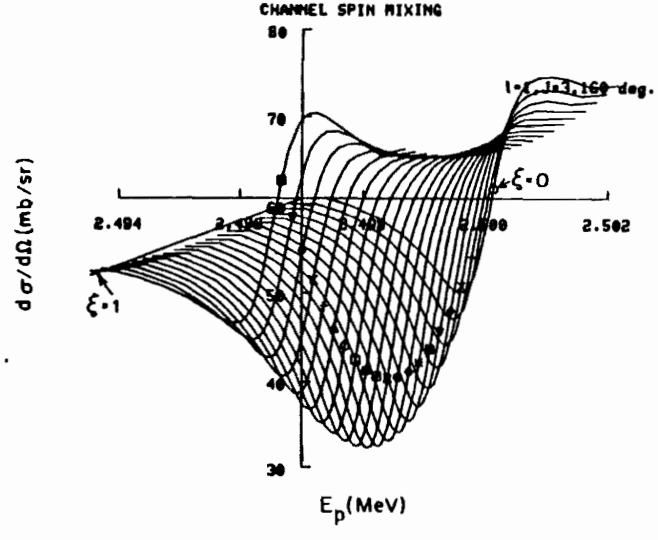
CHANNEL SPIN MIXING
ξ=0
ξ=1
dσ/dΩ(mb/sr)
E_p(MeV)

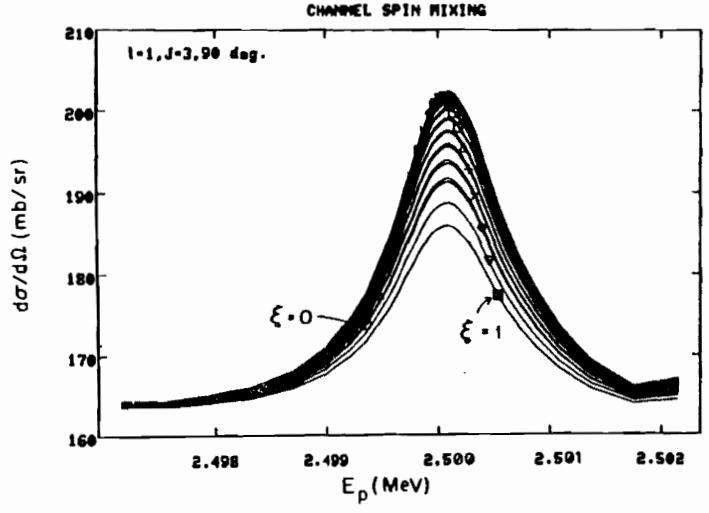
CHANNEL SPIN MIXING
l=1,J=3,90 deg.
ξ=0
ξ=1
dσ/dΩ(mb/sr)
E_p(MeV)

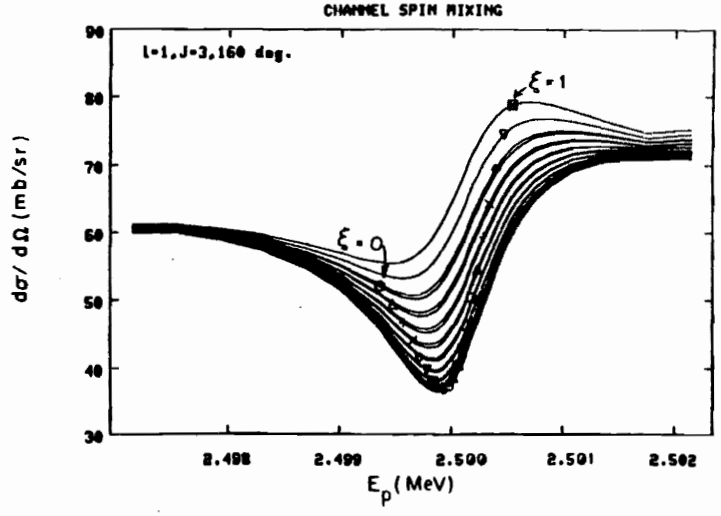
CHANNEL SPIN MIXING
l=1,J=3,160 deg.
ξ=1
ξ=0
dσ/dΩ(mb/sr)
E_p(MeV)

Figure 4.8 Three dimensional perspective plots (upper figures) with the corresponding two dimensional overlays (lower figures) show the variation of the resonance shape with the channel spin admixture for a $J^{\pi} = 4^{+}$ d-wave resonance at 90^{o} and 135^{o}.

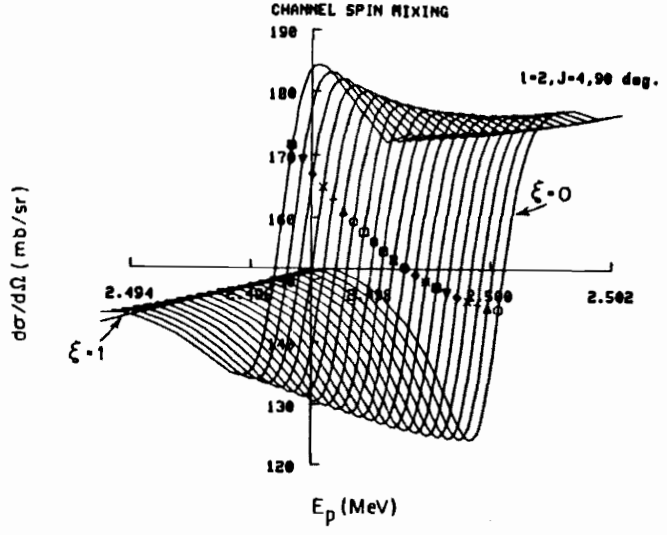
CHANNEL SPIN MIXING
l=2,J=4,90 deg.
ξ=0
ξ=1
dσ/dΩ (mb/sr)
E_p (MeV)

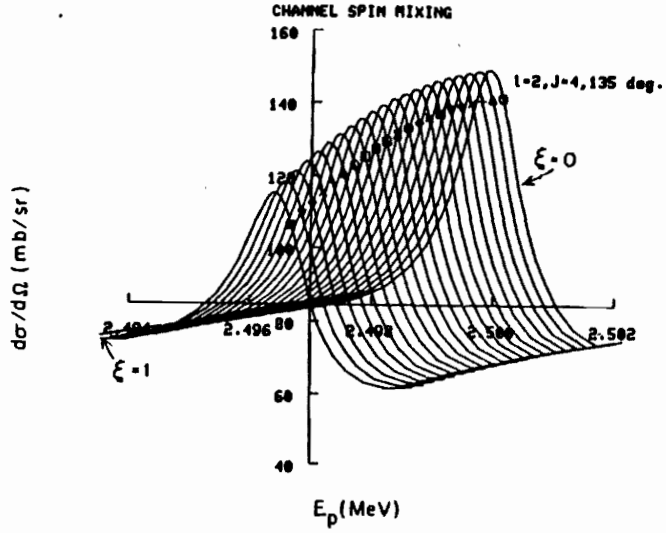
CHANNEL SPIN MIXING
l=2,J=4,135 deg.
ξ=0
ξ=1
dσ/dΩ (mb/sr)
E_p (MeV)

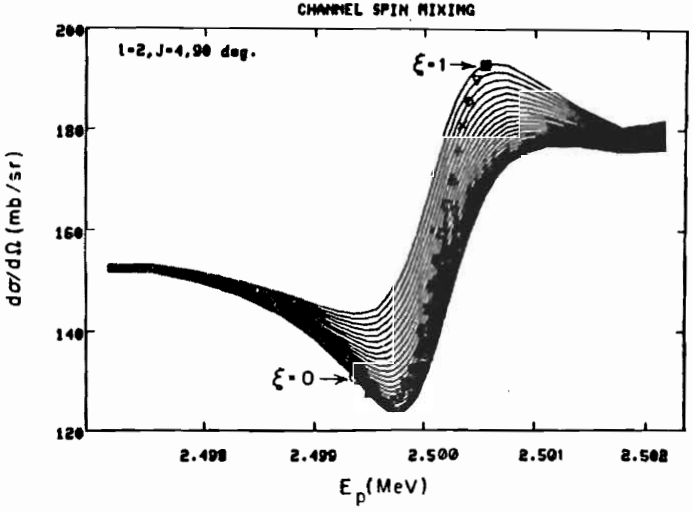
CHANNEL SPIN MIXING
l=2,J=4,90 deg.
ξ=1
ξ=0
dσ/dΩ (mb/sr)
E_p (MeV)

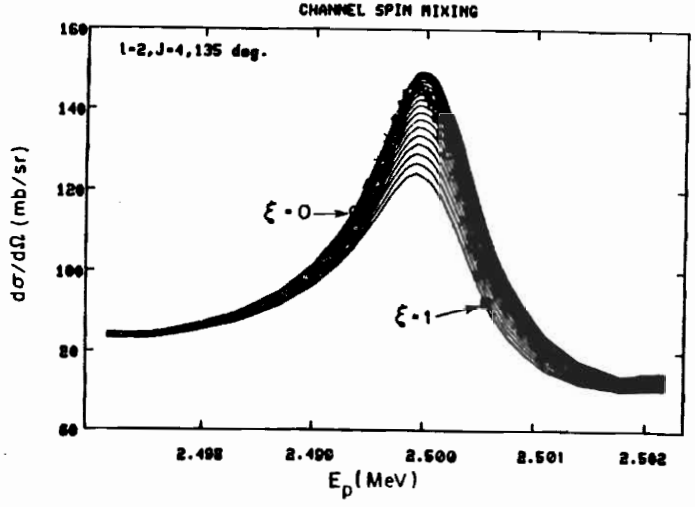
CHANNEL SPIN MIXING
l=2,J=4,135 deg.
ξ=0
ξ=1
dσ/dΩ (mb/sr)
E_p (MeV)

Figure 4.9 Three dimensional perspective plots (upper figures) with the corresponding two dimensional overlays (lower figures) show the variation of the resonance shape with the channel spin admixture for a $J^{\pi} = 4^{-}$ f-wave resonance at 90^{o} and 135^{o}.

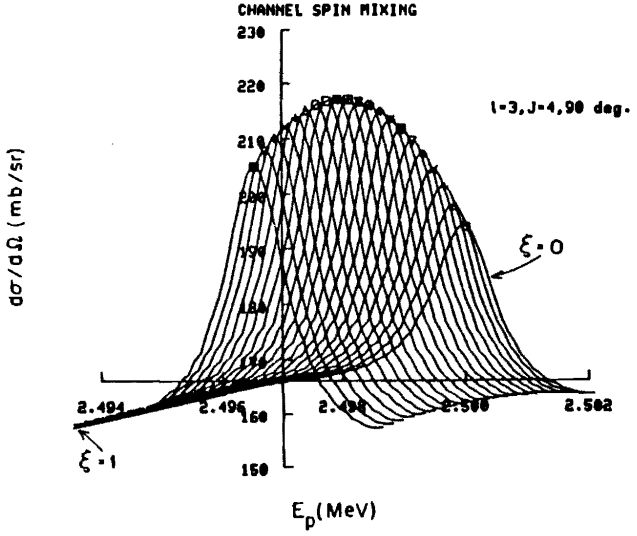
CHANNEL SPIN MIXING
l=3,J=4,90 deg.
ξ=0
ξ=1
dσ/dΩ (mb/sr)
E_p(MeV)

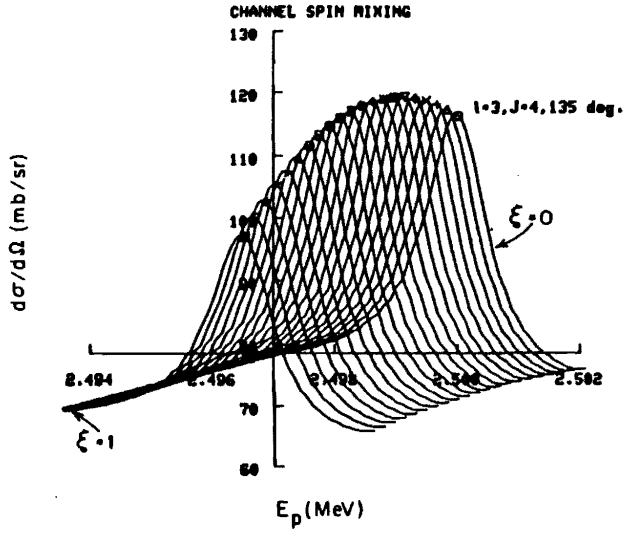
CHANNEL SPIN MIXING
l=3,J=4,135 deg.
ξ=0
ξ=1
dσ/dΩ (mb/sr)
E_p(MeV)

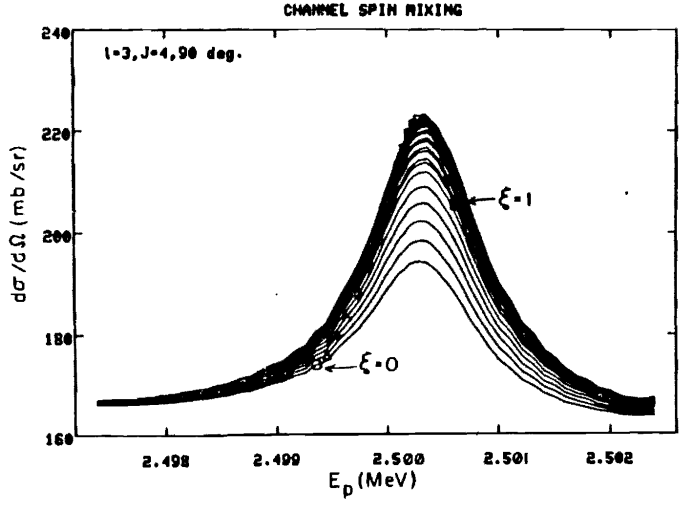
CHANNEL SPIN MIXING
l=3,J=4,90 deg.
ξ=1
ξ=0
dσ/dΩ (mb/sr)
E_p(MeV)

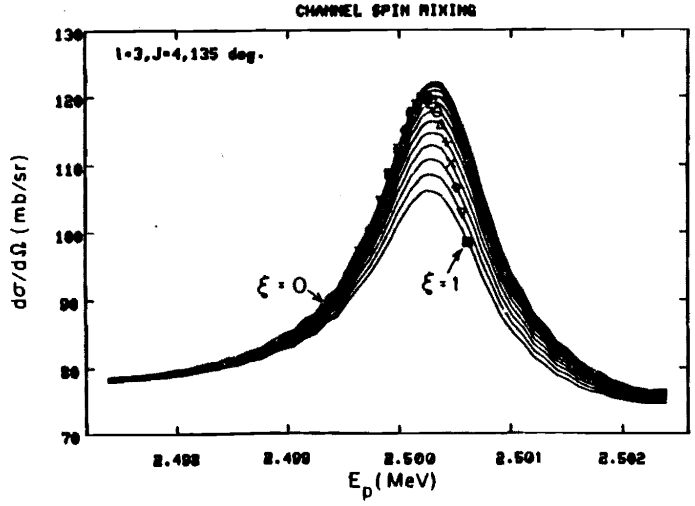
CHANNEL SPIN MIXING
l=3,J=4,135 deg.
ξ=0
ξ=1
dσ/dΩ (mb/sr)
E_p(MeV)

with increasing values of ξ. Seven of the identifying symbols were used twice but this should not result in any confusion.

For the $J^{\pi} = 2^{-}$ resonance in figure 4.6 it can be seen that the resonance shapes are different for over half of the range of the channel spin mixing values. Only for the higher values of ξ is there overlap of the shapes at all angles, giving a range of possible values for ξ. The shapes for the $J^{\pi} = 3^{-}$ p-wave resonance in figure 4.7 overlap at all angles for most of the range of ξ, thus two channel spin mixing ratios are possible in fitting an isolated $J^{\pi} = 3^{-}$ resonance, except for values of ξ near 1. Channel spin mixing is not allowed for p-wave resonances of spins 1 and 4.

Channel spin mixing plots for a $J^{\pi} = 4^{+}$ d-wave resonance are shown in figure 4.8. For d-wave resonances the channel spin mixing ratios are unique, as is demonstrated in this figure. Unfortunately the magnitude of the differences in the cross sections are not as great for the lower spin d-wave resonances. This means that there will be more uncertainty in determining ξ for the lower spin d-wave resonances. Channel spin mixing occurs for J values from 1 to 4 but not for J = 0 and 5 for d-wave resonances.

Figure 4.9 shows the channel spin mixed shapes for a $J^{\pi} = 4^{-}$ f-wave resonance. At 90° the resonance shapes tend to overlap for higher values of ξ while at 135° the overlap occurs at lower values of ξ. Since this is generally the case for f-wave resonances, a unique value of the channel spin mixing may be found provided the resonance is sufficiently large that the finite resolution does not dominate the shape. Again, as for the d-wave resonances, the differences in shape are less for lower spins. Channel spin mixing occurs for f-wave resonances with J = 1 to 5.

It is expected from statistical considerations that on the average the ℓ-mixing ratio should equal the ratio of the penetrabilities of the two

competing orbital angular momenta. The penetrabilities for the decay modes observed in proton scattering from ^{27}Al are plotted in figures 4.10, 4.11, and 4.12. The average ℓ-mixing ratio should be small over most of the energy range studied. Due to the very low $\ell = 4$ penetrability no g-wave resonances or admixtures were expected in this data, and none were observed. Thus ℓ-mixing was only considered for resonances with $J^\pi = 2^+$, 3^+, 1^-, 2^-, 3^-, and 4^-.

Because mixing of ℓ values of different channel spins is an incoherent process the effects of this type of mixing are easily predicted from the resonance shapes for the pure ℓ values. Mixing of ℓ values possessing the same channel spin exhibits coherent interference. Since these effects can not easily be inferred from the resonance shapes for the pure ℓ values, a catalog of elastic scattering shapes was generated for coherent ℓ-mixing similar to the channel spin mixing catalogs.

Figure 4.13 shows the coherent ℓ-mixing for a $J^\pi = 2^+$ resonance at two angles for $E_p = 2.5$ MeV. In the 3D plots the axis of the ℓ-mixing angle is projected out of the page with $\phi = -90^\circ$ located at the coordinate origin. The excitation functions were calculated for a constant total width, while the partial widths were varied in 10% increments of the total width. The pure s-wave shape occurs at the midpoint of the mixing angle axis ($\phi = 0$) and the shapes for $\phi = +90^\circ$ and $\phi = -90^\circ$ are, of course, identical.

From figure 4.13 it is clear that the relative sign of the partial waves can not be obtained for an isolated $J^\pi = 2^+$ resonance. Thus there are two (approximately equal) solutions with opposite signs for the mixing angle. In addition, the $s = 3$, $\ell = 2$ partial wave results in nearly the same resonance shapes when mixed with $\ell = 0$, so the d-wave channel spin admixture also is undetermined. Still, the resonance energy, angular momentum, width, and a range of possible values for the ℓ-mixing are

Figure 4.10 Coulomb penetrabilities versus energy for the $^{27}Al(p,p)$ and (p,p_1) reactions. The top horizontal axes list the exit energies at which the penetrabilities were calculated. The bottom horizontal axes give the corresponding incident proton energies.

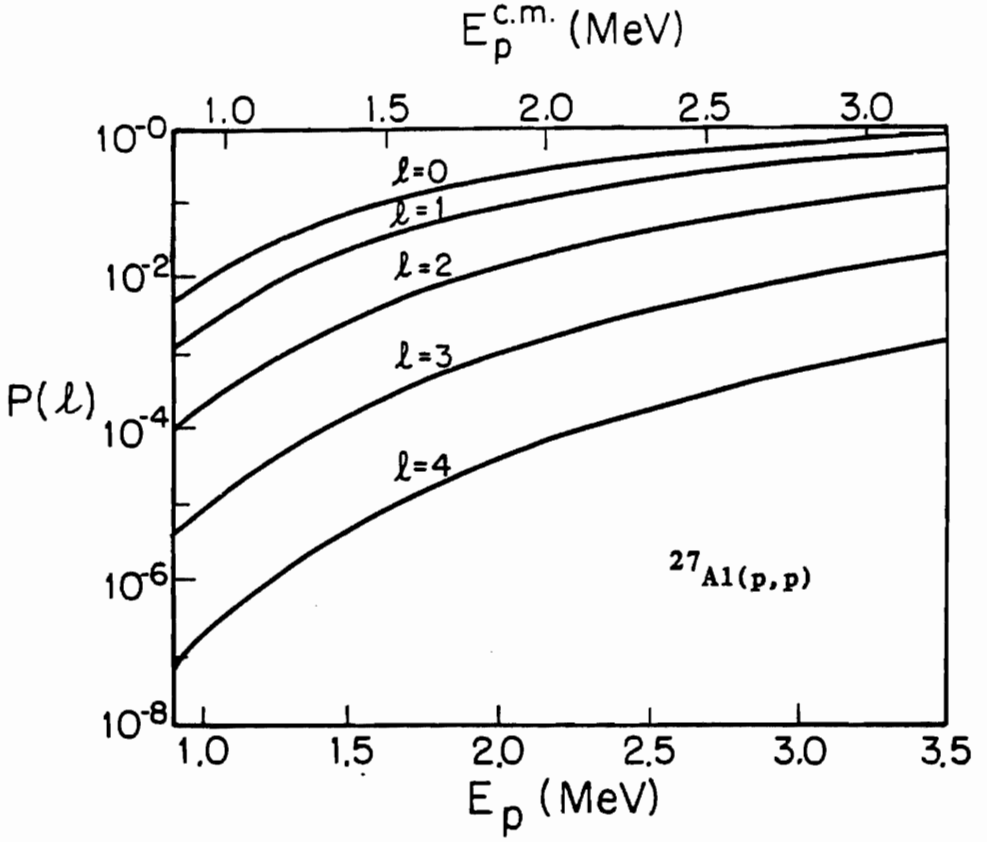
$E_p^{c.m.}$ (MeV)
1.0
1.5
2.0
2.5
3.0
10^{-0}
10^{-2}
10^{-4}
10^{-6}
10^{-8}
P(ℓ)
ℓ=0
ℓ=1
ℓ=2
ℓ=3
ℓ=4
^{27}Al(p,p)
1.0
1.5
2.0
2.5
3.0
3.5
E_p (MeV)

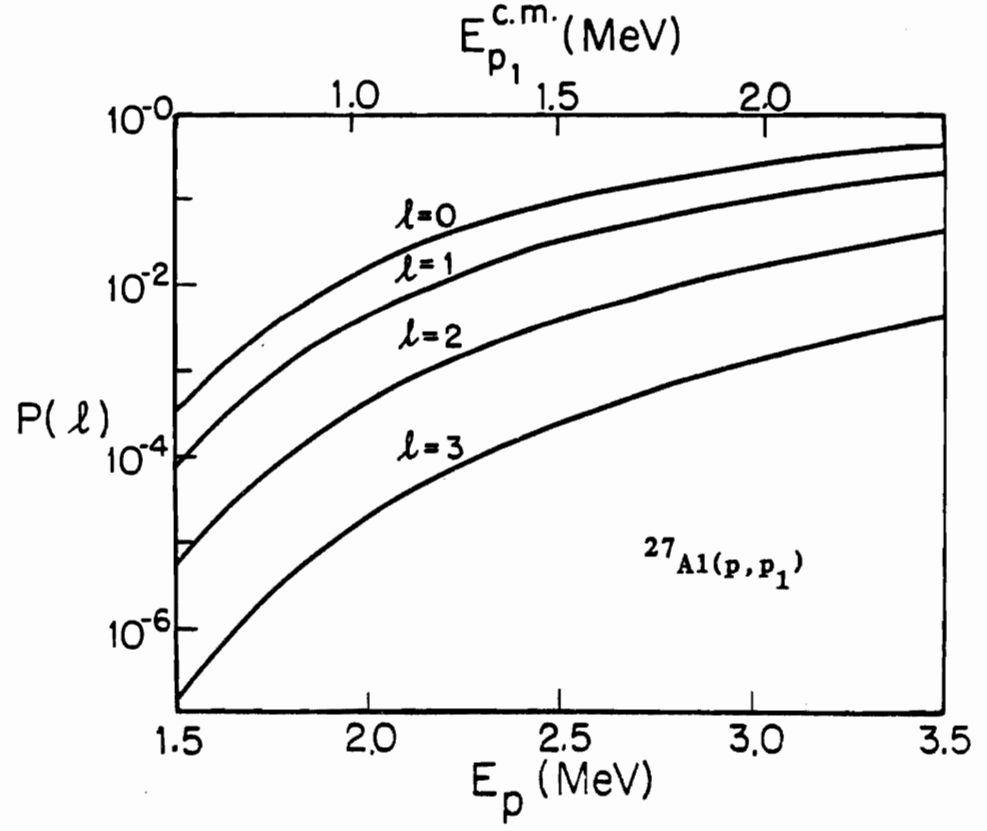
$E_{p_1}^{c.m.}$ (MeV)
1.0
1.5
2.0
10^{-0}
10^{-2}
10^{-4}
10^{-6}
P(ℓ)
ℓ=0
ℓ=1
ℓ=2
ℓ=3
^{27}Al(p,p_1)
1.5
2.0
2.5
3.0
3.5
E_p (MeV)

Figure 4.11 Coulomb penetrabilities versus energy for the $^{27}Al(p,p_2)$ and (p,p_3) reactions. The top horizontal axes list the exit energies at which the penetrabilities were calculated. The bottom horizontal axes give the corresponding incident proton energies.

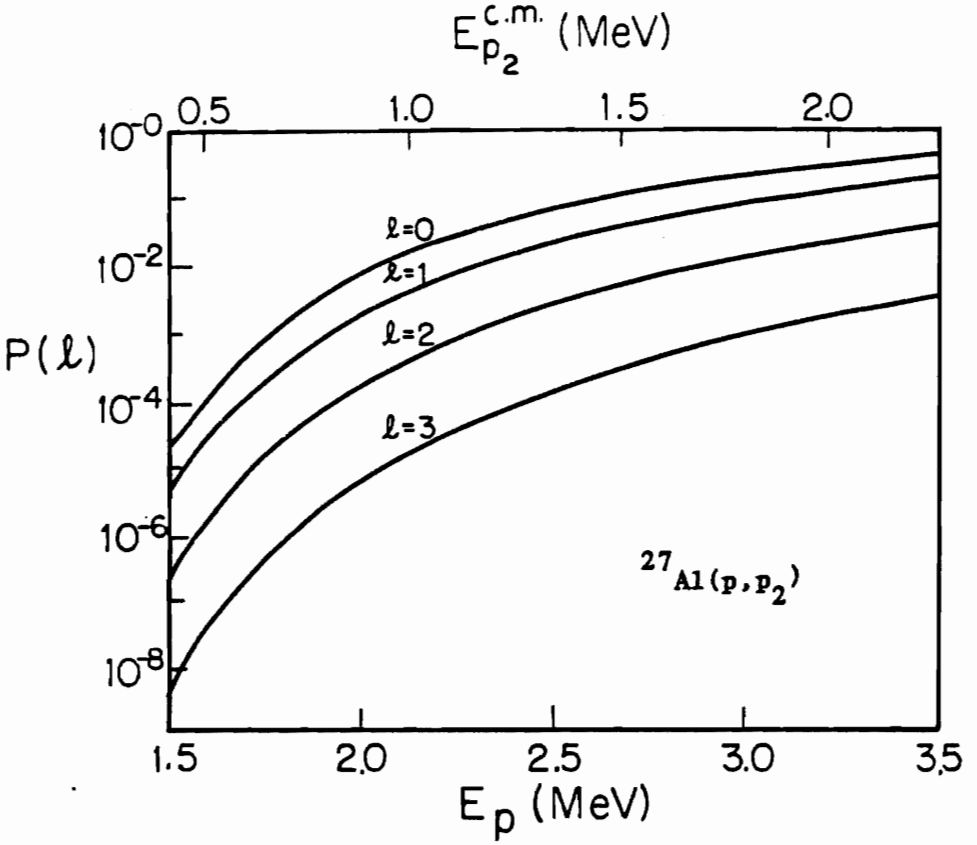
$E_{p_2}^{c.m.}$ (MeV)
0.5
1.0
1.5
2.0
10^{-0}
10^{-2}
10^{-4}
10^{-6}
10^{-8}
P(ℓ)
ℓ=0
ℓ=1
ℓ=2
ℓ=3
^{27}Al(p,p$_2$)
1.5
2.0
2.5
3.0
3.5
E_p (MeV)

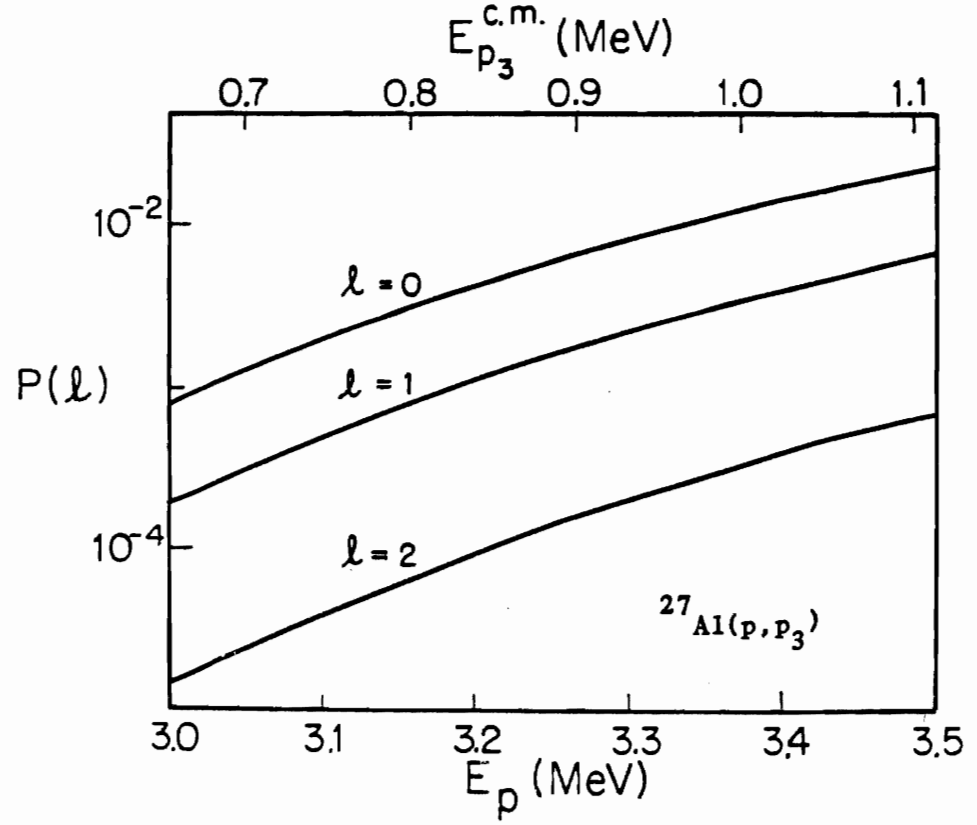
$E_{p_3}^{c.m.}$ (MeV)
0.7
0.8
0.9
1.0
1.1
10^{-2}
10^{-4}
P(ℓ)
ℓ = 0
ℓ = 1
ℓ = 2
^{27}Al(p,p$_3$)
3.0
3.1
3.2
3.3
3.4
3.5
E_p (MeV)

Figure 4.12 Coulomb penetrabilities versus energy for the $^{27}Al(p,\alpha_0)$ and (p,α_1) reactions. The top horizontal axes list the exit energies at which the penetrabilities were calculated. The bottom horizontal axes give the corresponding incident proton energies.

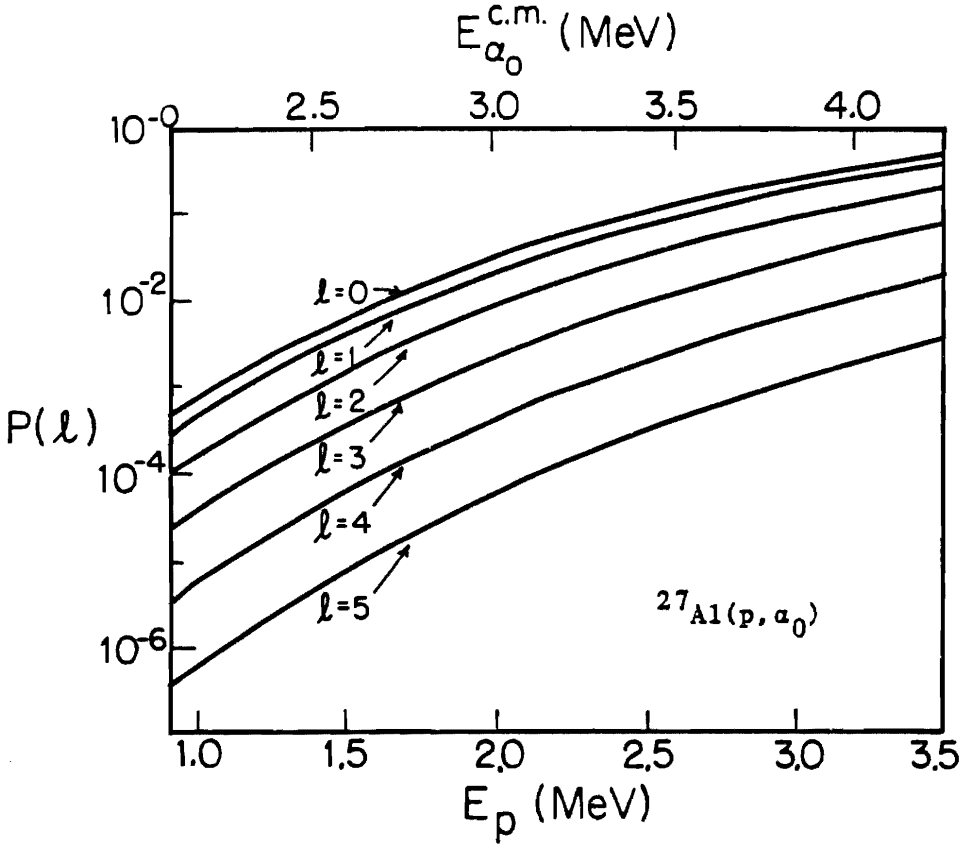
$E_{\alpha_0}^{c.m.}$ (MeV)
2.5
3.0
3.5
4.0
10^{-0}
10^{-2}
10^{-4}
10^{-6}
P(ℓ)
ℓ=0
ℓ=1
ℓ=2
ℓ=3
ℓ=4
ℓ=5
^{27}Al(p, α_0)
1.0
1.5
2.0
2.5
3.0
3.5
E_p (MeV)

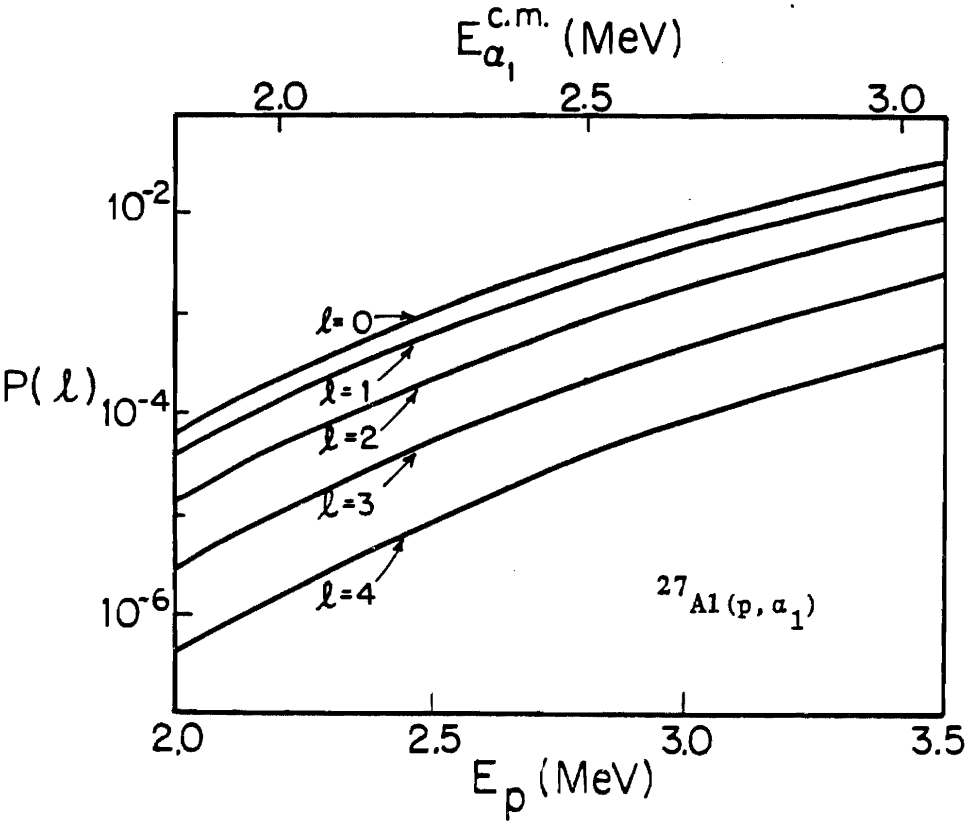
$E_{\alpha_1}^{c.m.}$ (MeV)
2.0
2.5
3.0
10^{-2}
10^{-4}
10^{-6}
P(ℓ)
ℓ= 0
ℓ=1
ℓ=2
ℓ=3
ℓ=4
^{27}Al(p, α_1)
2.0
2.5
3.0
3.5
E_p (MeV)

Figure 4.13 Three dimensional perspective plots (upper figures) with the corresponding two dimensional overlays (lower figures) show the variation of the resonance shape with the coherent orbital angular momentum admixture for s=2 for a $J^{\pi} = 2^{+}$ resonance at 90^{o} and 160^{o}.

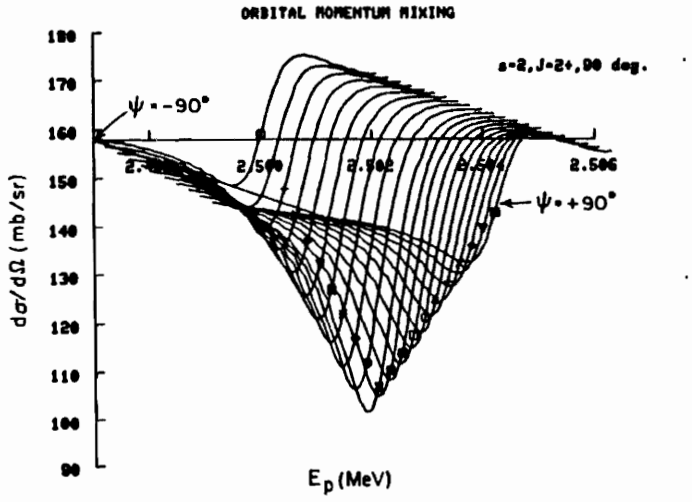
ORBITAL MOMENTUM MIXING
s=2,J=2+,90 deg.
ψ=-90°
ψ=+90°
dσ/dΩ (mb/sr)
E_p(MeV)

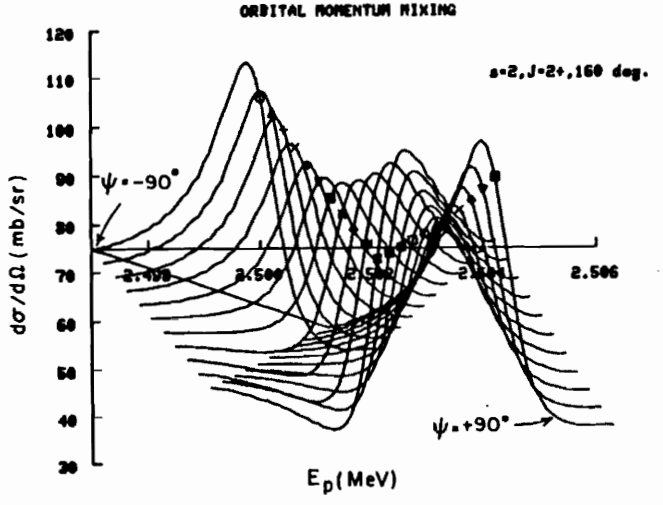
ORBITAL MOMENTUM MIXING
s=2,J=2+,160 deg.
ψ=-90°
ψ=+90°
dσ/dΩ (mb/sr)
E_p(MeV)

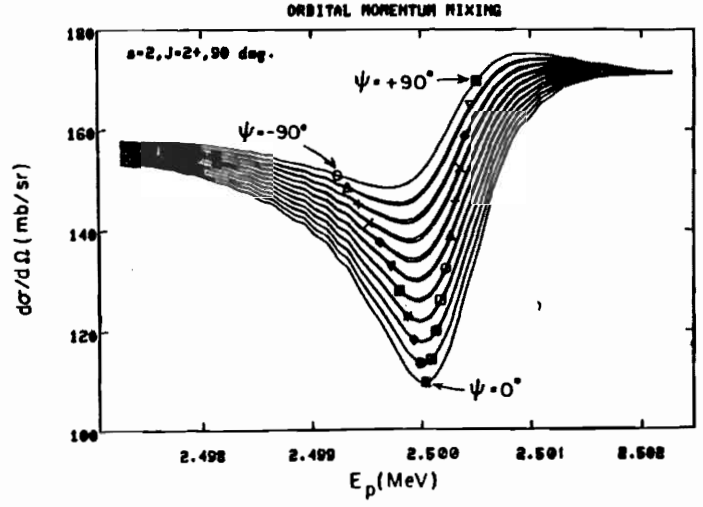
ORBITAL MOMENTUM MIXING
s=2,J=2+,90 deg.
ψ=+90°
ψ=-90°
ψ=0°
dσ/dΩ (mb/sr)
E_p(MeV)

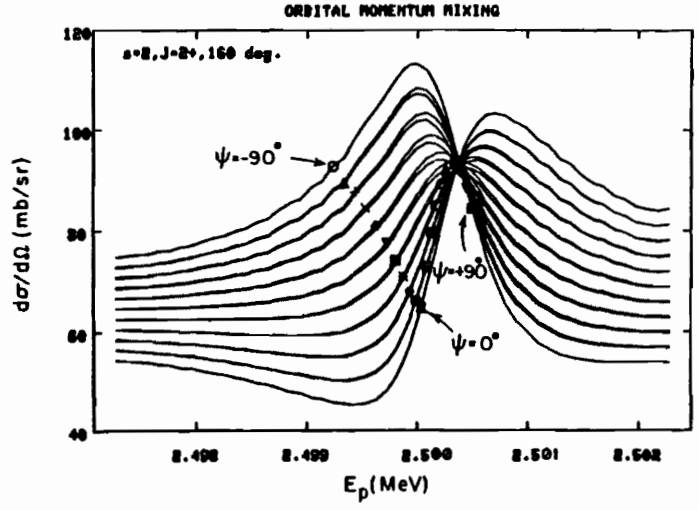
ORBITAL MOMENTUM MIXING
s=2,J=2+,160 deg.
ψ=-90°
ψ=+90°
ψ=0°
dσ/dΩ (mb/sr)
E_p(MeV)

determined from the elastic scattering data alone. The case of ℓ mixing for $J^\pi = 3^+$ is similar to that for $J^\pi = 2^+$.

The coherent ℓ-mixing for a $J^\pi = 3^-$ resonance with s = 2 is shown in figure 4.14. The conventions are the same as in figure 4.13. Here the coherence effects are most striking. Just from the 135^o excitation function both the magnitude and sign of the mixing angle may be determined. The ℓ-mixing effects are similar for the other spins. Unfortunately both ℓ-mixing and channel spin mixing can occur for resonances with $J^\pi = 2^-$ or 3^-. For these complicated cases more than one solution is possible, but since ℓ-mixing is usually small, multiple solutions seldom occur in practice.

An example of the determination of the channel spin admixture for a J=3, p-wave resonance is shown in figure 4.15. The two channel spin mixing ratios, $\xi = 0.0$ and $\xi = 0.9$, give equally good fits to the data. The extremes of cross section which occur for $\xi = 0.5$ and $\xi = 1.0$ (as shown in figure 4.7) are obviously poorer fits to the data. Notice that the data are much more sensitive to small changes in ξ near $\xi = 0.9$ or 0.0 than near $\xi = 0.5$. It is important to include enough of the Rutherford background to fix the data normalization at the correct value so that the data are not distorted to match the fit. For example, the data in figure 4.15 could be normalized to match the $\xi = 1.0$ fit if only a small energy region were considered.

The determination of the total angular momentum of the J = 3, p-wave resonance is demonstrated by the fits shown in figure 4.16. From figure 4.6, the extremes of cross section occur for $\xi = 0.0$ and $\xi = 1.0$ for a J = 2, p-wave resonance. Neither of these fits reproduce the data, nor will any other channel spin admixture for J = 2. For J = 4, only one channel spin is allowed. The J = 4 fit also does not reproduce the data. The width of the

Figure 4.14 Three dimensional perspective plots (upper figures) with the corresponding two dimensional overlays (lower figures) show the variation of the resonance shape with the coherent orbital angular momentum admixture for s=2 for a $J^{\pi} = 3^{-}$ resonance at 90^{o} and 135^{o}.

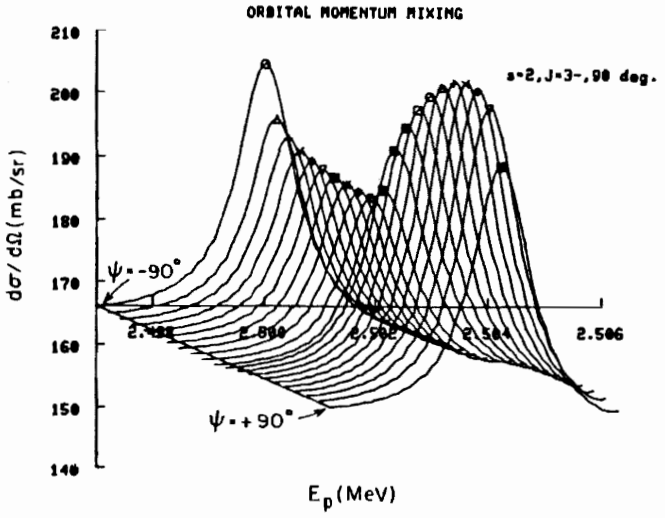
ORBITAL MOMENTUM MIXING
a=2,J=3-,90 deg.
ψ=-90°
ψ=+90°
dσ/dΩ(mb/sr)
E_p(MeV)

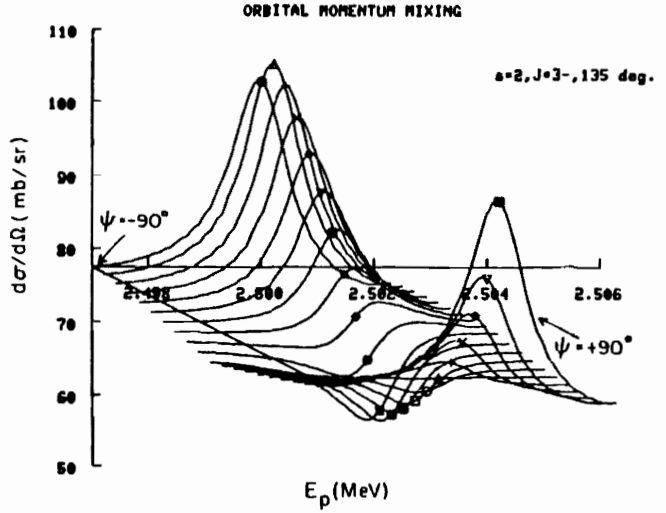
ORBITAL MOMENTUM MIXING
a=2,J=3-,135 deg.
ψ=-90°
ψ=+90°
dσ/dΩ(mb/sr)
E_p(MeV)

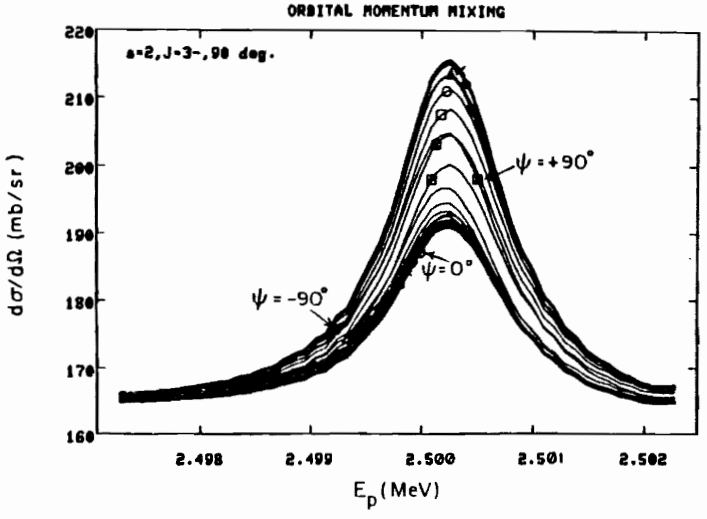
ORBITAL MOMENTUM MIXING
a=2,J=3-,90 deg.
ψ=+90°
ψ=0°
ψ=-90°
dσ/dΩ (mb/sr)
E_p(MeV)

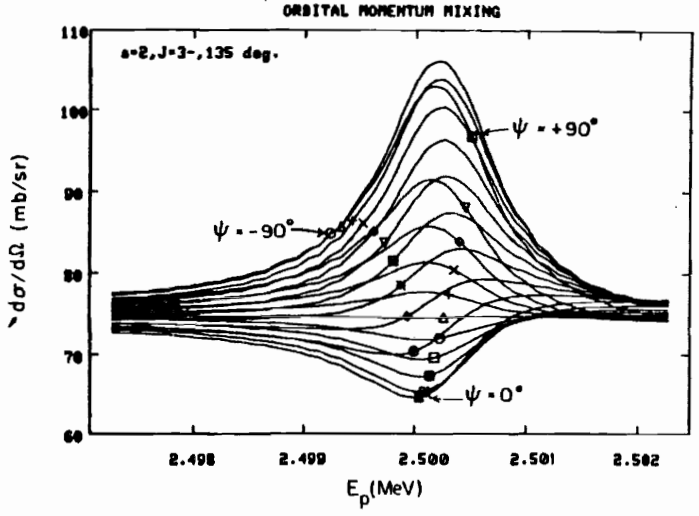
ORBITAL MOMENTUM MIXING
a=2,J=3-,135 deg.
ψ=+90°
ψ=-90°
ψ=0°
dσ/dΩ (mb/sr)
E_p(MeV)

Figure 4.15 The 160°, $^{27}Al(p,p)$ excitation function is shown with fits for four different values of the channel spin mixing ratio ξ for a $J^{\pi} = 3^{-}$ resonance. The fits calculated with $\xi = 0.0$ and $\xi = 0.9$ are both satisfactory. The resonance shapes obtained for $\xi = 0.5$ and $\xi = 1.0$ do not reproduce the data. The lower energy resonance has $J^{\pi} = 2^{+}$.

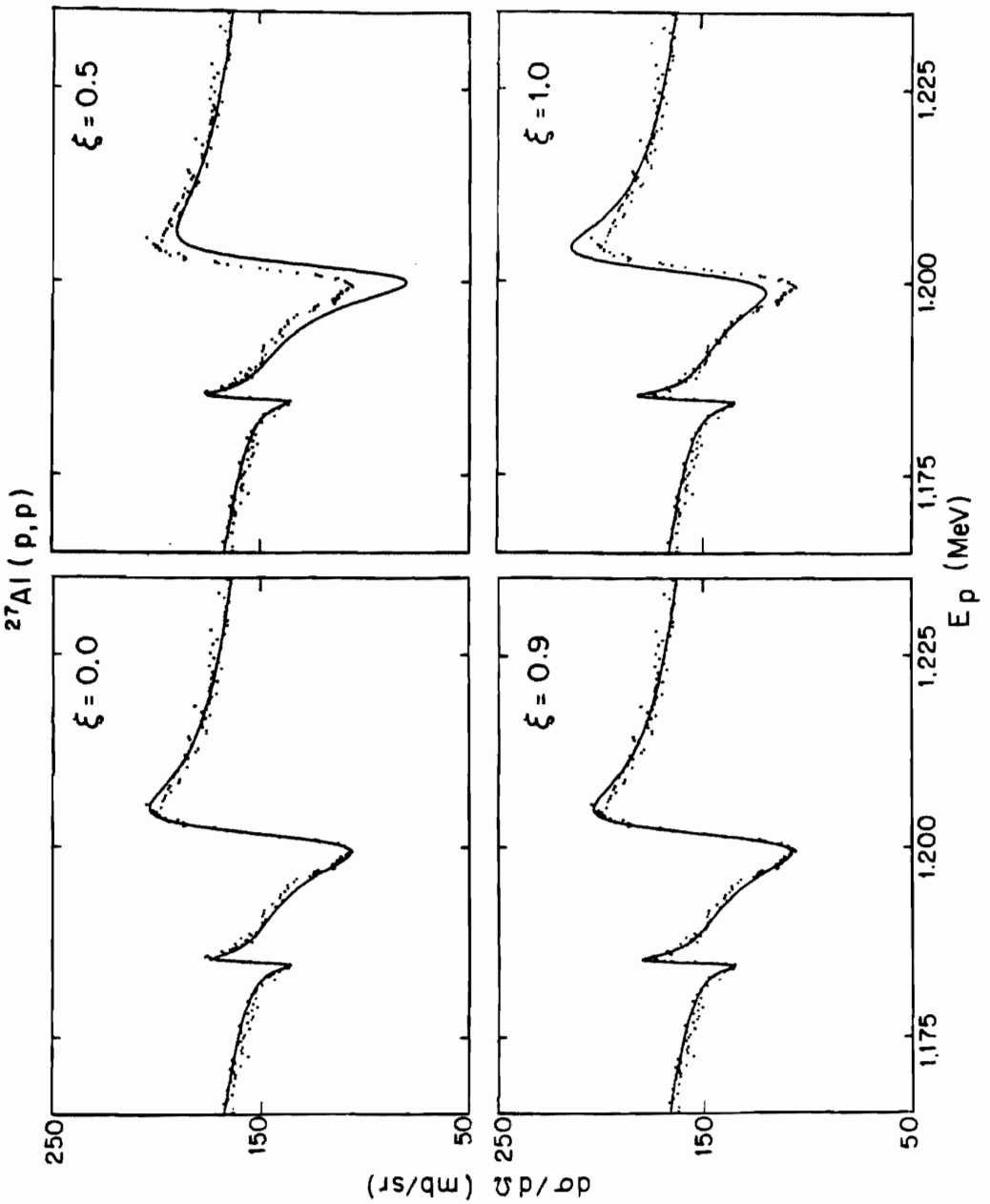
^{27}Al (p,p)
ξ = 0.0
ξ = 0.5
ξ = 0.9
ξ = 1.0
dσ/dΩ (mb/sr)
250
150
50
1.175
1.200
1.225
E p (MeV)

Figure 4.16 The 160° data for an $\ell = 1$ resonance in $^{27}Al(p,p)$ with fits for three different values of J^{π}. The $J^{\pi} = 2^{-}$ fit is shown for two channel spin mixing ratios, $\xi = 0.0$ and $\xi = 1.0$ The fits for $J^{\pi} = 2^{-}$ and $J^{\pi} = 4^{-}$ do not reproduce the data. The $J^{\pi} = 3^{-}$ fit is satisfactory. The lower energy resonance has $J^{\pi} = 2^{+}$.

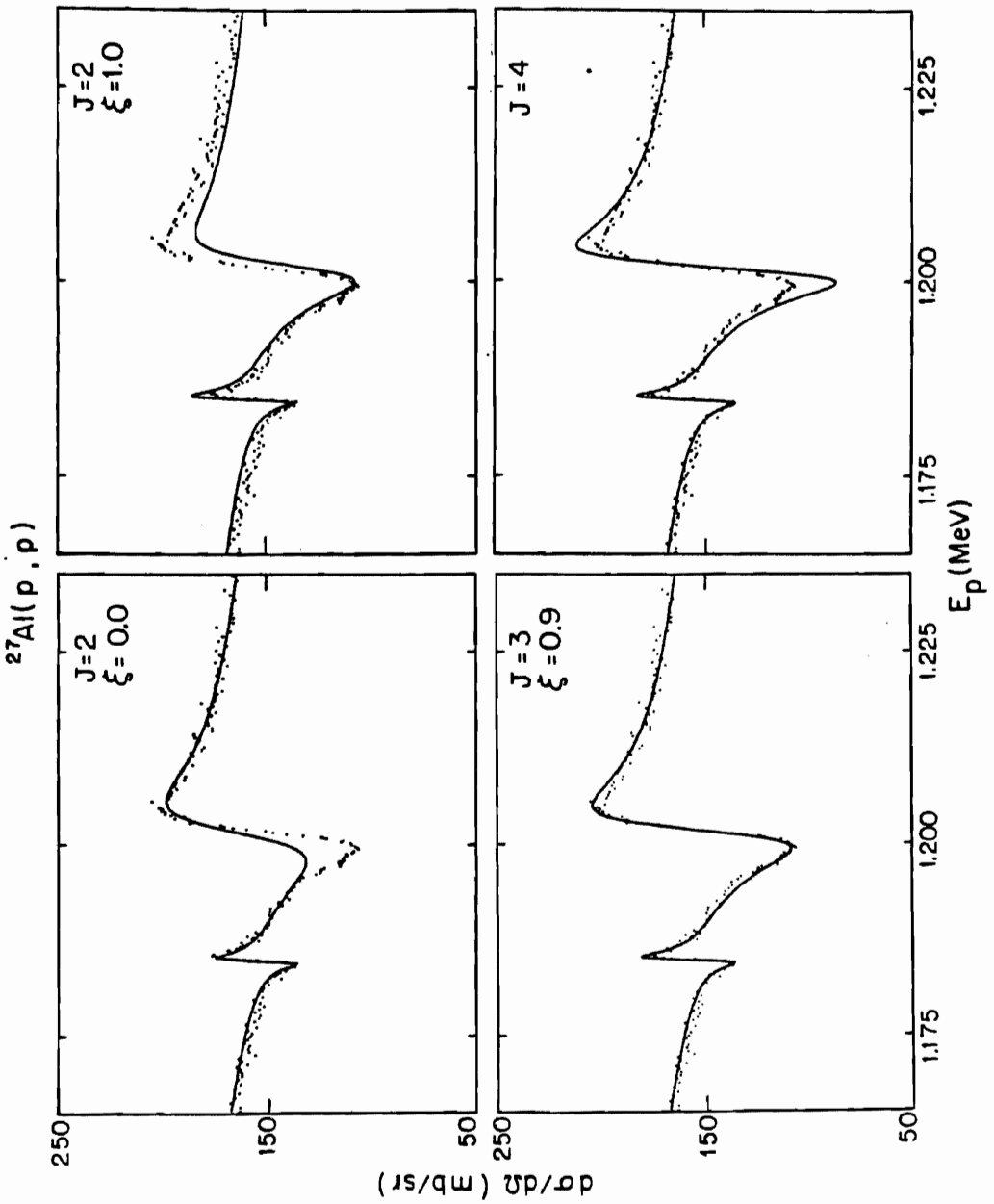
^{27}Al(p,p)
J=2
ξ=0.0
J=2
ξ=1.0
J=3
ξ=0.9
J=4
dσ/dΩ (mb/sr)
250
150
50
1.175
1.200
1.225
E_p(MeV)

J = 2 fits has been increased over the value used for the J = 3 fit in an attempt to fit the maximum and minimum values of the cross section. By comparing the position in energy of the maximum and minimum values of the J = 2 cross section it is clear that further increases in the width will make the fits too broad. Similarly, if the J = 4 resonance width is decreased to match the maximum and minimum values of the cross section the fit will be too narrow.

Rather than rederive explicitly the angular distribution formulas for every possible set of spins, parities, and reaction channels the program MULTI was used to generate the cross sections for pure channel spins and ℓ values for all of the reaction products. The calculated cross sections were then fit to a Legendre polynomial expression of the form

$$W(\theta) \propto 1 + a_2 P_2 + a_4 P_4 + \ldots$$

with the aid of the program LEGFIT. From these results a catalog of the angular distributions was made. The Legendre coefficients are listed in tables 4.3, 4.4, 4.5, and 4.6 for proton induced reactions on ^{27}Al. The sum of the angular distributions for pure ℓ values and channel spins, weighted by the corresponding laboratory widths, allows prediction of the channel spin mixed angular distributions. However, for cases where ℓ-mixing is appreciable the resulting interference terms make quantitative prediction of the angular distributions impossible. These results were a useful aid in selecting possible resonance parameters to fit the elastic and corresponding reaction cross sections. A more thorough analysis of the angular distributions of the reaction products was not usually warranted due to the low statistical accuracy of the data.

C. Data Presentation

1. Proton Scattering from ^{29}Si

TABLE 4.3

LEGENDRE COEFFICIENTS FOR $^{27}Al(p,p_1)$ ANGULAR DISTRIBUTIONS WITH NO CHANNEL SPIN OR ℓ MIXING

J^π	l	s	l′	s′	a_2	a_4	a_6
1−	1	2	1	0	0.20	0.00	0.00
	1	2	1	1	−0.10	0.00	0.00
	3	2	1	0	0.80	0.00	0.00
	3	2	1	1	−0.40	0.00	0.00
	3	3	1	0	−1.00	0.00	0.00
	3	3	1	1	0.50	0.00	0.00
1+	2	2	2	1	−0.50	0.00	0.00
	2	3	2	1	0.15	0.00	0.00
2−	1	2	1	1	−0.70	0.00	0.00
	1	2	3	1	−0.81	0.00	0.00
	1	3	1	1	0.20	0.00	0.00
	1	3	3	1	0.23	0.00	0.00
	3	2	1	1	0.20	0.00	0.00
	3	2	3	1	0.23	−0.43	0.00
	3	3	1	1	−0.37	0.00	0.00
	3	3	3	1	−0.42	0.29	0.00
2+	2	2	2	0	−0.30	0.73	0.00
	2	2	2	1	−0.15	−0.49	0.00
	2	3	2	0	−0.81	−0.19	0.00
	2	3	2	1	−0.41	0.12	0.00
3−	1	2	3	0	0.80	0.00	0.00
	1	2	3	1	0.60	0.00	0.00
	1	3	3	0	−1.00	0.00	0.00
	1	3	3	1	−0.75	0.00	0.00
	3	2	3	0	0.42	−0.82	1.26
	3	2	3	1	0.32	−0.13	−0.95
	3	3	3	0	−0.22	−0.27	−0.50
	3	3	3	1	−0.16	−0.05	0.38
3+	2	2	2	1	0.25	−0.67	0.00
	2	3	2	1	−0.45	0.45	0.00
4−	1	3	3	1	0.65	0.00	0.00
	3	2	3	1	0.65	−0.25	−0.57
	3	3	3	1	0.12	−0.53	0.51

TABLE 4.4

LEGENDRE COEFFICIENTS FOR $^{27}Al(p,p_2)$ ANGULAR DISTRIBUTIONS WITH NO CHANNEL SPIN OR ℓ MIXING

J^π	l	s	l′	s′	a_2	a_4	a_6
1−	1	2	1	1	−0.10	0.00	0.00
	1	2	1	2	0.02	0.00	0.00
	1	2	3	2	0.08	0.00	0.00
	3	2	1	1	−0.40	0.00	0.00
	3	2	1	2	0.08	0.00	0.00
	3	2	3	2	0.31	0.00	0.00
	3	3	1	1	0.50	0.00	0.00
	3	3	1	2	−0.10	0.00	0.00
	3	3	3	2	−0.39	0.00	0.00
1+	2	2	2	1	−0.50	0.00	0.00
	2	2	2	2	0.50	0.00	0.00
	2	3	2	1	0.14	0.00	0.00
	2	3	2	2	−0.14	0.00	0.00
2−	1	2	1	1	−0.70	0.00	0.00
	1	2	3	1	−0.80	0.00	0.00
	1	2	1	2	0.70	0.00	0.00
	1	2	3	2	−0.20	0.00	0.00
	1	3	1	1	0.20	0.00	0.00
	1	3	3	1	0.23	0.00	0.00
	1	3	1	2	−0.20	0.00	0.00
	1	3	3	2	0.06	0.00	0.00
	3	2	1	1	0.20	0.00	0.00
	3	2	3	1	0.23	−0.43	0.00
	3	2	1	2	−0.20	0.00	0.00
	3	2	3	2	0.06	0.64	0.00
	3	3	1	1	−0.37	0.00	0.00
	3	3	3	1	−0.42	0.28	0.00
	3	3	1	2	0.37	0.00	0.00
	3	3	3	2	−0.10	−0.43	0.00
2+	2	2	2	1	−0.15	−0.49	0.00
	2	2	2	2	0.07	0.21	0.00
	2	3	2	1	−0.41	0.12	0.00
	2	3	2	2	0.18	−0.05	0.00

TABLE 4.4-Continued

J^{π}	l	s	l'	s'	a_2	a_4	a_6
3-	1	2	1	2	0.48	0.00	0.00
	1	2	3	2	0.25	0.00	0.00
	1	2	3	1	0.60	0.00	0.00
	1	3	1	2	-0.60	0.00	0.00
	1	3	3	2	-0.32	0.00	0.00
	1	3	3	1	-0.76	0.00	0.00
	3	2	1	2	0.25	0.00	0.00
	3	2	3	2	0.13	0.40	0.53
	3	2	3	1	0.32	-0.14	-0.94
	3	3	1	2	-0.13	0.00	0.00
	3	3	3	2	-0.07	0.14	-0.21
	3	3	3	1	-0.16	-0.05	0.38
3+	2	2	2	1	0.24	-0.67	0.00
	2	2	2	2	0.06	1.01	0.00
	2	3	2	1	-0.45	0.45	0.00
	2	3	2	2	-0.11	-0.67	0.00
4-	1	3	3	1	0.66	0.00	0.00
	1	3	3	2	0.39	0.00	0.00
	3	2	3	1	0.65	-0.25	-0.57
	3	2	3	2	0.39	0.08	1.03
	3	3	3	1	0.12	-0.53	0.52
	3	3	3	2	0.07	0.18	-0.93
4+	2	2	2	2	0.80	0.21	0.00
	2	3	2	2	0.08	-0.42	0.00
5-	3	2	3	2	0.96	0.48	0.10
	3	3	3	2	0.48	-0.32	-0.26

TABLE 4.5

LEGENDRE COEFFICIENTS FOR $^{27}Al(p,\alpha_0)$ ANGULAR DISTRIBUTIONS WITH NO CHANNEL SPIN OR ℓ MIXING

J^π	l	s	l'	s'	a_2	a_4	a_6
1−	1	2	1	0	0.20	0.00	0.00
	3	2	1	0	0.80	0.00	0.00
	3	3	1	0	−0.95	0.00	0.00
2+	2	2	2	0	−0.31	0.73	0.00
	2	3	2	0	−0.82	−0.19	0.00
3−	1	2	3	0	0.80	0.00	0.00
	1	3	3	0	−1.00	0.00	0.00
	3	2	3	0	0.42	−0.82	1.26
	3	3	3	0	−0.22	−0.27	−0.51
4+	2	2	4	0	1.02	0.55	0.00
	2	3	4	0	0.10	−1.10	0.00
	4	2	4	0	1.70	−0.21	−0.88
	4	3	4	0	0.48	−1.20	−0.21
5−	3	2	5	0	1.12	0.82	0.40
	3	3	5	0	0.55	−0.54	−1.00

TABLE 4.6

LEGENDRE COEFFICIENTS FOR $^{27}Al(p,\alpha_1)$ ANGULAR DISTRIBUTIONS WITH NO CHANNEL SPIN OR ℓ MIXING

J^π	l	s	l′	s′	a_2	a_4	a_6
1−	1	2	1	2	0.02	0.00	0.00
	1	2	3	2	0.07	0.00	0.00
	3	2	1	2	0.08	0.00	0.00
	3	2	3	2	0.32	0.00	0.00
	3	3	1	2	−0.10	0.00	0.00
	3	3	3	2	−0.39	0.00	0.00
1+	2	2	2	2	0.50	0.00	0.00
	2	3	2	2	−0.14	0.00	0.00
2−	1	2	1	2	0.70	0.00	0.00
	1	2	3	2	−0.19	0.00	0.00
	1	3	1	2	−0.20	0.00	0.00
	1	3	3	2	0.05	0.00	0.00
	3	2	1	2	−0.20	0.00	0.00
	3	2	3	2	0.05	0.65	0.00
	3	3	1	2	0.37	0.00	0.00
	3	3	3	2	−0.10	−0.43	0.00
2+	2	2	2	2	0.07	0.21	0.00
	2	3	2	2	0.18	−0.05	0.00
3−	1	2	1	2	0.48	0.00	0.00
	1	2	3	2	0.25	0.00	0.00
	1	3	1	2	−0.60	0.00	0.00
	1	3	3	2	−0.31	0.00	0.00
	3	2	1	2	0.25	0.00	0.00
	3	2	3	2	0.13	0.41	0.52
	3	3	1	2	−0.13	0.00	0.00
	3	3	3	2	−0.07	0.14	−0.21
3+	2	2	2	2	0.06	1.01	0.00
	2	3	2	2	−0.11	−0.67	0.00
4−	1	3	3	2	0.39	0.00	0.00
	3	2	3	2	0.40	0.08	1.02
	3	3	3	2	0.07	0.18	−0.93
4+	2	2	2	2	0.80	0.21	0.00
	2	3	2	2	0.08	−0.42	0.00
5−	3	2	3	2	0.96	0.48	0.10
	3	3	3	2	0.48	−0.32	−0.26

In the present experiment, a total of sixty-six resonances were observed and fit in the excitation functions for proton scattering from ^{29}Si in the range E_p = 1.29 - 3.30 MeV. Twenty-eight of these resonances had not previously been fit and five of these had not been observed as resonances in elastic scattering. The extracted resonance parameters are listed in tables 4.7 and 4.8.

The four angle excitation functions for proton elastic scattering from ^{29}Si in the energy range 1.29 - 2.50 MeV are shown in figure 4.17. The data are plotted using the uncorrected energies, thus the resonances appear at slightly different energies from those listed with the resonance parameters. Thirty-one resonances were observed in this energy range. Inelastic decay to the first excited state of ^{29}Si (not shown) was observed for four of these resonances. The lowest of these four states is a d-wave resonance at E_p = 2.0789 MeV with J = 3. The p_1 decay must have ℓ = 2, thus the inelastic reduced width is quite large for this state.

There is good agreement with the $^{29}Si(p,\gamma)$ data (Harris 1969) in the range E_p = 1.1 - 1.8 MeV. Of the 15 (p,γ) resonances only three were not observed in elastic scattering. These are located at E_p = 1.324, 1.746, and 1.749 MeV. The spin assignments below E_p = 1.8 MeV agree with previous results.

The only previous elastic scattering data for which any detailed analysis has been performed are those of Poirier et al., (1970) in the range E_p = 1.1 - 2.5 MeV and Hemsky et al. (1973) for E_p = 2.5 - 3.3 MeV. In general, the resonance energies of Poirier et al. are higher than those of the present measurement, with the difference increasing with energy to a maximum of about 5 keV. Other major differences are the following: (1) The 1.506 MeV, $J^\pi = 4^-$ analog state was reported to be a doublet. This resonance was remeasured several times with better resolution than in the

$R_0 = ?$

NELSON PhD 1983

ANALOG STATES ↓

TABLE 4.7

RESONANCE PARAMETERS FOR $^{29}Si(p,p)$ AND $^{29}Si(p,p_1)$

	E_p [a] (MeV)	J^π [b]	ℓ [c]	ξ	ε	Γ_p [d] (keV)	γ_p^2 [e] (keV)	ℓ_1	ξ_1	ε_1 [f]	Γ_{p_1} [d] (keV)	$\gamma_{p_1}^2$ [e] (keV)
	1.3020	$(0,1)^+$	0			0.025	0.43					
	1.3268	2^-	1		0.0	3.1	150.					
	1.3737	1^-	1	0.0		5.4	220.					
	1.4709	2^-	1		0.0	0.70	20.					
	1.5023	$(2,3,4)^-$	3	1.0		0.020	67.					
A	1.5060	4^-	3			0.045	150.					
	1.6393	1^-	1	0.5		15.	250.					
A	1.6639	$2,(1)^+$	2	1.0		0.030	3.3					
A	1.6685	0^+	0			0.16	0.86					
A	1.6844	2^-	1		0.0	4.5	65.					
	1.7698	1^-	1	1.0		0.11	1.2					
	1.7715	$2,(4)^-$	3		∞	0.045	50.					
A	1.7881	1^-	1	0.45		16.5	179.					
	1.9637	1^+	0		0.0	3.5	10.					
	2.0336	$3,(1)^+$	2		0.0	0.040	1.5					
	2.0361	$(1,2,3)^+$	2	1.0		0.040	1.5					
	2.0535	2^-	3		∞	0.17	75.					
	2.0789	3^+	2		0.0	0.23	7.5	2	1.0	0.0	0.015	380.
	2.1203	3^+	2		0.0	0.065	1.9					
	2.2223	1^-	1	0.55		52.	230.					
	2.2294	1^+	0		0.0	0.53	1.0					
	2.2679	$(2,3,4)^-$	3	1.0		0.017	4.1					
	2.2849	$(2,3,4)^-$	3	1.0		0.010	2.3					

TABLE 4.7-Continued

E_p[a] (MeV)	J^π[b]	ℓ[c]	ξ	ε	Γ_p[d] (keV)	γ_p^2[e] (keV)	ℓ_1	ξ_1	ε_1[f]	Γ_{p_1}[d] (keV)	$\gamma_{p_1}^2$[e] (keV)
2.3095	$(2,3)^-$	3	1.0		0.050	11.	1	0.0	0.0	0.40	120.
2.3588	4^-	3			0.015	2.9					
2.3771	2^-	1		0.0	70.	240.					
2.4063	2^+	2	1.0		0.38	6.1	0[g]		0.0	0.020	1.0
2.4183	0^+	0			28.	41.					
2.4866	0^+	0			1.0	1.4					
2.4901	1^-	1	0.98		4.3	12.	1	0.85	0.0	0.35	37.
2.4979	$(1,2,3)^+$	2	1.0		0.65	0.88	0[g]		0.0	0.002	0.060
2.5056	2^+	2	0.0		0.16	2.1	0[g]		0.0	0.11	3.2
2.5221	$2,(1)^-$	1	1.0	0.0	0.050	0.14	1	0.0	0.0	2.2	200.
2.5881	1^+	0		0.0	7.4	9.1					
2.5992	2^+	2	1.0		0.32	3.6	0		-.50	0.75	94.
2.6602	1^-	1	1.0		1.7	3.9	1	0.5	0.0	0.18	8.6
2.6761	1^+	0		0.0	18.	20.					
2.6826	3^-	3	1.0		0.70	6.5	1	1.0	0.0	0.60	26.
2.7019	4^-	3			0.040	3.6	3	h		0.010	61.
2.7027	0^+	0			13.	14.					
2.7057	0^-	1			30.	65.					
2.7745	2^-	3		∞	0.060	4.6	1	0.30	0.0	0.26	7.9
2.7766	2^+	2	0.80		1.3	11.	0		0.0	0.030	0.30
2.8188	1^+	0		-0.30	6.0	9.5	0[g]		0.0	2.7	24.
2.8509	4^-	3			0.17	11.	3	h		0.002	6.0
2.8529	2^-	1		0.0	2.4	4.4	1	0.35	0.0	1.0	24.

TABLE 4.7-Continued

E_p[a] (MeV)	J^π[b]	ℓ[c]	ξ	ε	Γ_p[d] (keV)	γ_p^2[e] (keV)	ℓ_1	ξ_1	ε_1[f]	Γ_{p_1}[d] (keV)	$\gamma_{p_1}^2$[e] (keV)
2.8886	3^+	2		0.0	0.10	0.72	2	1.0	0.0	0.020	3.1
2.9014	2^+	2	0.20		0.24	1.7	0		0.0	0.40	2.7
2.9115	3^-	3	0.0		0.040	2.4	1		0.0	0.060	1.1
2.9361	2^+	2	0.30		1.3	8.7	0		0.0	0.10	0.62
2.9562	1^+	0		0.75	2.3	6.5	2	0.5	∞	0.60	73.
2.9902	4^-	3			0.10	5.2	3	h		0.016	27.
3.0042	1^-	1	0.70		37.	58.	1	0.0	0.0	2.0	29.
A 3.0253	0^-	1			200.	300.					
3.0656	1^-	1	0.20		25.	37.	1	0.5	0.0	4.4	54.
3.0914	2^+	2	0.90		0.50	2.7	0		0.0	0.60	2.6
3.1299	2^+	2	0.0		0.60	3.1	0	1.0	-0.33	1.0	10.
3.1379	1^+	2		∞	3.0	15.	0[g]		0.0	15.	58.
3.1432	4^-	3			0.45	18.	3	h		0.010	9.4
3.1537	3^-	1	0.20		0.60	23.	1		0.0	0.50	4.9
3.1594	2^+	2	1.0		0.12	0.60	0		0.0	0.020	0.070
3.1741	2^-	1		0.0	4.0	5.4	1	0.95	0.0	1.8	17.
3.1821	2^-	1		0.0	1.5	2.0	1	0.30	0.0	0.14	1.3
3.2224	1^+	0		0.50	38.	59.	0[g]	0.20	i	10.	130.
3.2451	4^-	3			0.30	10.					
3.2656	(1^+)	2			3.0	13.	0[g]		0.0	30.	90.

[a]Laboratory energies are quoted. The absolute energies should be accurate within 3 keV. Except for very large resonances, the relative energies over a

TABLE 4.7-Continued

small energy range should be accurate within a few hundred eV.

[b]Spin assignments have been listed according to the following convention: 0^+ definite spin and parity; $1,(0)^+$ definite ℓ value, preferred spin outside of parentheses; $(0,1)^+$ definite ℓ value, spin not completely determined; (0^+) possible ℓ value and J^π.

[c]For ε infinite the higher ℓ value is listed.

[d]If several spins are listed, the widths and mixing ratios are given for the first spin listed.

[e]Total reduced widths corresponding to the total laboratory widths listed are calculated according to eqn. 2.4.

[f]Except as noted, simultaneous channel spin mixing and ℓ mixing were not observed; values correspond to the channel spin listed.

[g]Parameters quoted for inelastic decay are for the lowest possible ℓ values in cases where more than one fit is possible.

[h]The exit channel spin is undetermined.

[i]$\varepsilon_1(1) = 0.0$, $\varepsilon_1(2)$ infinite.

TABLE 4.8

RESONANCE PARAMETERS FOR $^{29}Si(p, p_2)$

E_p[a] (MeV)	J^π	ℓ_2	ξ_2	ε_2	Γ_{p_2} (keV)	$\gamma^2_{p_2}$ (keV)
3.1299	2^+	0		0.0	0.15	10.
3.1432	4^-	1		0.0	0.080	18.
3.1537	3^-	1	1.0	0.0	0.20	42.
3.1594	2^+	0		0.0	0.18	10.
3.1741	2^-	1	0.0	0.0	0.50	93.
3.1821	2^-	1	0.0	0.0	0.50	89.
3.2451	4^-	1		0.0	0.010	1.2

[a]Conventions are the same as in table 4.7.

Figure 4.17 The differential cross sections for $^{29}Si(p,p)$ in the energy range E_p = 1.29 to 2.5 MeV. The solid line is an R-matrix fit to the data.

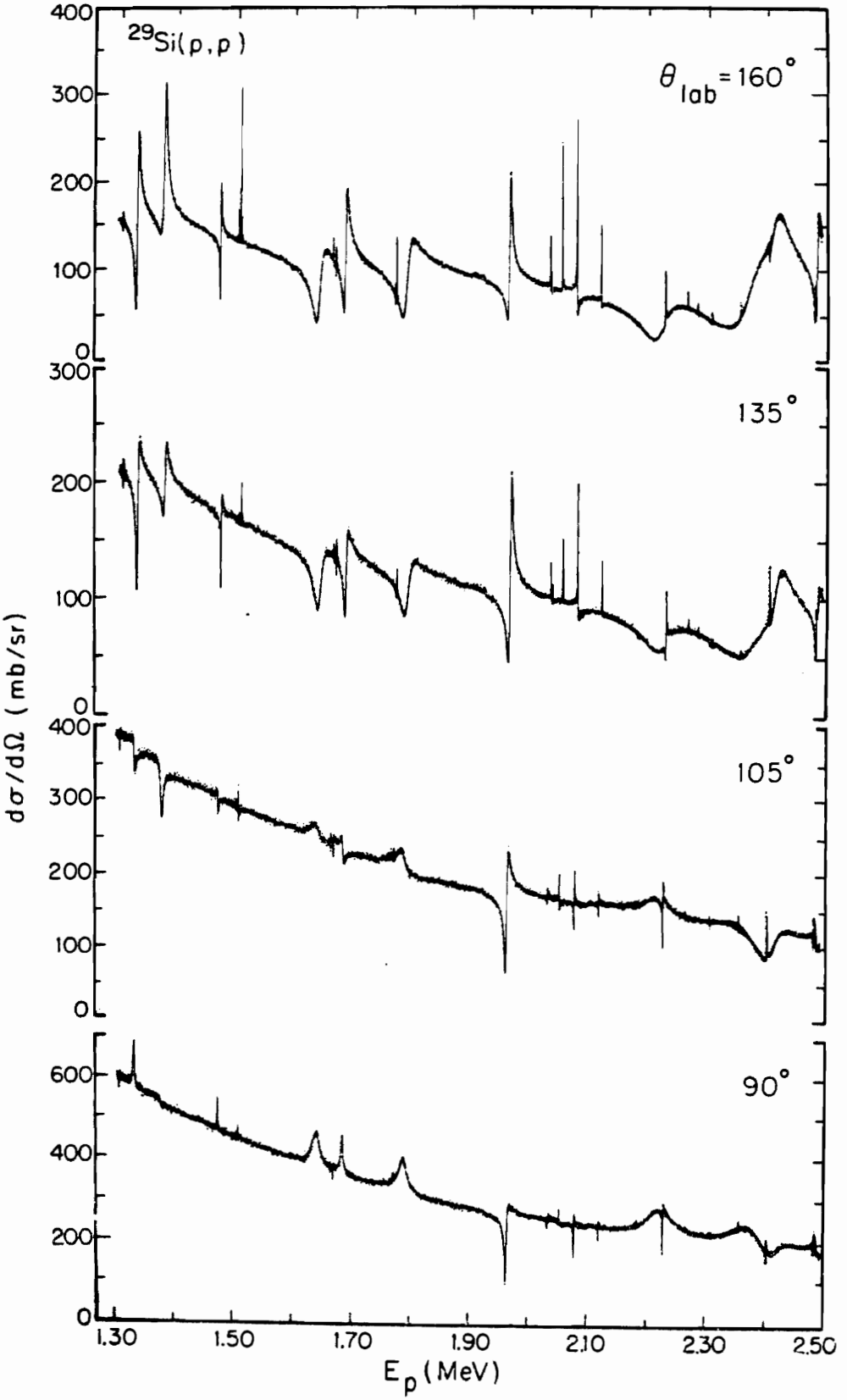
^{29}Si(p,p)
θ_{lab}=160°
135°
105°
90°
dσ/dΩ (mb/sr)
E_p (MeV)
1.30
1.50
1.70
1.90
2.10
2.30
2.50

previous measurement and no doublet structure was observed. The f-wave resonance at E_p = 1.5023, which was poorly resolved by Poirier et al., may be part of a 4^- doublet. (2) The resonances at E_p = 1.7691 and 1.7708 MeV were not observed in earlier elastic scattering measurements. (3) Three new levels were observed at 2.0336, 2.2659, and 2.2829 MeV. (4) The 2.2275 MeV level was assigned J = 1 rather than J = 0. (5) No evidence was seen for the 2.337 MeV, 0^+ resonance with a reported width of 15 keV. Also in this same energy region the 2.3771 and 2.3588 MeV states were located 8 keV higher than in the previous results. (6) Significantly lower channel spin mixing ratios were previously assigned for the $J^\pi = 1^-$ states at 2.222 and 2.490 MeV. (7) Widths for eight resonances varied more than 30% from the present values. The less comprehensive analysis and poorer resolution probably account for most of these differences.

Figure 4.18 shows the ^{29}Si(p,p) and (p,p_1) differential cross sections in the energy range E_p = 2.39 to 3.31 MeV at four angles. The solid line is the R-matrix fit to the data. Achieving satisfactory fits was more difficult in the higher energy region due to the increased level density, and the resulting increased interference effects. The presence of the broad $J^\pi = 0^-$ level at E_p = 3.03 MeV was not apparent until the other large states in this region had been fit. Although the cross sections above 2 MeV are very different from Rutherford, they are well reproduced by the inclusion of all of the observed resonances and of Rutherford and hard sphere scattering.

The comparison with the data and analysis of Hemsky et al. is also qualitatively good with the following exceptions: (1) The 2.8474 MeV resonance was assigned J = 2 instead of J = 4. (2) The resonance at 2.9802 MeV has ℓ = 3, not ℓ = 4. (3) The channel spin mixing ratios previously assigned for the resonances at 2.5056, 2.6602, and 2.8529 MeV are very different from those in this work. (4) The ℓ mixing ratios for the states at

Figure 4.18 The differential cross sections for $^{29}Si(p,p)$ and $^{29}Si(p,p_1)$ in the energy range E_p = 2.4 to 3.3 MeV. The solid line is an R-matrix fit to the data.

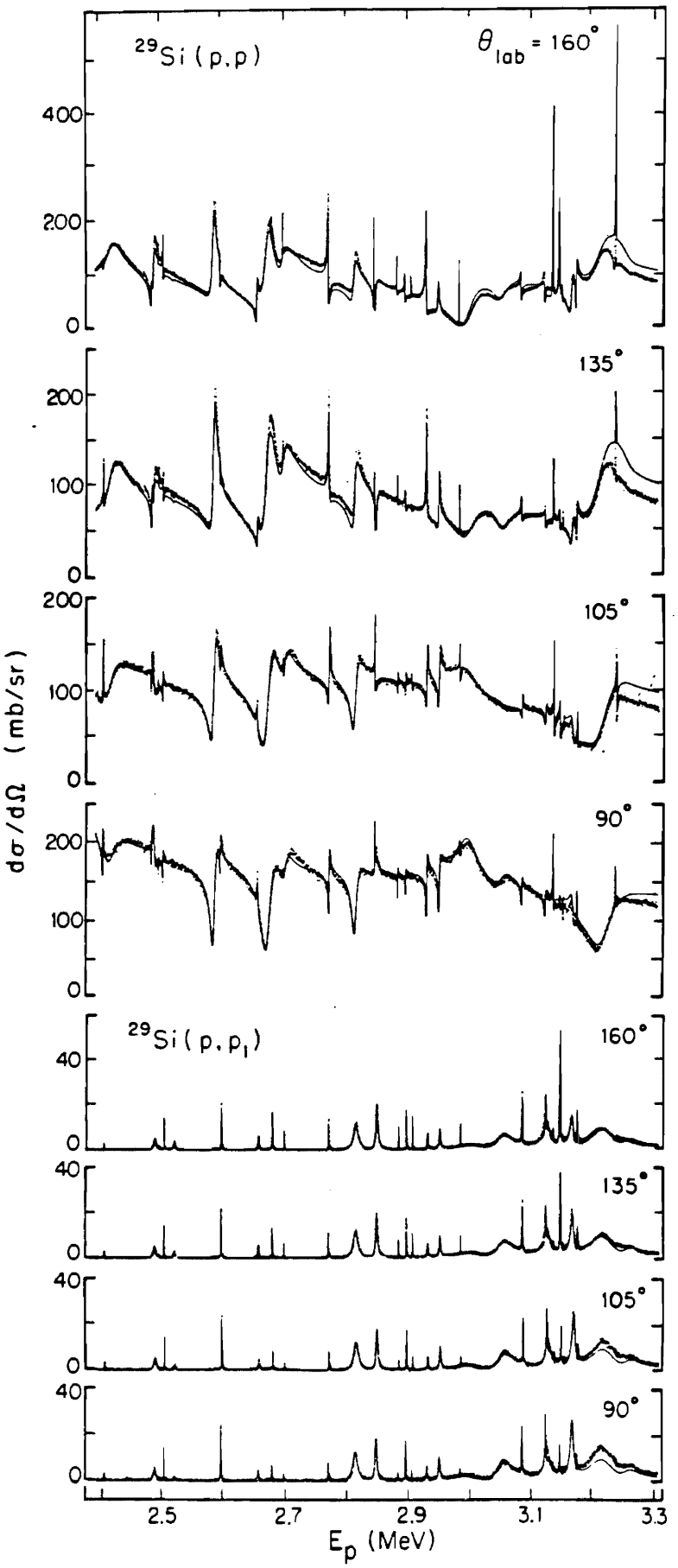
^{29}Si (p,p)
θ_{lab} = 160°
135°
105°
90°
^{29}Si (p,p$_1$)
160°
135°
105°
90°
dσ/dΩ (mb/sr)
E$_p$ (MeV)
2.5
2.7
2.9
3.1
3.3

2.5881 and 2.6761 were nonzero in the previous analysis. (5) Almost all of the widths differed some 30 to 60% from the present results. These discrepancies can be attributed to our improved treatment of resonance interference, better normalization procedures, and more precise treatment of the inelastic widths. Some 23 resonances analyzed in the present study were omitted in the previous analyses.

The errors associated with the fit parameters listed in tables 4.7 and 4.8 have been estimated by examining the range over which each parameter could be varied without appreciably degrading the fit. Below 2.7 MeV the errors were smaller than in the more complicated higher energy regions. As a guide the errors in the widths are 10% below 2.7 MeV and 20% above 2.7 MeV. Typical errors in the channel spin mixing ratios are 8% below 2.7 MeV and 15% above this energy, while the errors in the ℓ-mixing ratios are 10% for small isolated resonances and up to 30% for the broad overlapping resonances.

2. Proton Scattering from ^{27}Al

A total of 104 resonances were observed in proton scattering from ^{27}Al in the energy range E_p = 0.992 - 3.050 MeV. Most of the resonances below E_p = 1.7 MeV were known from a previous ^{27}Al(p,γ) study (Maas 1978). Only 18 resonances had previously been measured and analyzed in elastic scattering (Tveter 1972). Definite ℓ values were assigned for all of the levels seen in elastic scattering. Definite spin assignments were made for many of the resonances. If a spin assignment could not be made on the basis of the present data, then the spin (if any) listed by Endt (1978) was adopted. The resonance parameters are listed in tables 4.9, 4.10, and 4.11. For resonances where several solutions were possible an attempt was made to indicate all possible solutions in these tables.

The errors in the widths are estimated to be 10% below E_p = 2.4 MeV,

$R_0 = 2$

NELSON PhD 1983

TABLE 4.9

RESONANCE PARAMETERS FOR $^{27}Al(p,p)$ AND $^{27}Al(p,\alpha_0)$

	E_p[a] (MeV)	J^π[b]	ℓ[c]	ξ	ψ_2[d] (deg)	ψ_3[d] (deg)	Γ_p[e] (keV)	γ_p^2[f] (keV)	ℓ_{α_0}	Γ_{α_0}[e] (keV)	$\gamma_{\alpha_0}^2$[f] (keV)
	0.9370	3^-	1	0.8	0	0	0.10	28.	3	0.008	17.
A	0.9919	$(2)^+$	0	0.0	0		0.10	5.0			
		$(3)^+$	0	1.0		0	0.070	3.5			
A	1.0253	2^+	0	0.0	0		0.11	4.5			
A	1.1189	4^-	1	1.0		0	0.70	62.			
	1.1841	2^+	0	0.2	0	90	0.41	56.	2	0.25	46.
A	1.2008	3^-	1	0.0	0		5.4	320.			
			1	0.9	0	0	5.4	320.			
	1.2637	3^+	0	1.0		0	0.035	0.48			
	1.3183	4^+	2	1.0			0.030	9.6	4	0.005	11.
	1.3300	$(2)^+$	0	0.0	0		0.040	0.43			
		$(3)^+$	0	1.0		0	0.030	0.32			
	1.3656	2^+	0	0.03	-6	90	0.55	11.	2	0.40	36.
	1.3826	2^+	0	0.0	0		0.78	7.0			
A	1.3893	3^+	0	1.0		0	0.60	5.3			
A	1.3895	2^+	0	0.0	0		0.20	1.7	2	0.030	2.5
	1.4406	1^-	1	0.0	0		0.25	5.7	1	1.45	42.
	1.4575	4^-	1	1.0		0	2.3	49.			
	1.5033	3^+	0	1.0		0	0.55	3.4			
A	1.5196	2^-	1	0.32	0	0	3.7	65.			
	1.5660	4^+	2	0.8			0.010	1.4	4	0.010	8.2

TABLE 4.9-Continued

	E_p[a] (MeV)	J^π[b]	ℓ[c]	ξ	ψ_2[d] (deg)	ψ_3[d] (deg)	Γ_p[e] (keV)	γ_p^2[f] (keV)	ℓ_{α_0}	Γ_{α_0}[e] (keV)	$\gamma_{\alpha_0}^2$[f] (keV)
	1.5784	4^-	1	1.0		0	2.4	35.			
	1.5788	2^+	0	0.0	0		0.050	0.26	2	0.18	7.9
	1.6472	3^-	1	0.71	0	0	0.28	3.4	3	0.070	8.6
	1.6662	2^+	0	0.00	17		1.85	20.			
			0	0.09	0	90	1.85	20.			
A	1.6645	1^+	2	g			0.45	38.			
A	1.6798	2^+	0	0.0	0		0.21	0.84			
		$(3)^+$	0	1.0		0	0.15	0.60			
	1.7055	2^+	0	0.0	0		1.1	4.2			
	1.7234	3^-	1	0.93	0	0	7.3	72.	3	1.6	153.
A	1.7243	5^-	3	0.75			0.25	269.			
	1.7481	2^-	1	0.05	0	0	6.6	62.			
	1.7974	4^-	1	1.0		0	1.1	9.1			
A	1.7998	1^+	2	g			0.20	11.			
	1.8410	4^+	2	0.7			0.55	2.7	4	0.006	1.9
	1.8981	4^+	2	0.1			0.060	2.4	4	0.08	21.
	1.9060	1^-	1	0.0	0		19.	124.	1	0.80	6.2
	1.9090	5^+	2	1.0			0.080	3.3			
	1.9637	2^-	1	0.0	0		4.0	23.			
	1.9680	2^+	0	0.15	0	90	1.4	9.9	2	0.04	0.58
	1.9774	3^-	1	0.9	0	0	31.	173.	3	1.0	45.

TABLE 4.9-Continued

E_p[a] (MeV)	J^π[b]	ℓ[c]	ξ	ψ_2[d] (deg)	ψ_3[d] (deg)	Γ_p[e] (keV)	γ_p^2[f] (keV)	ℓ_{α_0}	Γ_{α_0}[e] (keV)	$\gamma_{\alpha_0}^2$[f] (keV)
2.0329	2^+	0	0.06	0	90	8.5	32.	2	0.15	1.8
2.0450	5^+	2	1.0			0.15	4.4			
2.0485	3^+	0	0.93	90	0	1.8	7.0			
		0	1.0	0	15	1.8	7.0			
2.1069	2^-	1	0.06	0	0	11.	49.			
2.1262	3^+	0	0.80	90	0	0.57	3.8			
		0	1.0		27	0.57	3.8			
2.1308	2^+	0	0.01	13	90	5.0	16.	2	0.65	6.3
2.1313	(1^-)	1	0.0	0		0.030	0.13			
	(2^+)	0	0.0	0		0.12	0.21			
2.1549	$(3)^-$	1	0.4	+31	0	0.38	18.			
	$(4)^-$	1	1.0		+31	0.45	35.			
		1	0.2	90	0	0.39	18.			
A 2.1595	4^+	2	0.5			0.17	3.9	4	0.08	9.7
2.1711	2^+	0	0.3	10	90	0.43	3.4	2	0.9	8.0
2.2002	2^+	2	g	90	90	0.50	10.4			
	$(3)^+$	2	1.0		90	0.30	6.2			
2.2003	4^+	2	0.25			0.04	0.83	4	0.15	16.
2.2056	3^-	1	0.6	0	0	20.	75.			
2.2293	1^-	1	0.0	0		35.	126.			
2.2860	3^-	1	0.08[h]	-6	90	2.7	54.			

TABLE 4.9-Continued

E_p[a] (MeV)	J^π[b]	ℓ[c]	ξ	ψ_2[d] (deg)	ψ_3[d] (deg)	Γ_p[e] (keV)	γ_p^2[f] (keV)	ℓ_{α_0}	Γ_{α_0}[e] (keV)	$\gamma_{\alpha_0}^2$[f] (keV)
2.3032	4^+	2	0.0			0.15	2.5	4	0.007	0.58
2.3105	1^-	1	0.0	0		2.0	6.3	1	1.7	5.5
2.3120	3^+	0	1.0		0	0.32	0.46			
2.3300	4^-	1	0.95[h]	90	0	2.3	34.			
2.3607	3^-	1	0.70	0	0	2.4	7.1	3	1.2	20.
2.3731	3^-	1	0.0	0		3.2	9.3	3	3.0	50.
2.3902	$(3)^-$	3	g			0.070	11.			
	$(4)^-$	3	g			0.055	8.6			
	$(5)^-$	3	0.0			0.040	6.3			
	$(6)^-$	3	1.0			0.035	5.2			
2.4030	1^-	1	0.0	0		2.5	6.9	1	0.20	0.55
2.4418	2^+	0	0.0	0		2.2	5.1	2	3.0	15.
2.4716	4^+	2	0.5			0.050	0.60	4	0.2	11.
2.4751	2^+	0	0.4	0	90	1.5	8.4	2	1.0	4.7
2.4827	4^+	2	0.0			2.4	29.			
2.4872	5^-	3	1.0			0.33	41.			
2.4883	2^+	2	0.0	90		0.30	3.6	2	0.08	0.37
2.5172	4^+	2	1.0			0.080	0.91	4	0.005	0.24
2.5304	1^-	1	0.0	0		3.0	7.0			
2.5436	$(3)^-$	1	1.0		0	45.	104.			
2.5553	5^+	2	1.0			1.2	13.			
	$(4)^+$	2	0.0			1.8	20.			
2.5560	2^+	0	0.0[h]	-24		2.4	6.5			

TABLE 4.9–Continued

	E_p[a] (MeV)	J^π[b]	ℓ[c]	ξ	ψ_2[d] (deg)	ψ_3[d] (deg)	Γ_p[e] (keV)	γ_p^2[f] (keV)	ℓ_{α_0}	Γ_{α_0}[e] (keV)	$\gamma_{\alpha_0}^2$[f] (keV)
	2.5728	2^+	0	0.5	0	90	4.0	23.	2	1.8	7.0
A	2.5829	$(2)^-$	1	0.4	0	0	36.	79.			
	2.5975	3^-	1	0.5	0	0	1.2	2.6	3	3.0	31.
A	2.6030	1^+	2	1.0			1.0	9.8			
	2.6044	4^+	2	0.0			0.20	2.0	4	0.8	32.
	2.6138	5^-	3	1.0			0.17	16.	5	0.03	6.3
	2.6703	4^-	1	1.0		+16	13.	110.			
		$(3)^-$	1	h			17.	140.			
A	2.7132	3^+	0	1.0		0	0.80	0.78			
	2.7216	4^+	2	0.0			1.0	8.2			
	2.7234	$(2)^-$	1	1.0		0	3.0	5.6			
	2.7263	5^+	2	1.0			0.60	4.9			
	2.7410	3^+	0	0.6[h]	90	−50	1.4	8.6			
	2.7592	$(3)^-$	1	1.0		0	35.	63.			
A	2.7620	2^+	0	0.0	0		25.	23.	2	0.90	2.5
	2.8099	2^+	0	0.0	0		0.60	0.54	2	0.2	0.52
	2.8148	4^+	2	0.0			0.20	1.4	4	1.2	30.
	2.8226	$(1)^-$	1	0.0			40.	68.			
	2.8458	4^+	2	0.7			0.17	1.2	4	0.38	8.9
	2.8505	$(4)^+$	2	0.0	0		0.090	0.61			
		$(5)^+$	2	1.0			0.070	0.47			
	2.8676	4^-	1	1.0		+12	2.3	9.4			

TABLE 4.9—Continued

E_p[a] (MeV)	J^π[b]	ℓ[c]	ξ	ψ_2[d] (deg)	ψ_3[d] (deg)	Γ_p[e] (keV)	γ_p^2[f] (keV)	ℓ_{α_0}	Γ_{α_0}[e] (keV)	$\gamma_{\alpha_0}^2$[f] (keV)
2.8750	6^-	3	1.0			3.7	209.			
2.8765	$(3)^-$	3	0.4[h]	90	90	2.0	116.	3	2.2	13.
2.8770	(2^-)	1	0.4	0	0	17.	27.			
2.8942	2^{+h}	0	0.0	0		16.	14.	2	0.60	1.4
2.9110	3^+	0	1.0		39	0.50	1.5			
2.9113	(0^+)	2	0.0[h]			1.0	6.2			
2.9207	3^-	3	0.7	90	90	0.19	10.			
	$(2)^-$	3	0.9		90	0.26	14.			
2.9556	3^+	0	1.0		23	19.	31.			
2.9968	$(5)^-$	3	0.0			0.18	8.3			
	$(6)^-$	3	1.0			0.15	7.0			
3.0171	2^+	0	0.0[h]	0		8.0	6.2	2	15.	29.
3.0171	3^+	0	0.85	90	0	5.3	7.8			
3.0397	3^-	3	0.3	90	90	0.28	1.2	3	0.10	0.45
3.0483	3^-	1	0.0	0		0.80	1.1	3	10.	45.

[a]Laboratory energies are quoted. The absolute energies should be accurate within 3 keV. Except for very large resonances, the relative energies over a small energy range should be accurate within a few hundred eV.

TABLE 4.9-Continued

[b]Spin assignments have been listed according to the following convention: 0^+ definite spin and parity; $1^+,(0)^+$ definite ℓ value, preferred spin outside of parentheses; $(0)^+,(1)^+$ definite ℓ value, spin not completely determined; (0^+) possible ℓ value and J^π. Several possible solutions may be listed for each J^π.

[c]For $\phi_2 = 90^\circ$ with $\xi = 0.0$, or $\phi_3 = 90^\circ$ with $\xi = 1.0$, or $\phi_2 = \phi_3 = 90^\circ$, the higher ℓ value is listed.

[d]When determined, the relative phase is indicated by + or −.

[e]Errors in the widths are estimated to be 20% for resonances with widths less than 100 eV and 10% for widths greater than 100 eV for energies less than 2.4 MeV. At energies above 2.4 MeV errors are larger due to local interference effects.

[f]Total reduced widths corresponding to the total laboratory widths listed are calculated according to eqn. 2.3 with $r_0 = 1.25$ fm.

[g]Parameter is undetermined for this resonance.

[h]Mixing ratio assignments for ξ, ϕ_2, and ϕ_3 are uncertain due to strong interference effects. The parameters listed were used in the fitting the data, but other solutions may be possible.

TABLE 4.10

RESONANCE PARAMETERS FOR $^{27}Al(p,p_1)$ AND $^{27}Al(p,p_2)$

E_p[a] (MeV)	J^π	ℓ_{p_1}	ξ_{p_1}[h]	Γ_{p_1} (keV)	$\gamma^2_{p_1}$ (keV)	ℓ_{p_2}	ξ_{p_2}[h]	Γ_{p_2} (keV)	$\gamma^2_{p_2}$ (keV)
1.7998	1^+	0	1.0	0.20	16.	0	0.0	0.050	16.
1.9060	1^-					1	g	0.60	308.
1.9680	2^+					0	1.0	0.080	24.
2.1069	2^-					1	0.7	0.35	46.
2.1313	(1^-)					1	g	0.30	34.
	(2^+)					0	1.0	0.40	11.
2.1711	2^+					0	1.0	0.27	7.1
2.2293	1^-					1	g	1.4	97.
2.3105	1^-	1	g	2.0	48.	1	g	2.0	95.
2.3607	3^-					1	1.0	0.20	7.7
2.3731	3^-					1	1.0	2.0	73.
2.4030	1^-	1	g	8.0	140.	1	g	3.0	98.
2.4418	2^+					0	1.0	0.60	5.4
2.4751	2^+					0	1.0	0.20	1.6
2.4883	2^+					0	1.0	0.15	1.2
2.5172	4^+					2	1.0	0.010	1.8
2.5304	1^-	1	g	6.5	79.	1	g	6.5	135.
2.5829	$(2)^-$	1	1.0	7.0	74.	1	0.5	4.0	70.
2.5975	3^-					1	1.0	0.10	1.7
2.6030	1^+	0	1.0	11.	41.				
2.7132	3^+					2	1.0	0.20	18.
2.7234	$(2)^-$	1	1.0	12.	90.	1	0.9	5.0	58.

TABLE 4.10—Continued

E_p[a] (MeV)	J^π	ℓ_{p_1}	ξ_{p_1}[h]	Γ_{p_1} (keV)	$\gamma^2_{p_1}$ (keV)	ℓ_{p_2}	ξ_{p_2}[h]	Γ_{p_2} (keV)	$\gamma^2_{p_2}$ (keV)
2.7410	3^+					2	g	0.10	8.0
2.7592	$(3)^-$					1	1.0	6.0	63.
2.7620	2^+					0	g	0.0	
2.8099	2^+					0	1.0	0.80	2.8
2.8226	$(1)^-$	1	g	9.0	55.	1	1.0	25.	226.
2.8770	$(2)^-$	1	1.0	16.	87.	1	1.0	10.	79.
2.8765	$(3)^-$					1	1.0	0.40	3.2
2.8942	2^+					0	1.0	10.	29.
2.9113	(0^+)	0	0.0	8.0	17.				
2.9207	3^-					1	1.0	0.10	0.72
	2^-					1	1.0	0.10	0.72
3.0397	3^-					1	1.0	0.15	0.84

[a]Conventions are the same as in table 4.9. The ℓ-mixing angles for inelastic decay are undetermined, $\phi_p = 0$ is assumed.

TABLE 4.11

RESONANCE PARAMETERS FOR $^{27}Al(p,\alpha_1)$

E_p[a] (MeV)	J^π	ℓ_{α_1}	Γ_{α_1} (keV)	$\gamma^2_{\alpha_1}$ (keV)
2.4418	2^+	0	0.20	18.
2.4716	4^+	2	0.020	6.6
2.4883	2^+	0	0.40	30.
2.5172	4^+	2	0.005	1.4
2.5728	2^+	0	0.30	16.
2.6044	4^+	2	0.13	25.
2.7132	3^+	2	0.10	12.
2.7410	3^+	2	0.60	67.
2.8099	2^+	0	0.40	9.2
2.8226	$(1)^-$	1	0.10	3.4
2.8458	4^+	2	0.070	5.3
2.8765	$(3)^-$	1	0.30	8.6
2.9110	3^+	2	0.22	13.
2.9207	3^-	1	0.18	4.5
	$(2)^-$	1	0.18	4.5
3.0171	2^+	0	2.0	24.
3.0171	3^+	2	0.50	21.
3.0397	3^-	1	0.40	6.9

[a]Conventions are the same as in table 4.9. The mixing angle φ is undetermined for the (p,α_1) reaction. $\varphi = 0$ is assumed.

and 20% above this energy. The estimated errors for the channel spin mixing ratios and ℓ-mixing ratios are listed in tables 4.12 and 4.13. The ranges of the elastic scattering channel spin mixing ratio and the ℓ-mixing angle, for which the various errors apply, were estimated from the catalogs of resonance shapes. These errors apply to states possessing widths much greater than the resolution width. For smaller widths the errors become much larger, and for states with alpha decay the errors on the mixing ratios are usually smaller due to the additional information from the α_0 angular distribution. The errors for incoherent ℓ-mixing appear in the channel spin mixing ratio, and do not change with the value of the mixing. In general, these errors in ξ are all less than ± 0.15.

The differential cross sections for ^{27}Al(p,p) and (p,α_0) are shown in figures 4.19 and 4.20 in the region E_p = 0.92 - 1.68 MeV. No inelastic decay was observed for the twenty-four resonances fit in this energy range. Ten resonances which are observed in ^{27}Al(p,γ) were not seen in this experiment. Three resonances seen in (p,p) were not listed as (p,γ) resonances.

There is good qualitative agreement with the previous elastic scattering experiment in the range E_p = 1.1 - 1.8 MeV. Nine of the smaller resonances were missed in the previous experiment. For the eighteen resonances analyzed previously the energies agree within errors with the present results, and all ℓ value assignments are in agreement. Different spins were assigned for three resonances. The state at E_p = 1.3876 MeV was previously listed as $J^\pi = 2^+$. This level interferes with two nearby 2^+ levels. The only possible assignment in the present analysis is $J^\pi = 3^+$. The two p-wave resonances at E_p = 1.4555 and 1.5759 MeV were listed as $J^\pi = 3^-$ by Tveter. In the present analysis the spins of these states were determined to be $J^\pi = 4^-$. The reported alpha decay to the ground state of

TABLE 4.12

RANGES OF THE CHANNEL SPIN MIXING RATIO ξ
CORRESPONDING TO VARIOUS ERRORS IN ξ

		Error in ξ				
ℓ	J	± 0.05	± 0.10	± 0.20	± 0.30	± 0.40
1	2		0.0–0.3	0.3–0.5	0.5–1.0	
1	3	0.8–1.0 0.0–0.1	0.6–0.8 0.1–0.3	0.3–0.6		
2	1				0.0–0.1	0.1–1.0
2	2				0.0–0.1	0.1–1.0
2	3		0.0–0.1	0.1–0.3	0.3–0.5	0.5–1.0
2	4		0.0–0.2	0.2–0.5	0.5–1.0	
3	1			0.9–1.0	0.0–0.9	
3	2		0.0–0.1	0.1–0.3	0.3–1.0	
3	3		0.0–0.3	0.3–0.4	0.4–1.0	
3	4	0.0–0.2	0.2–0.4 0.8–1.0	0.4–0.8		
3	5	0.0–0.3	0.3–0.5	0.5–1.0		

TABLE 4.13

RANGES OF THE ℓ-MIXING ANGLE ϕ CORRESPONDING TO VARIOUS ERRORS IN ϕ

s	J^{π}	Error in ϕ $\pm 10^{\circ}$	$\pm 20^{\circ}$
2	2^{+}	$+20 - +70^{\circ}$ $-70 - -20^{\circ}$	$+70 - +90^{\circ}$ $-70 - -90^{\circ}$ $-20 - +20^{\circ}$
3	3^{+}	$+20 - +70^{\circ}$ $-70 - -20^{\circ}$	$+70 - +90^{\circ}$ $-70 - -90^{\circ}$ $-20 - +20^{\circ}$
2	1^{-}	$+20 - +70^{\circ}$ $-70 - -20^{\circ}$	$+70 - +90^{\circ}$ $-70 - -90^{\circ}$ $-20 - +20^{\circ}$
2	2^{-}	$0 - +70^{\circ}$ $-70 - -20^{\circ}$	$+70 - +90^{\circ}$ $-70 - -90^{\circ}$ $-20 - 0^{\circ}$
3	2^{-}	$-70 - +70^{\circ}$	$+70 - +90^{\circ}$ $-70 - -90^{\circ}$
2	3^{-}	$+20 - +90^{\circ}$ $-70 - 0^{\circ}$	$0 - +20^{\circ}$ $-70 - -90^{\circ}$
3	3^{-}	$0 - +70^{\circ}$ $-70 - -20^{\circ}$	$+70 - +90^{\circ}$ $-90 - -70^{\circ}$ $-20 - 0^{\circ}$
3	4^{-}	$+20 - +90^{\circ}$ $-70 - 0^{\circ}$	$0 - +20^{\circ}$ $-90 - -70^{\circ}$

Figure 4.19 The differential cross sections for $^{27}Al(p,p)$ and $^{27}Al(p,\alpha_0)$ at 90^o and 105^o in the energy range E_p = 0.92 to 1.68 MeV. The solid line is an R-matrix fit to the data.

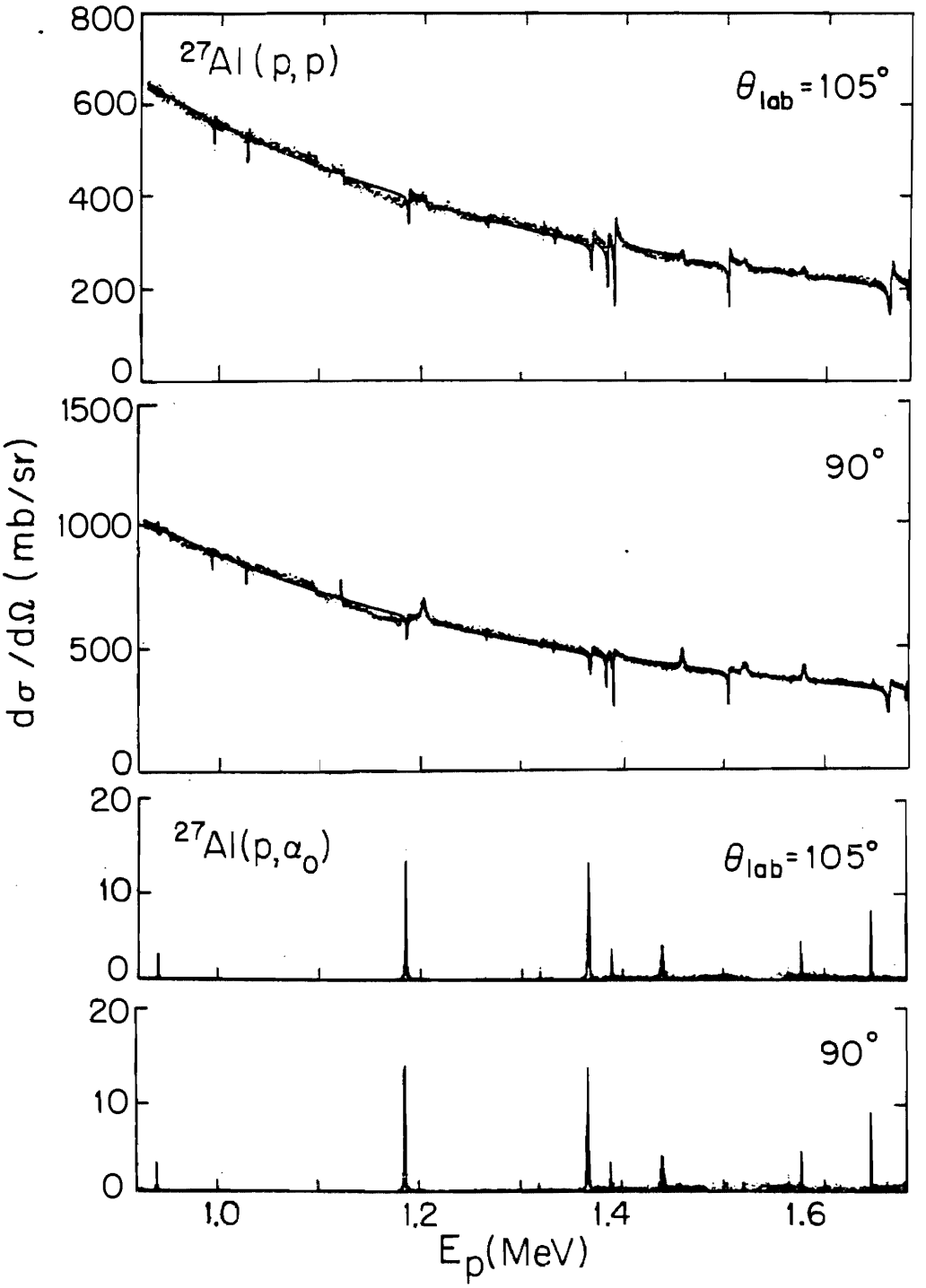
^{27}Al (p, p)
θ_{lab} = 105°
90°
^{27}Al(p,α_0)
θ_{lab} = 105°
90°
dσ /dΩ (mb/sr)
E_p(MeV)
800
600
400
200
0
1500
1000
500
0
20
10
0
20
10
0
1.0
1.2
1.4
1.6

Figure 4.20 The differential cross sections for $^{27}Al(p,p)$ and $^{27}Al(p,\alpha_0)$ for 135^o and 160^o in the energy range E_p = 0.92 to 1.68 MeV. The solid line is an R-matrix fit to the data.

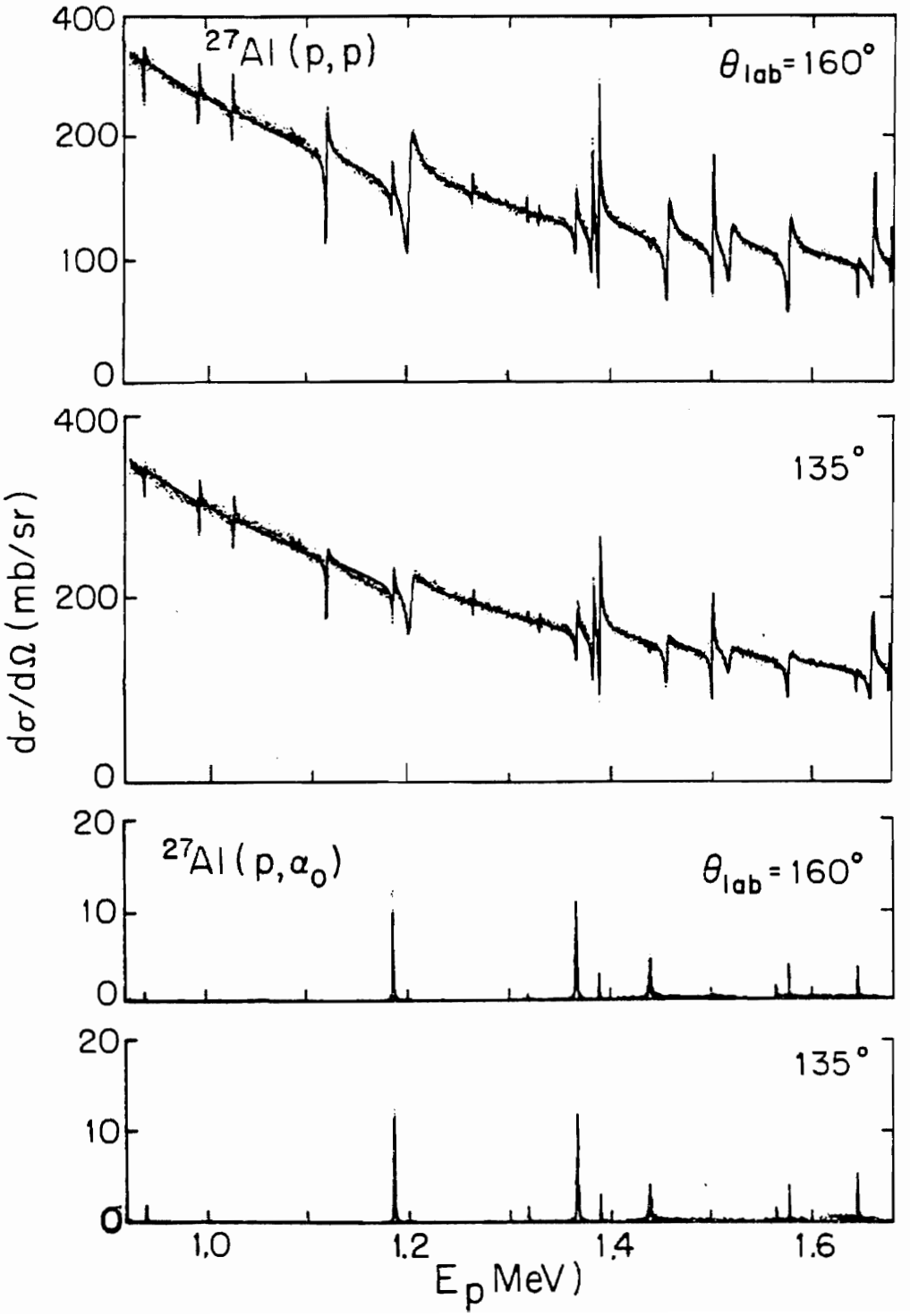
400
200
100
0
^{27}Al (p, p)
θ_{lab}= 160°
400
200
0
135°
dσ/dΩ (mb/sr)
20
10
0
^{27}Al (p, α_0)
θ_{lab} = 160°
20
10
0
135°
1.0
1.2
1.4
1.6
E$_p$ MeV)

^{24}Mg for the 1.5759 MeV resonance, which requires a spin assignment of 3^-, was not observed. The widths extracted in the two experiments agree within 25% or better except for the 2^+ resonances at E_p = 1.1832 and 1.3649 MeV, where the larger widths of Tveter are due to the different ℓ-mixing ratio assignments. Also the width of the 3^- resonance at E_p = 1.6443 was much smaller in the previous analysis, although the (p,α_0) widths and the channel spin mixing ratios are in agreement. Tveter did not present the data or fit for this state. All of the channel spin mixing ratios are in agreement, and the ℓ-mixing ratios agree within the large stated errors.

Information on the natural parity states in the range E_p = 1.18 - 2.60 MeV has been obtained from the ^{24}Mg(α,α_0) reaction (Cseh 1982). All of these results agree with the present experiment except for the observation of three $J^\pi = 0^+$ states at energies corresponding to E_p = 1.441, 1.505, and 1.709 MeV, and a $J^\pi = 1^-$ state at E_p = 1.276 MeV.

Above E_p = 2 MeV there was almost no previous resonance data. The data and R-matrix fits for the energy range E_p = 1.67 - 2.42 MeV are shown in figures 4.21, 4.22, 4.23, and 4.24, for laboratory angles of 90°, 105°, 135°, and 160°, respectively. In this energy region thirty-six resonances were observed, and the ^{27}Al(p,p_1) and (p,p_2) reactions were measured. The fitting was more difficult in this region due to the greater number of overlapping levels, but excellent fits were obtained for most of this energy range.

Figures 4.25, 4.26, 4.27, and 4.28 show the data and R-matrix fits for E_p = 2.42 - 3.05 MeV. The alpha decay to the first excited state of ^{24}Mg was measured in this region. The broad overlapping levels in this energy range made fitting difficult. To avoid introducing spurious resonances, a level was included in the fit only if there was clear evidence for its existence in one of the measured reaction channels. Satisfactory fits could

Figure 4.21 The differential cross sections for $^{27}Al(p,p)$, (p,p_1), (p,p_2), and (p,α_0) at 90^{o} in the energy range E_p = 1.67 to 2.42 MeV. The solid line is an R-matrix fit to the data.

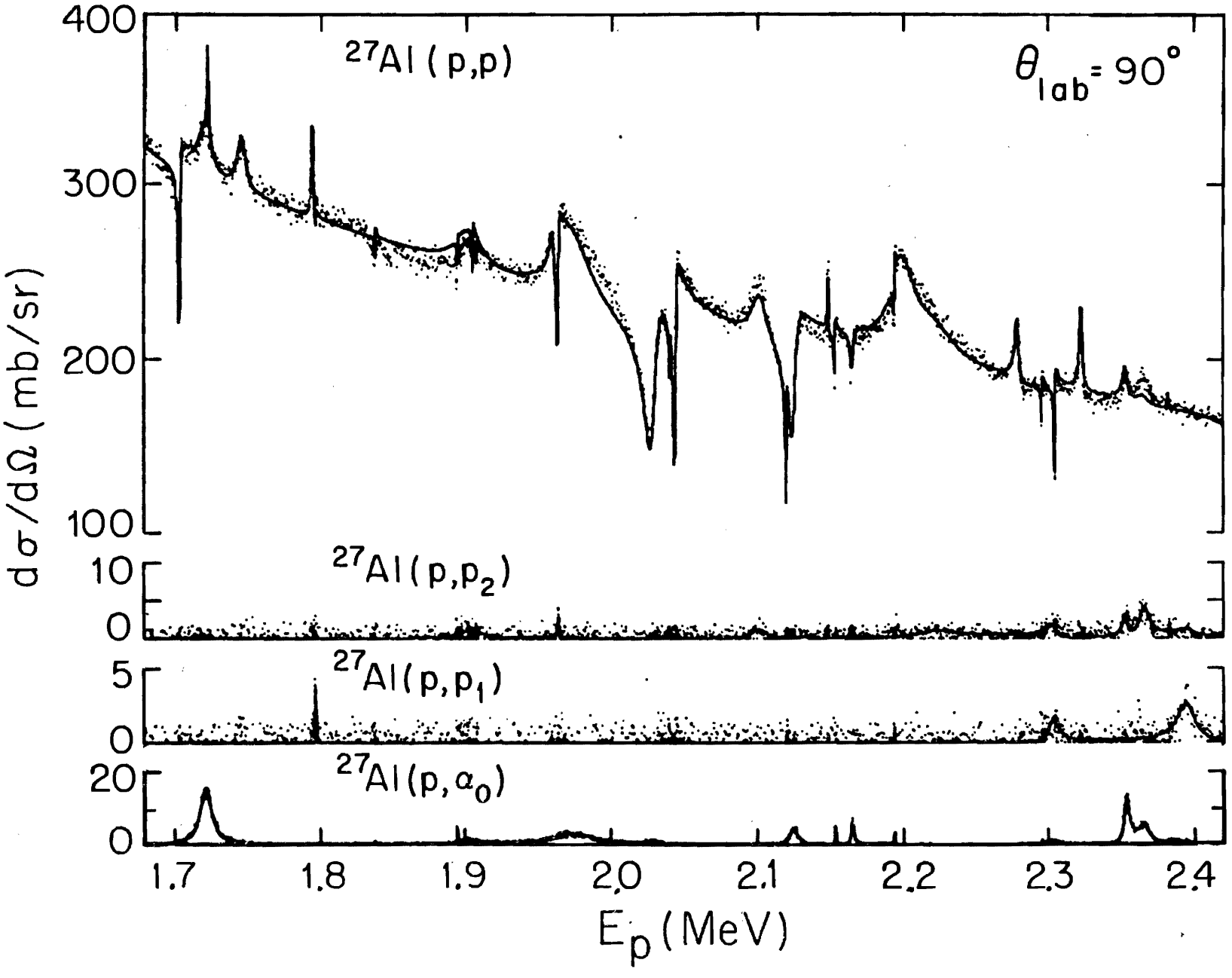
400
300
200
100
^{27}Al (p,p)
θ_{lab}= 90°
dσ/dΩ (mb/sr)
10
0
^{27}Al (p,p$_2$)
5
0
^{27}Al (p,p$_1$)
20
0
^{27}Al (p, α$_0$)
1.7
1.8
1.9
2.0
2.1
2.2
2.3
2.4
E$_p$ (MeV)

Figure 4.22 The differential cross sections for $^{27}Al(p,p)$, (p,p_1), (p,p_2), and (p,α_0) at 105^{o} in the energy range E_p = 1.67 to 2.42 MeV. The solid line is an R-matrix fit to the data.

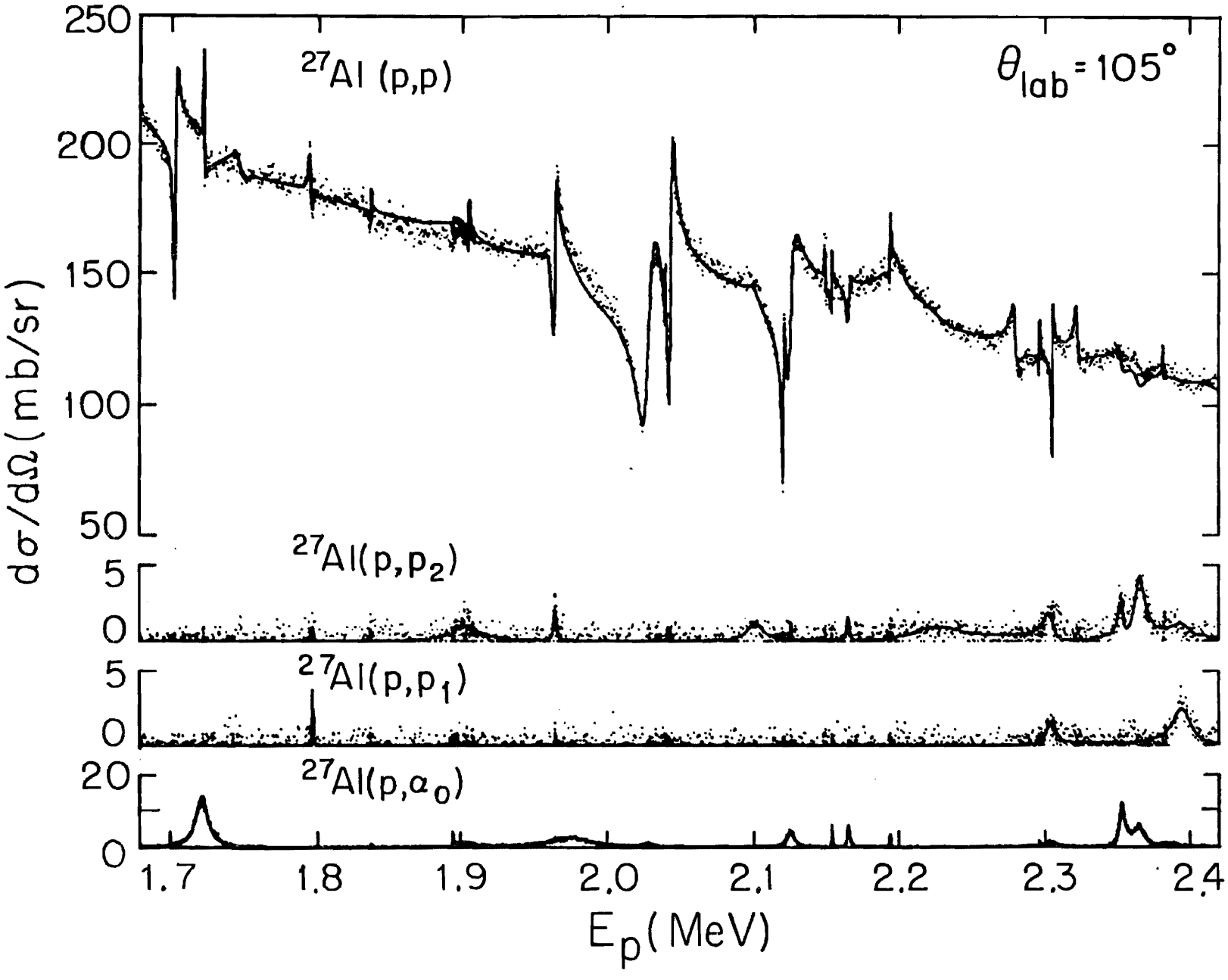
250
200
150
100
50
^{27}Al (p,p)
$\theta_{lab} = 105°$
dσ/dΩ (mb/sr)
^{27}Al(p,p$_2$)
5
0
^{27}Al(p,p$_1$)
5
0
^{27}Al(p,α$_0$)
20
0
1.7
1.8
1.9
2.0
2.1
2.2
2.3
2.4
E_p (MeV)

Figure 4.23 The differential cross sections for $^{27}Al(p,p)$, (p,p_1), (p,p_2), and (p,α_0) at 135^{o} in the energy range E_p = 1.67 to 2.42 MeV. The solid line is an R-matrix fit to the data.

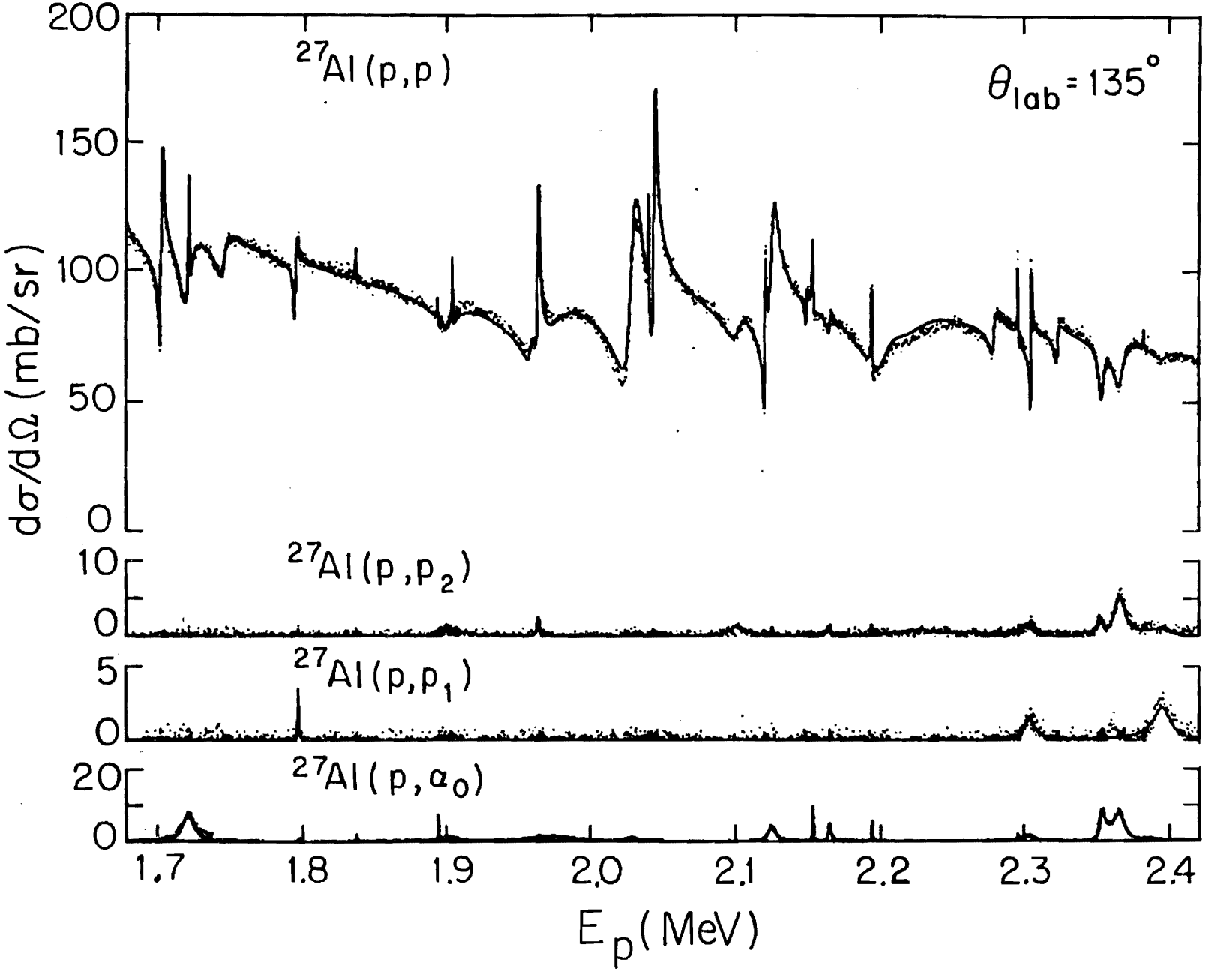
200
150
100
50
0
^{27}Al (p,p)
θ_{lab} = 135°
dσ/dΩ (mb/sr)
10
0
^{27}Al (p, p$_2$)
5
0
^{27}Al (p, p$_1$)
20
0
^{27}Al (p, α$_0$)
1.7
1.8
1.9
2.0
2.1
2.2
2.3
2.4
E$_p$ (MeV)

Figure 4.24 The differential cross sections for $^{27}Al(p,p)$, (p,p_1), (p,p_2), and (p,α_0) at 160^{o} in the energy range E_p = 1.67 to 2.42 MeV. The solid line is an R-matrix fit to the data.

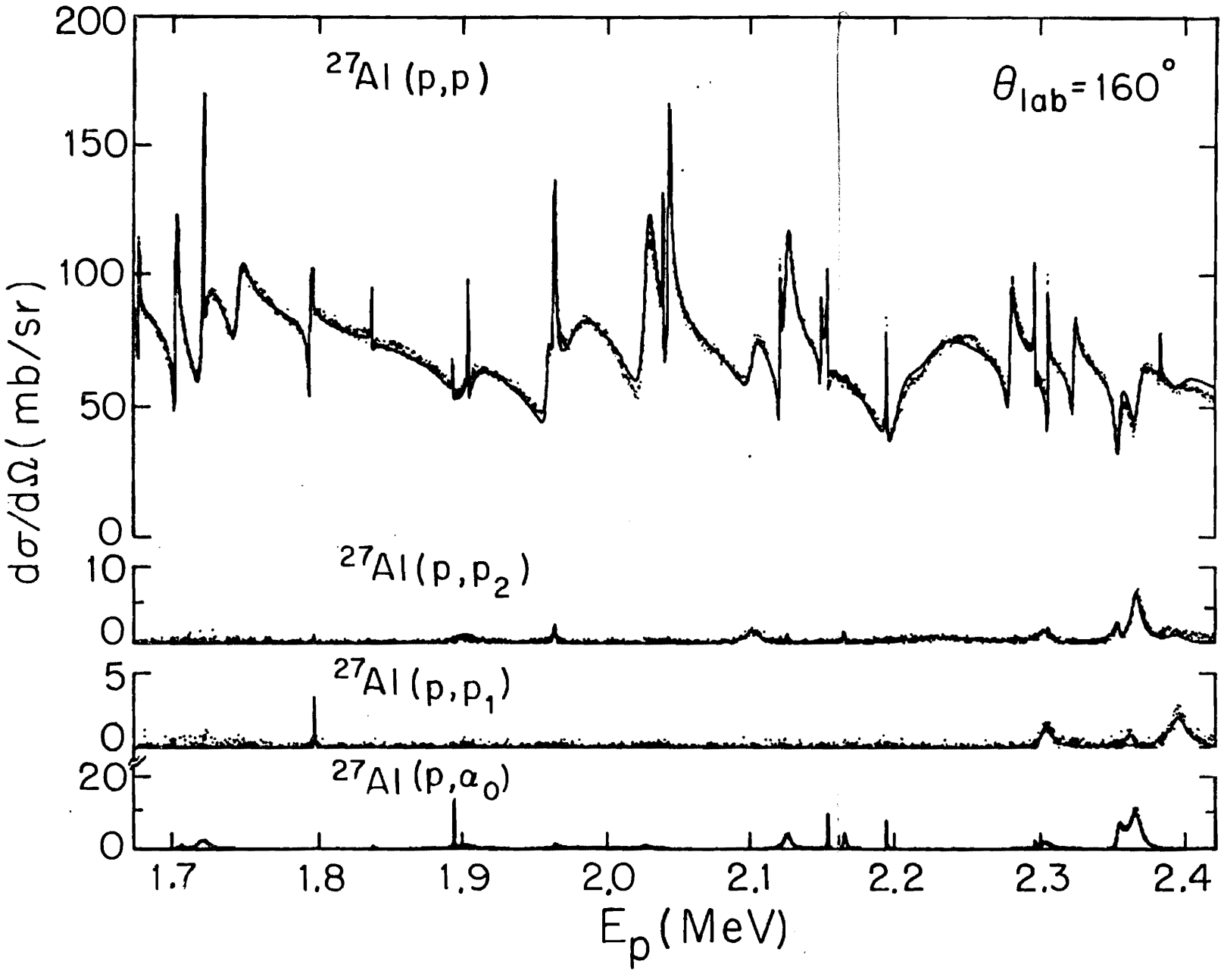
200
150
100
50
0
^{27}Al (p,p)
θ_{lab} = 160°
dσ/dΩ (mb/sr)
10
0
^{27}Al (p, p_2)
5
0
^{27}Al (p, p_1)
20
0
^{27}Al (p, α_0)
1.7
1.8
1.9
2.0
2.1
2.2
2.3
2.4
E_p (MeV)

Figure 4.25 The differential cross sections for $^{27}Al(p,p)$, (p,p_1), (p,p_2), and (p,α_0) at 90^o in the energy range E_p = 2.42 to 3.05 MeV. The solid line is an R-matrix fit to the data.

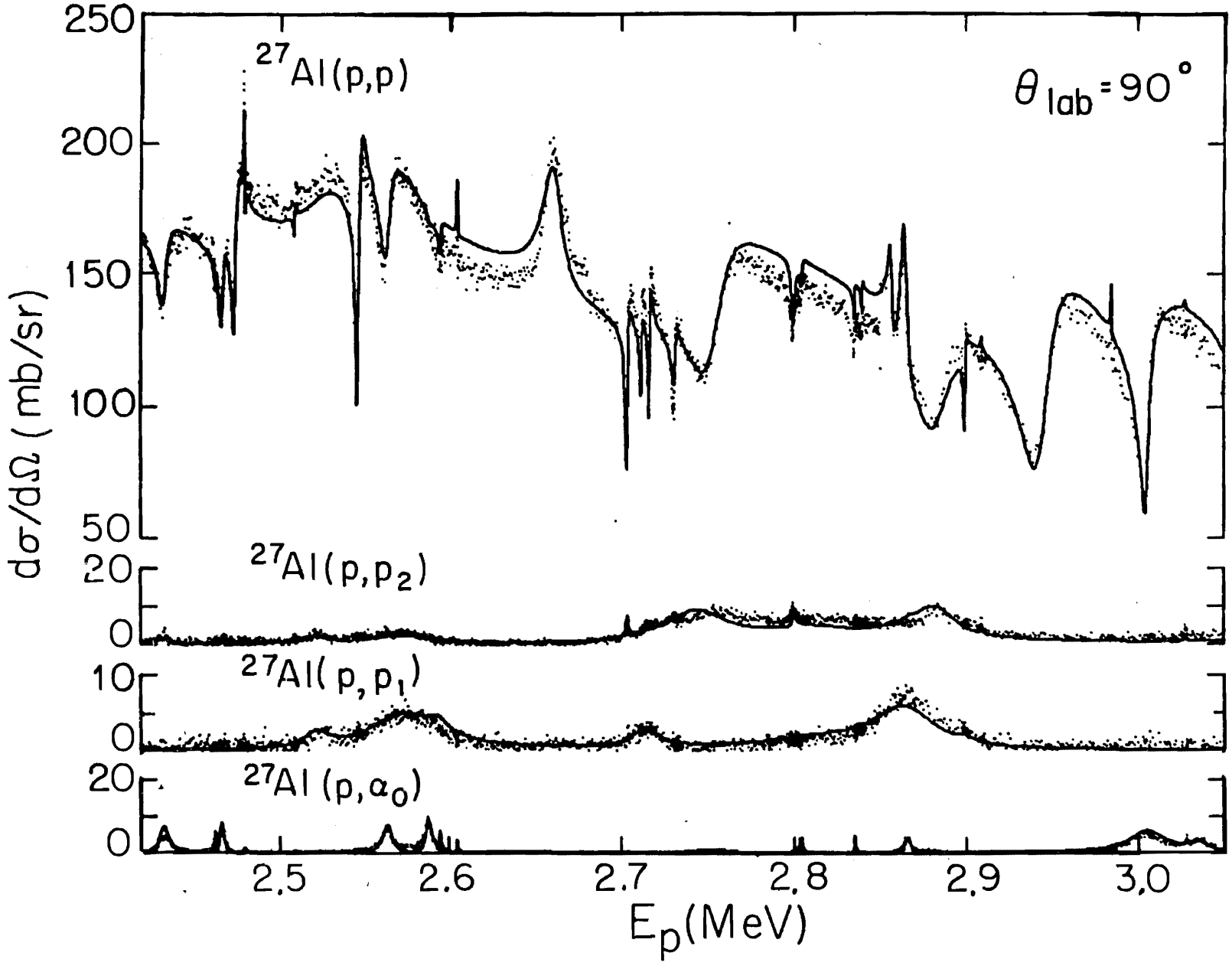
250
200
150
100
50
^{27}Al(p,p)
θ_{lab}=90°
dσ/dΩ (mb/sr)
20
0
^{27}Al(p,p$_2$)
10
0
^{27}Al(p,p$_1$)
20
0
^{27}Al (p,α$_0$)
2.5
2.6
2.7
2.8
2.9
3.0
E$_p$(MeV)

Figure 4.26 The differential cross sections for $^{27}Al(p,p)$, (p,p_1), (p,p_2), and (p,α_0), at 105^{o}, and (p,α_1) at 120^{o} in the energy range E_p = 2.42 to 3.05 MeV. The solid line is an R-matrix fit to the data.

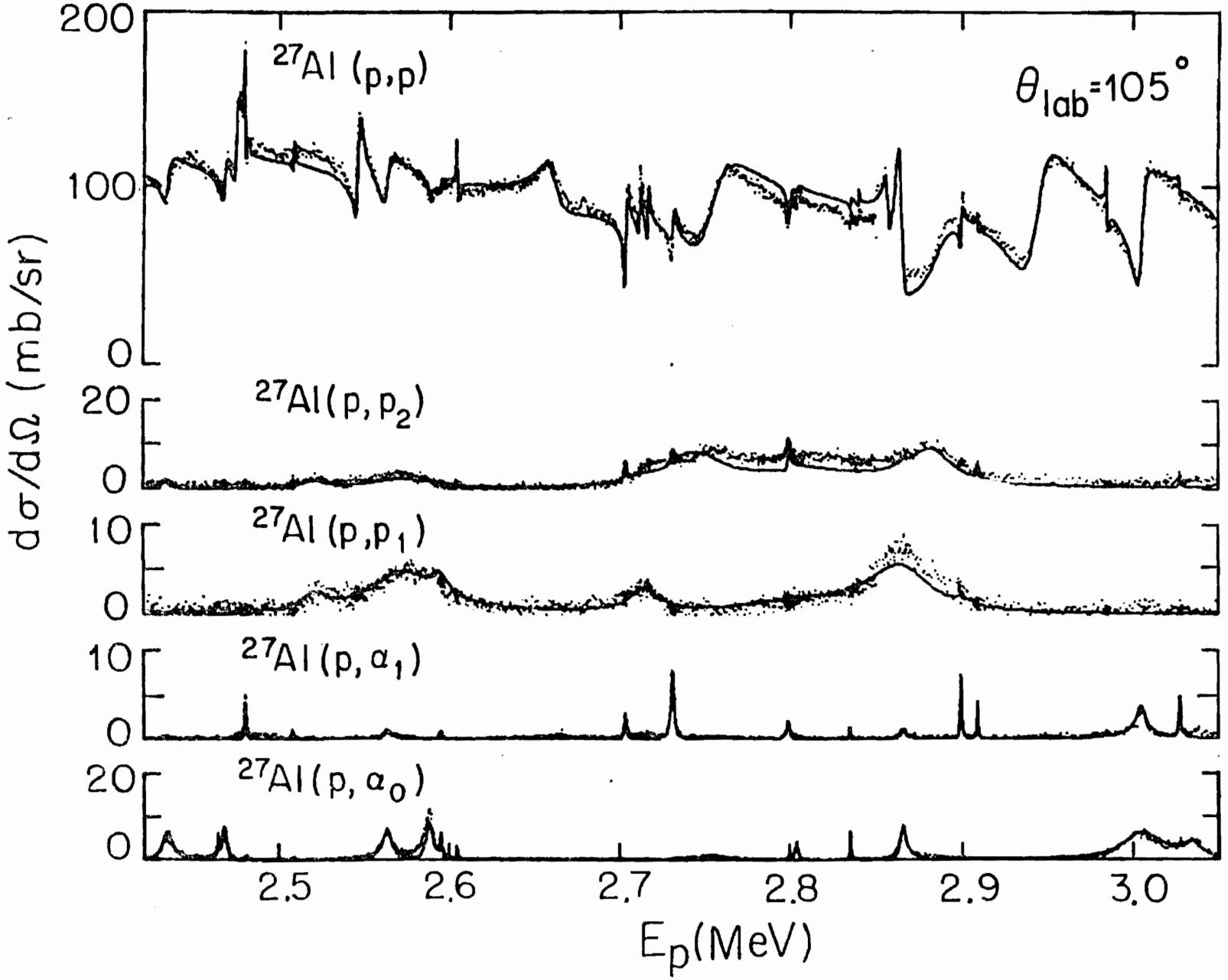
200
100
0
^{27}Al (p,p)
θ_{lab}=105°
20
0
^{27}Al(p, p$_2$)
10
0
^{27}Al (p,p$_1$)
10
0
^{27}Al (p, α_1)
20
0
^{27}Al(p, α_0)
dσ/dΩ (mb/sr)
2.5
2.6
2.7
2.8
2.9
3.0
E$_p$(MeV)

Figure 4.27 The differential cross sections for ^{27}Al(p,p), (p,p_1), (p,p_2), (p,α_0), and (p,α_1) at 135^{o} in the energy range E_p = 2.42 to 3.05 MeV. The solid line is an R-matrix fit to the data.

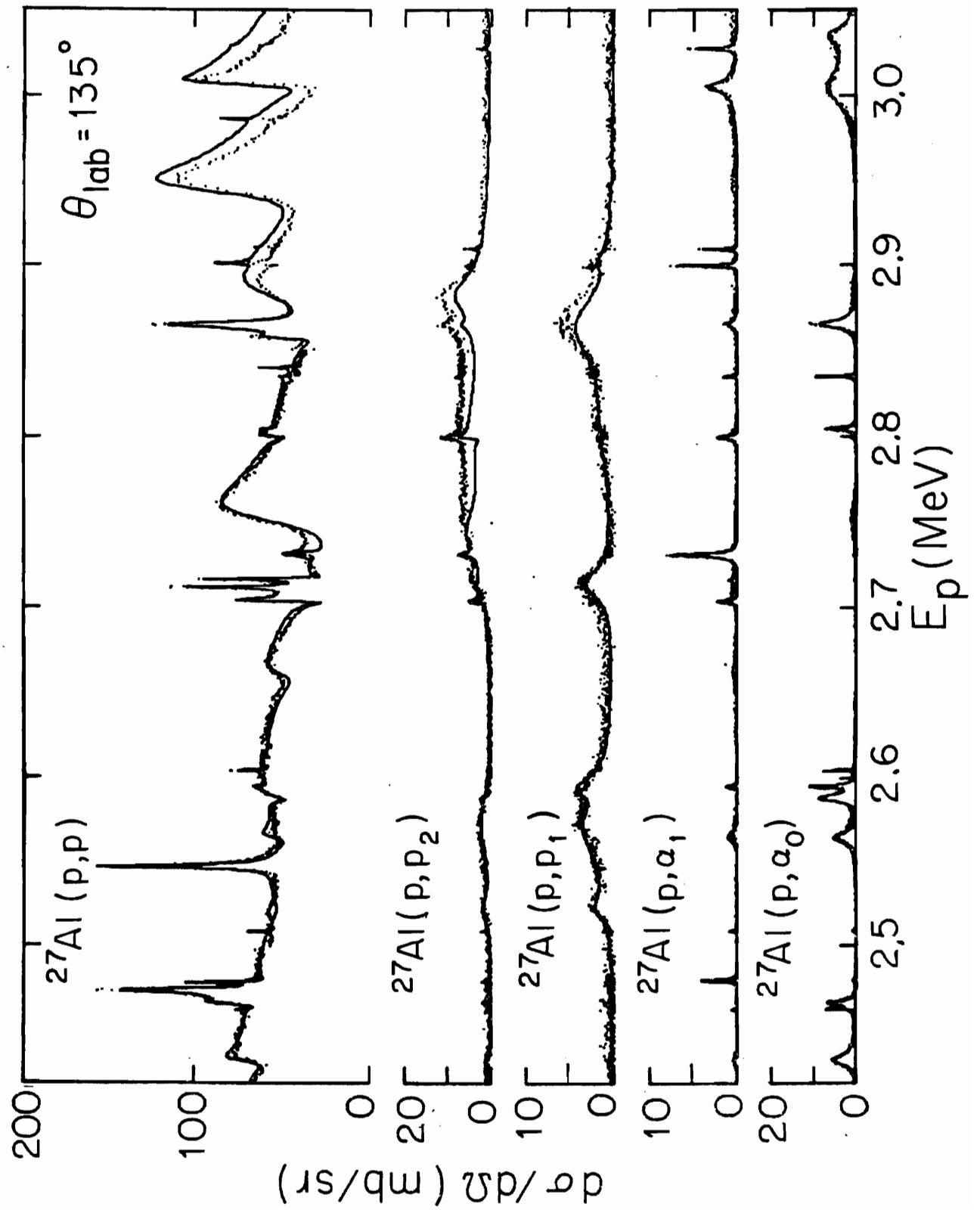
$\theta_{lab} = 135°$
$^{27}Al\,(p,p)$
$^{27}Al\,(p,p_2)$
$^{27}Al\,(p,p_1)$
$^{27}Al\,(p,\alpha_1)$
$^{27}Al\,(p,\alpha_0)$
200
100
0
20
0
10
0
10
0
20
0
2.5
2.6
2.7
2.8
2.9
3.0
E_p (MeV)
$d\sigma/d\Omega$ (mb/sr)

Figure 4.28 The differential cross sections for $^{27}Al(p,p)$, (p,p_1), (p,p_2), and (p,α_0) at 160°, and (p,α_1) at 150° in the energy range E_p = 2.42 to 3.05 MeV. The solid line is an R-matrix fit to the data.

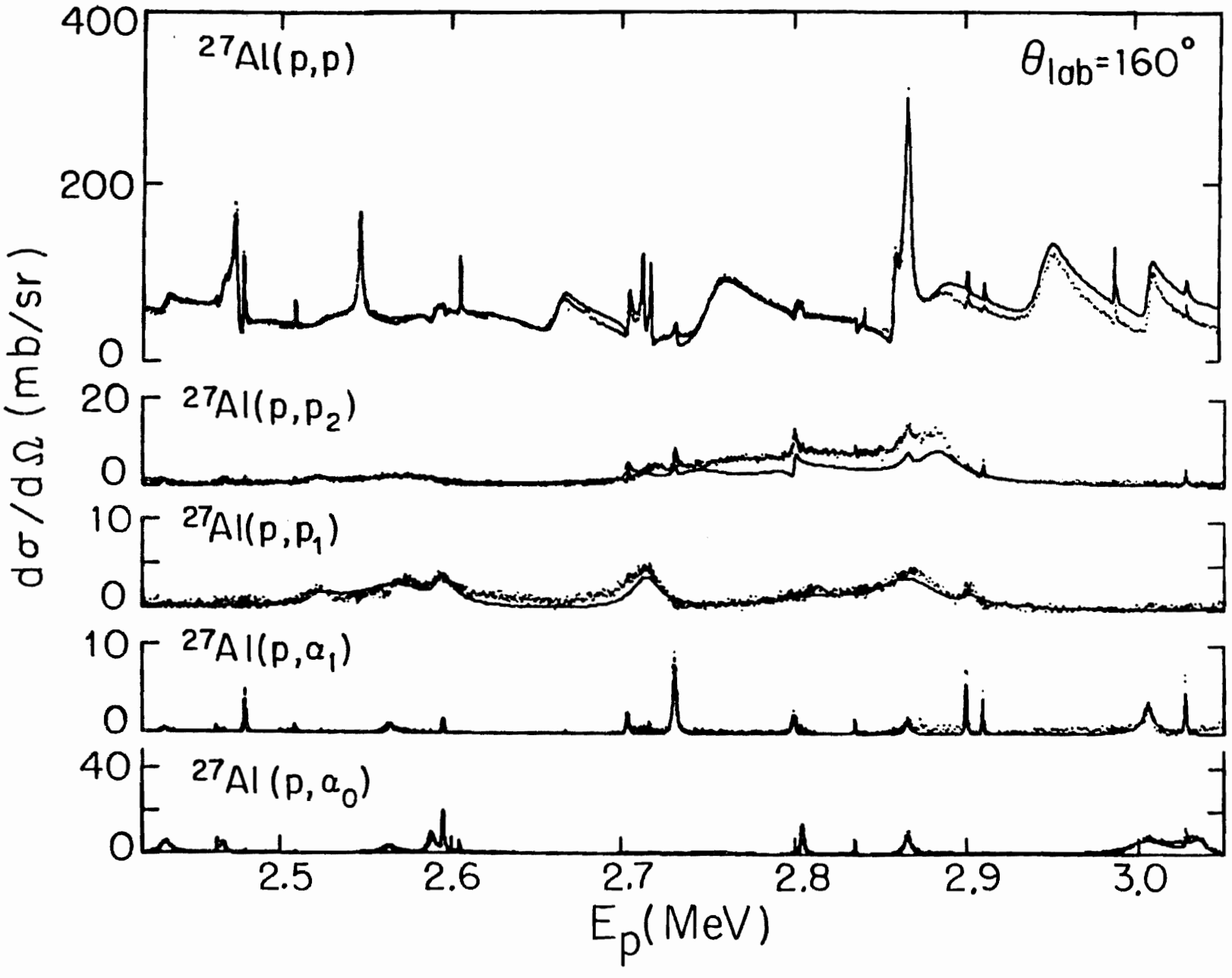
400
200
0
^{27}Al(p,p)
θ_{lab}=160°
20
0
^{27}Al(p,p$_2$)
10
0
^{27}Al(p,p$_1$)
10
0
^{27}Al(p,α_1)
40
0
^{27}Al(p,α_0)
dσ/dΩ (mb/sr)
2.5
2.6
2.7
2.8
2.9
3.0
E_p(MeV)

not be obtained for the cluster of resonances observed in the (p,p_2) reaction around $E_p = 2.8$ MeV. The lack of information about the spins, channel spin mixing ratios, energies, and total number of resonances which comprise this cluster, combined with the strong interference effects, made it impossible to determine the correct resonance parameters. However, most of the resonances observed in the elastic scattering and (p,α_0) cross sections could be assigned ℓ values and spins.

Above 2.9 MeV the poorer fits are probably due to the effects of higher energy resonances, although resonance parameters were included for a few of the large states observed from 3.05 - 3.30 MeV. In addition, the approximations made in the R-matrix analysis may begin to break down in this energy region which is near the top of the Coulomb barrier.

A portion of the data around the $J^\pi = 2^+$ resonance at $E_p = 1.365$ MeV is shown in figure 4.29. This resonance was utilized in a test of time reversal invariance and is discussed in chapter V. The large s-wave resonance at $E_p = 1.388$ MeV is actually a doublet which consists of a 3^+ level and a 2^+ level (with alpha decay) separated by 200 eV. There are five natural parity levels in this range, four of which exhibit alpha decay. These include a 4^+ d-wave resonance, two 2^+ resonances, and one 1^- level.

The 160° elastic scattering cross section for $E_p = 1.65 - 1.85$ MeV is shown in figure 4.30. This excitation function includes resonances with ℓ values from 0 to 3, and spins from 1 to 5. The resonances include: (1) two 2^+ s-wave states, (2) a 3^- level also observed in the (p,α) reaction, (3) a 5^- f-wave analog state, (4) a 2^- p-wave resonance, (5) a 4^- p-wave, 1^+ d-wave doublet, and (6) a 4^+ d-wave resonance.

Finally, the region around the 6^- stretched state at $E_p = 2.875$ MeV is shown in figure 4.31. The 6^- level is discussed in chapter V. The alpha decay to the ground state of ^{24}Mg is both parity and isospin forbidden for

Figure 4.29 The differential cross sections for $^{27}Al(p,p)$, and $^{27}Al(p,\alpha_0)$ at 160^o in the energy range E_p = 1.30 to 1.45 MeV. The solid line is an R-matrix fit to the data.

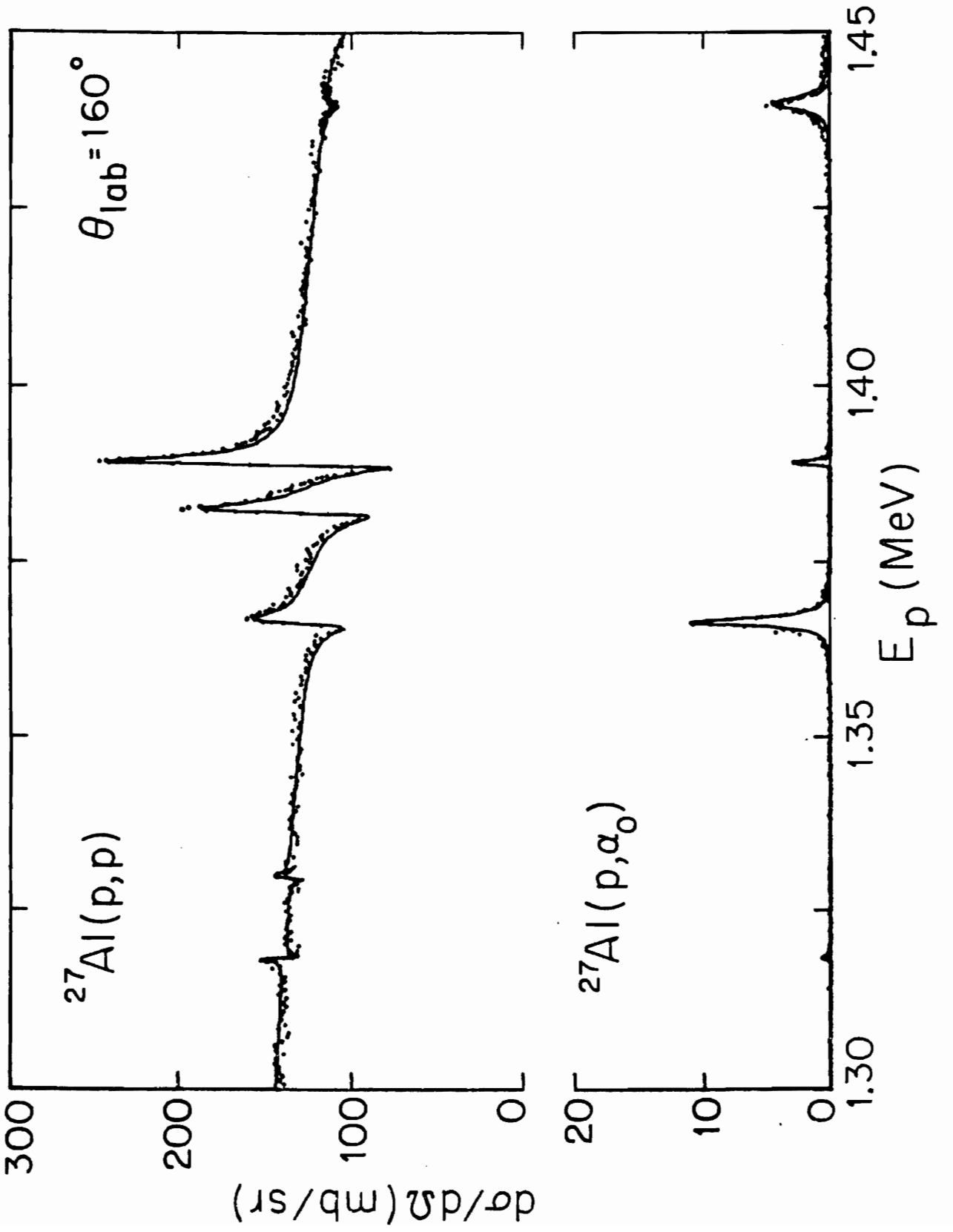
θ_{lab}=160°
^{27}Al(p,p)
^{27}Al(p,α_0)
dσ/dΩ (mb/sr)
E_p (MeV)
300
200
100
0
20
10
0
1.30
1.35
1.40
1.45

Figure 4.30 The differential cross section for $^{27}Al(p,p)$, at 160^{o} in the energy range E_p = 1.65 to 1.85 MeV. The solid line is an R-matrix fit to the data.

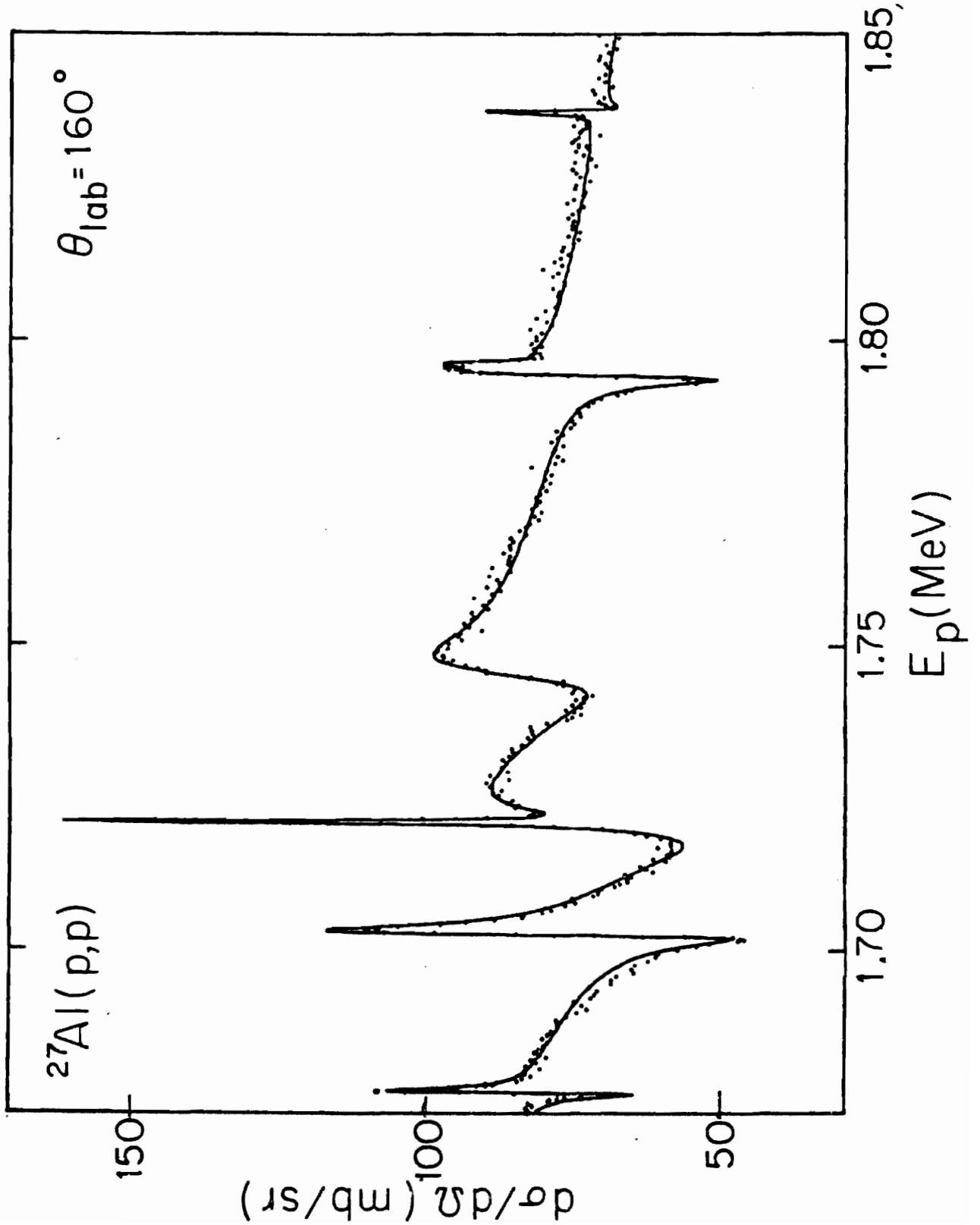
θ_{lab}=160°
^{27}Al(p,p)
dσ/dΩ (mb/sr)
150
100
50
1.70
1.75
1.80
1.85
E_p(MeV)

Figure 4.31 The differential cross sections at 160^{o} in the region of the 6^{-}, T = 1 stretched state at E_{p} = 2.875 MeV. The solid line is an R-matrix fit to the data.

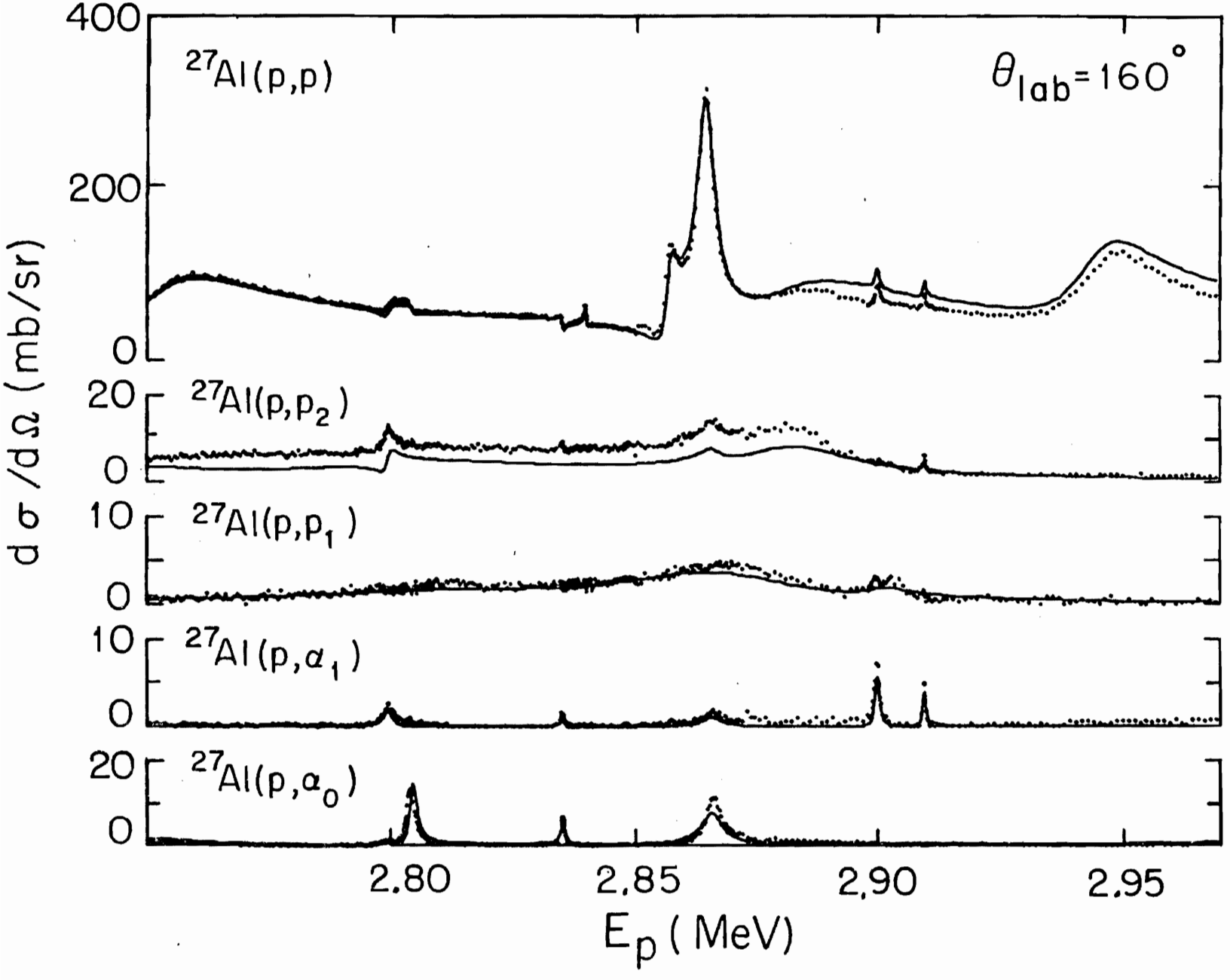
400
200
0
^{27}Al(p,p)
θ_{lab}=160°
20
0
^{27}Al(p,p$_2$)
10
0
^{27}Al(p,p$_1$)
10
0
^{27}Al(p,α_1)
20
0
^{27}Al(p,α_0)
dσ/dΩ (mb/sr)
2.80
2.85
2.90
2.95
E_p (MeV)

the 6^- state. The peak observed in the (p,α) and (p,p_2) cross sections near the 6^- state is located approximately 1 keV higher in energy and is due to a resonance with a probable spin of 3. There was no decay other than elastic scattering observed for the 6^- state.

CHAPTER V

ANALYSIS AND RESULTS

A. Analog States in ^{30}P and ^{28}Si

The concept of analog states arises from the charge independence of nuclear forces. Consider the addition of a nucleon to a core nucleus with atomic number Z, neutron number N, and mass number A. Suppose a bound state exists in the nucleus $_{Z}(A + 1)_{N + 1}$. This state is called the parent state and consists of a neutron plus the core. Changing one neutron into a proton results in a similar state in a nucleus (daughter nucleus) $_{Z+1}(A + 1)_{N}$. If nuclear forces are charge independent, the energy of the resulting state in the daughter nucleus differs from that in the parent nucleus only by the Coulomb energy (E_c) of the extra proton minus the neutron-proton mass difference (δ). The state in the daughter nucleus should have essentially the same properties as that of the parent state; this state is called the "analog" of the parent state. The energy relation between these states is shown in figure 5.1, where D represents the daughter nucleus and P represents the parent nucleus. T is the isospin quantum number with projection $T_z = (N - Z)/2$. In the daughter nucleus, states of both $T = T_z + 1/2$ and $T = T_z - 1/2$ are populated in proton resonance scattering.

Analog states have been extensively studied both experimentally and theoretically. In nuclei with very low level densities analogs occur as individual states. In nuclei with high level densities analogs are fragmented (mixed with the background states by the Coulomb interaction), and are normally strongly enhanced with respect to the background states.

Figure 5.1 Energy level diagram showing the relationship between the parent state and the analog state.

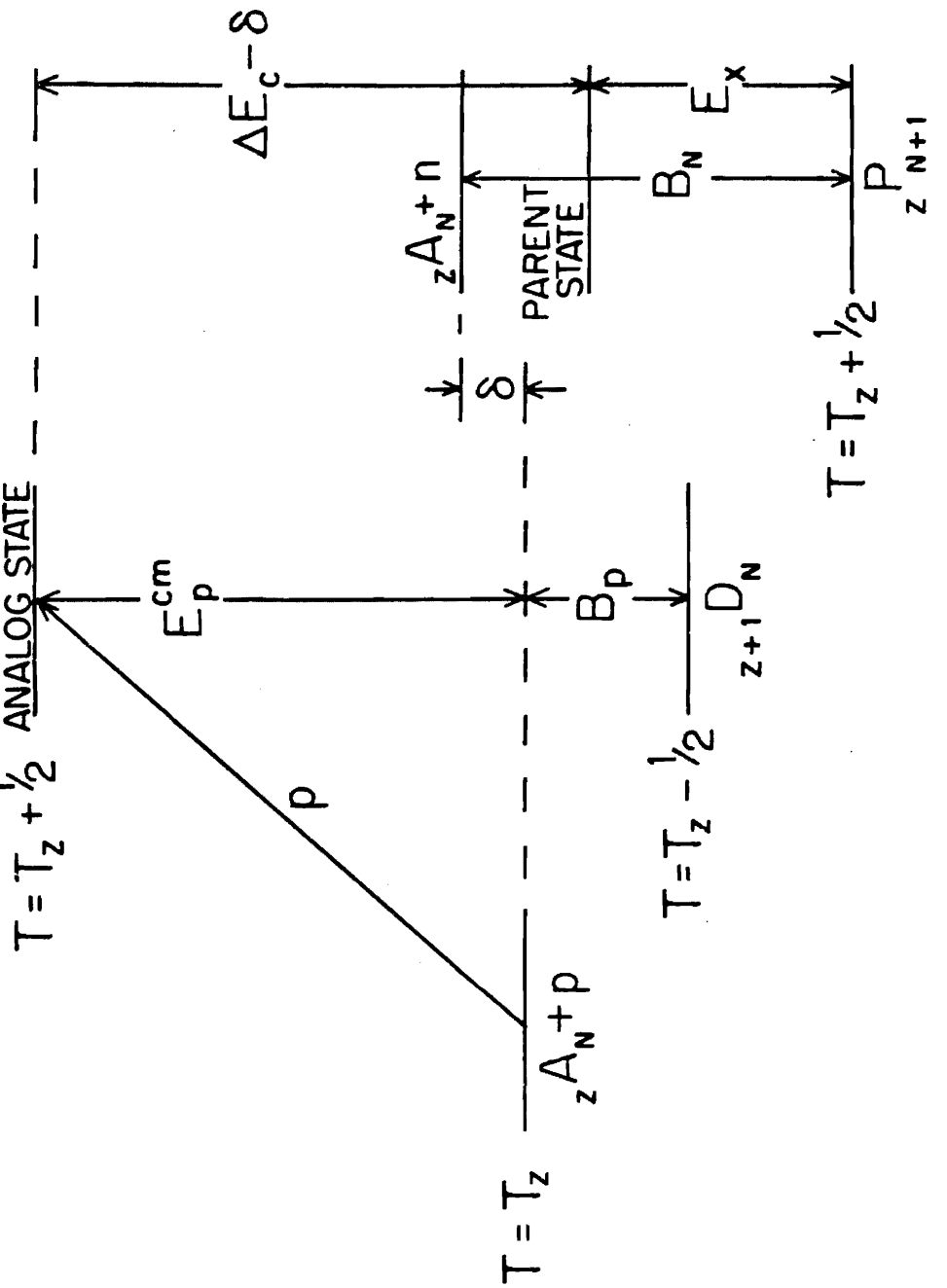
$\Delta E_c - \delta$
E_x
B_N
$P_{z^{N+1}}$
$T = T_z + 1/2$
$_zA_N + n$
PARENT STATE
δ
ANALOG STATE
E_p^{cm}
B_p
$D_{z+1}N$
$T = T_z - 1/2$
p
$T = T_z$
$_zA_N + p$

In both cases the analogs are easily identified in practice. However, there are intermediate situations where the analogs are not enhanced with respect to the background, and a unique identification of analog states becomes difficult or impossible. Some of the analogs in the present measurements appear to fall into this latter class. To aid in the discussion of analog identification the reduced widths for ^{30}P and ^{28}Si are plotted in figures 5.2 and 5.3.

The parent states may be observed in neutron stripping reactions such as the (d,p) reaction. The analogs may be excited in proton transfer reactions, such as (^{3}He,d), or as resonances in proton elastic scattering. From figure 5.1 the relation between the excitation energy (E_x) and the center of mass proton energy (E_p) is

$$\Delta E_c = B_n + E_p^{cm} - E_x$$

where B_n is the binding energy of the last neutron in the parent nucleus. From this relation and an estimate of the Coulomb energy, E_p can be approximately determined for the known parent levels. In addition, the relative strengths of the parent and analog state are expected to obey the relation

$$S_{dp} = (2T_z + 1)\Gamma_p / \Gamma_{sp} = (2T_z + 1)S_p$$

where S_{dp} is the (d,p) spectroscopic factor, S_p is the proton spectroscopic factor, and Γ_{sp} is the single particle width of the resonance. A discussion of Coulomb energies and spectroscopic factors as applied to this mass and energy region is given by Outlaw (1974). Often identification of analog states is easy, however for the intermediate case mentioned above, the identification process is not simple. Quantitative strength comparisons are not meaningful when the analog strength is mixed with one or two strong background states.

States observed in proton elastic scattering may be identified as

Figure 5.2 Reduced widths versus energy for resonances in ^{30}P. The prominent analog states are the 4^- resonance near $E_p = 1.5$ MeV, and the 0^+ and 2^- resonances near $E_p = 1.67$ MeV.

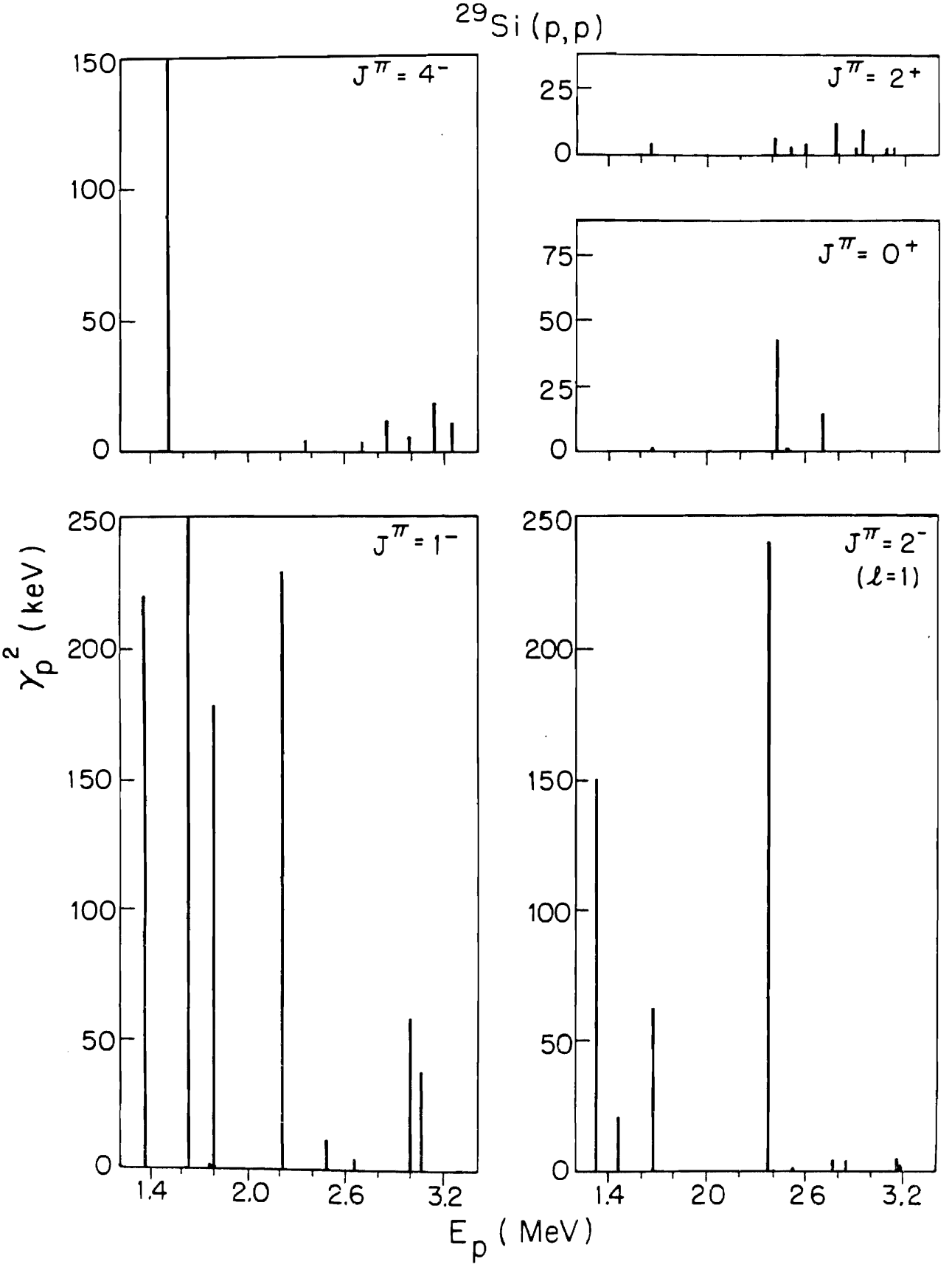
^{29}Si (p,p)
$J^\pi = 4^-$
$J^\pi = 2^+$
$J^\pi = 0^+$
$J^\pi = 1^-$
$J^\pi = 2^-$
(ℓ=1)
γ_p^2 (keV)
E_p (MeV)
150
100
50
0
25
75
250
200
1.4
2.0
2.6
3.2
20
26

Figure 5.3 Reduced widths versus energy for resonances in ^{28}Si. In the plots with multiple J values listed the unmarked resonances have J = 4. The prominent analog states are: (1) the 2^+ resonance at E_p = 1.025 MeV, (2) the 3^- level at E_p = 1.200 MeV, (3) the 5^- resonance at E_p = 1.724 MeV, (4) the 1^+ state at E_p = 1.800 MeV, and (5) the 6^- stretched state at E_p = 2.875 MeV.

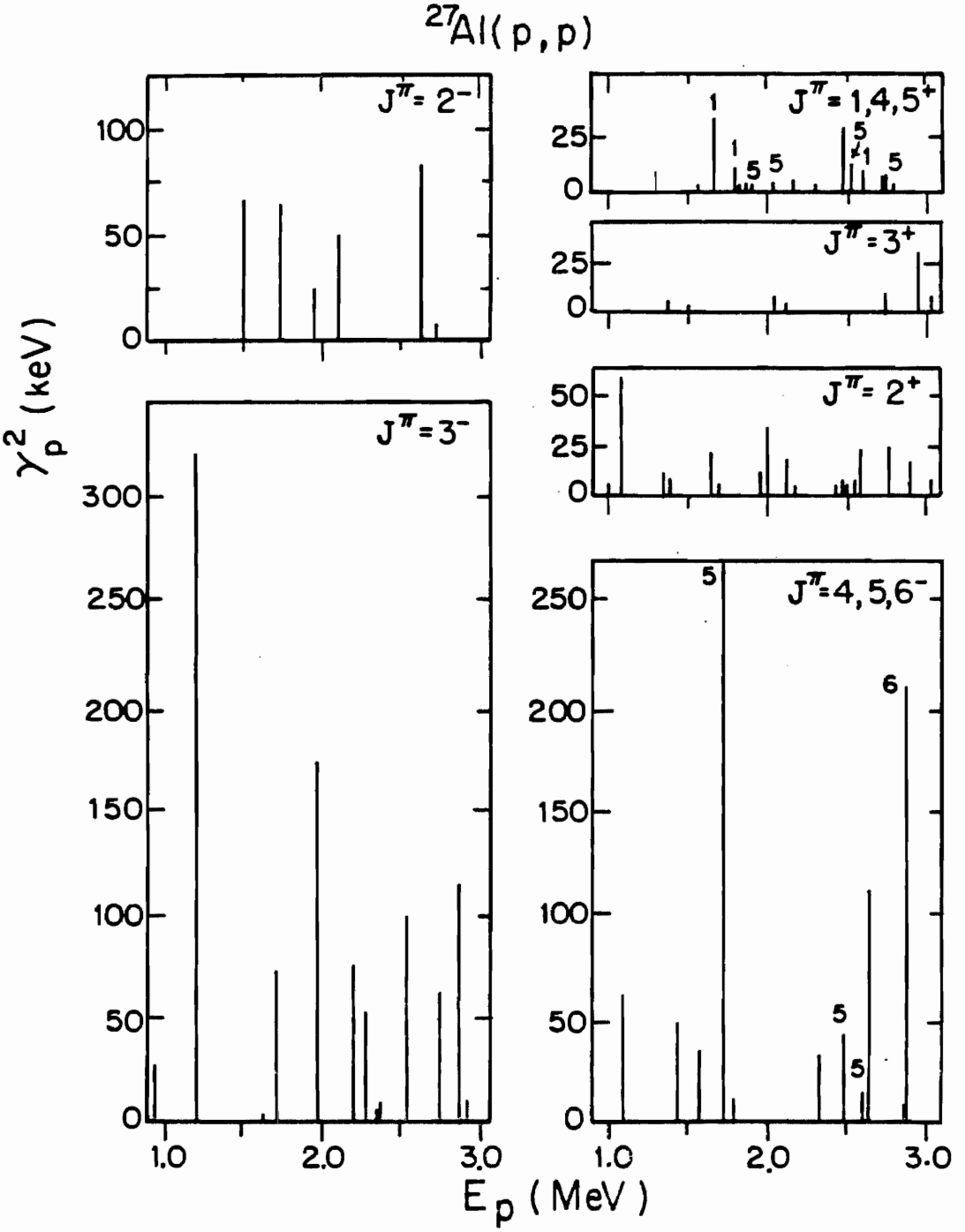
^{27}Al(p,p)
$J^\pi = 2^-$
$J^\pi = 1,4,5^+$
$J^\pi = 3^+$
$J^\pi = 2^+$
$J^\pi = 3^-$
$J^\pi = 4,5,6^-$
γ_p^2 (keV)
E_p (MeV)

analogs on the basis of angular momentum, energy, and strength. These quantities are tabulated for ^{30}P and ^{28}Si in tables 5.1 and 5.2. The single particle widths were calculated following the approach of Harney and Weidenmüller (1969). The method consists of calculating the excitation energy of a state consisting of a neutron (with the correct orbital and total angular momenta) in a real Woods-Saxon type potential while varying the potential well depth until the excitation energy of the parent state is matched. A symmetry potential

$$U_{sym} = \left[(2T_0 + 1)\right](125/A) \text{ MeV}$$

is then added to the neutron well depth to simulate the proton potential. The single particle proton width is then calculated with these potential well parameters.

For targets with spin several complications arise in calculating the single particle widths. For ℓ values other than zero, two total angular momentum values may contribute (except in the case of the maximum and minimum values of the resonance spin). The resonance analysis usually leads to two possible solutions for the relative j contribution. Thus the values of j to be used in the analysis are not well determined. The presence of ℓ-mixing also complicates the analysis since the single particle width must be calculated separately for the contribution due to each ℓ value. An extra complication occurs for $\ell = 1$ resonances because both 1p-hole states and 2p-particle states may be populated in 2s-1d shell nuclei, and thus the value of the principal quantum number to be used in the analysis is uncertain. The values of the single particle widths were found to be rather insensitive to the j value. Similarly, the choice of the principal quantum number (n) for p-wave resonances was not critical. An average over all possible values of j and n was used to obtain the single particle widths.

For ^{30}P seven analog states were tentatively identified. Five of these

TABLE 5.1

ANALOG STATE PARAMETERS IN ^{30}P.

J^π	E_x[a] (MeV)	ℓ	E_p^{lab}[b] (MeV)	E_c (MeV)	Γ_{sp}[b] (keV)	Γ_p (keV)	S_p	S_{dp}[c]
4^-	6.503	3	1.506	5.566	0.21	0.045	0.43	0.43
2^+	6.537	2	1.664	5.682	2.9	0.030	0.01	
0^+	6.641	0	1.669	5.582	59.	0.16	0.003	
2^-	6.641	1	1.684	5.597	54.	4.5	0.17	0.09
1^-	6.744	1	1.788	5.594	50.	16.5	0.66	0.33
2^-	7.508	1	2.377	5.400	230.	70.	0.61	0.34
1^-	8.163	1	3.025	5.352	476.	62.	0.26	0.23

[a]Excitation energies in ^{30}Si from Endt and Van der Leun (1978).

[b]Values of Γ_{sp} are averaged over n = 1 and 2 for J = 2, and also over j = 1/2 and 3/2 for J = 1.

[c]Spectroscopic factors from Endt and Van der Leun (1978).

TABLE 5.2

ANALOG STATE PARAMETERS IN ^{28}Si.

J^π	E_x[a] (MeV)	ℓ	E_p^{lab}[a,b] (MeV)	E_c (MeV)	Γ_{sp}[b] (keV)	Γ_p (keV)	S_p	S_{dp}[c]
3^+	3.30	0 2	0.992	5.382	8.	0.10	0.012	0.02 0.04
2^+	3.35	0 2	1.025	5.364	10.	0.11	0.011	0.022 0.022
4^-	3.47	1 3	1.118	5.333	4.5	0.70	0.16	0.11 0.62
3^-	3.59	1 3	1.200	5.292	7.	5.4	0.77	0.19 0.60
3^+	3.67	0 2	1.388	5.393	40.	0.60	0.015	0.006 0.019
2^+	3.71	0 2	1.381	5.347	40.	0.78	0.02	0.04 0.076
2^-	3.88	1 3	1.517	5.308	20.	3.7	0.18	0.074 0.28
1^+	3.90	2	1.662	5.428	4.	0.40	0.10	0.05
2^+	3.94	0 2	1.660	5.386	85. 4.0	1.7 0.15	0.02 0.04	0.012 0.04
5^-	4.03	3	1.724	5.358	0.3	0.25	0.82	0.85
1^+	4.12	2	1.800	5.341	6.	0.20	0.03	0.057
4^+	4.46	2	2.159	5.347	15.	0.17	0.01	0.033
4^+	4.74	2	2.483	5.379	30.	2.4	0.08	0.062
1^+	4.85	2	2.603	5.385	35.	1.0	0.028	0.10

TABLE 5.2-Continued

J^π	E_x[a] (MeV)	ℓ	E_p^{lab} (MeV)	E_c (MeV)	Γ_{sp}[b] (keV)	Γ_p (keV)	S_p	S_{dp}[c]
2^-	4.91	1 3	2.583	5.306	160.	36.	0.23	0.24 0.06
2^+	5.00	0 2	2.762	5.388	300.	25.	0.08	0.0 0.11
3^+	5.02	0 2	2.713	5.321	300.	0.80	0.003	0.006 0.009
6^-	5.17	3	2.875	5.328	6.	3.7	0.58	

[a]Excitation energies in ^{28}Al from Endt and Van der Leun (1978).

[b]Values of Γ_{sp} are averages, see text for discussion.

[c]Spectroscopic factors from Endt and Van der Leun (1978).

states were previously listed by Endt (1978) as possible analog states. The excitation energies of the parent states are higher than for most previous analog states studied. There are four other states which are weakly excited in the (d,p) reaction for which definite assignments could not be made. The strong 4^- analog at E_p = 1.506 MeV and the 0^+ and 2^- analogs near 1.67 MeV appear as prominent states in figure 5.2. The reduced width plots provide little help in identification of the other analogs.

While most of the parameters listed in table 5.1 are in good agreement with the (d,p) results, three of the states have proton spectroscopic factors which are larger than the (d,p) spectroscopic factors. This is unusual since for 1f-2p shell nuclei S_p was systematically lower than S_{dp}. However, values of S_p greater than S_{dp} have been observed previously in 2s-1d shell nuclei (Outlaw 1974; Westerfeldt 1977).

Analogs have been tentatively identified for 18 of the 25 states observed in the ^{27}Al(d,p) reaction. For a few of the parent states several possibilities exist for the analog but no assignments could be made. Nine previous analog assignments are listed by Endt (1978). The present results agree with those assignments except that the 2^+ state at E_x = 3.71 MeV may have two fragments, with most of the strength in the lower energy resonance at E_p = 1.381 MeV. Nine new assignments have been made in the present work. Many of these states are weakly excited with only six states having S_{dp} greater than 0.1. Five analogs are prominent in the reduced width plots of figure 5.3: (1) the 2^+ resonance at E_p = 1.025 MeV, (2) the 3^- level at E_p = 1.200 MeV, (3) the 5^- resonance at E_p = 1.724 MeV, (4) the 1^+ state at E_p = 1.800 MeV, and (5) the 6^- stretched state at E_p = 2.875 MeV.

The alpha decay of a T = 1 state (such as an analog) to a T = 0 final state in ^{24}Mg is forbidden by conservation of isospin. Thus, strong α_0 of a resonance decay indicates T = 0. This information ruled out the assignment

of several resonances as analog states.

The spectroscopic factors for ^{28}Si follow the usual trend— no strong analog states have spectroscopic factors greater than the (d,p) spectroscopic factors.

Most of the ℓ values assigned in the (d,p) and (p,p) reactions were in reasonable agreement. For two strong resonances (E_x = 3.59 and 5.00 MeV) there was disagreement for the ℓ-mixture, although the total strengths agree. This discrepancy may be due to errors in the stripping analysis, or the analog identification may be incorrect.

B. The $J^\pi = 6^-$, T=1, Stretched State at E_x = 14.36 MeV in ^{28}Si.

A stretched particle-hole state is defined within the context of a harmonic oscillator shell model as a nuclear state in which a single particle occupies an orbit of the largest angular momentum j_a in a given oscillator shell N, and a single hole occupies the orbit of largest angular momentum j_b, in the next lower shell N − 1, with j_a and j_b coupled to give the largest value of total angular momentum. N is the oscillator shell number and j_n is the total angular momentum of the particle n. Such states are predicted to occur at excitation energies $\hbar\omega = (41/A^{1/3})$ MeV (Lindgren 1979), where A is the atomic mass number. These states are of interest because they are strongly excited in intermediate energy proton, electron, and pion inelastic scattering. In addition, due to the relatively simple structure of these states, it may be possible to describe the reactions well in terms of a simple model.

Stretched $J^\pi = 4^-$ states of the configuration $(d_{5/2}p_{3/2}^{-1})$ have been observed in ^{12}C and ^{16}O, $J^\pi = 6^-$ states with the form $(f_{7/2}d_{5/2}^{-1})$ are known in ^{24}Mg and ^{28}Si, and $J^\pi = 8^-$ states, with the structure $(g_{9/2}f_{7/2}^{-1})$ have been seen in ^{54}Fe, ^{58}Ni, and ^{60}Ni (Lindgren 1979). The interpretation and

understanding of the intermediate energy scattering data depends upon a knowledge of the reaction mechanism and the use of a reasonable model for comparison with the data. For the $J^{\pi} = 6^{-}$ stretched state at $E_x = 14.36$ MeV in ^{28}Si, the spectroscopic strengths from inelastic proton, pion, and electron inelastic scattering are all in good agreement. It is important to be able to compare information from low energy excitation of this state with the intermediate energy results to examine the assumptions made in analyzing the inelastic scattering data. The measurement of the width of this stretched state in ^{28}Si through low energy elastic scattering provides such a test.

First a brief explanation of the intermediate energy results will be given, and then the relation between the measured width and the intermediate energy results will be derived. In addition, some more recent results on this state will be discussed.

Following Halderson (1981), assume that the ^{28}Si ground state $|i\rangle$ is a closed $0d_{5/2}$ shell plus a more complicated component

$$|i\rangle = \alpha_1|0\rangle + \alpha_2|c_i\rangle\,,\ \alpha_1^2 + \alpha_2^2 = 1\ ,$$

The $J^{\pi} = 6^{-}$, $T = 1$ state is similarly described as a pure particle hole excitation plus a more complicated component

$$|f\rangle = \beta_1[a^{+}_{f_{7/2}}, a_{d_{5/2}}]^{6,1}|0\rangle + \beta_2|c_f\rangle\,,\ \beta_1^2 + \beta_2^2 = 1\ .$$

The excitation of the stretched state in inelastic scattering is expected to proceed predominantly through a single particle transition. If the transition $|0\rangle \rightarrow [a^{+},a]^{6,1}|0\rangle$ between pure states is declared a sum rule then the fraction of the sum rule exhausted by the transition gives a measure of $\alpha_1^2\beta_1^2 \equiv S_{ph}^2$. For the state at $E_x = 14.36$ MeV in ^{28}Si the inelastic scattering data for protons, pions, and electrons agree remarkably

well with the average value of $S^2_{ph} = 0.31$.

Since the resonance scattering proceeds from the ^{27}Al ground state to the $J^\pi = 6^-$ state, while inelastic reactions promote a particle from the ground state of ^{28}Si, the structure of the two ground states must be related to compare the results of the two modes of excitation. The spectroscopic strength for the ^{27}Al(^{3}He, d) stripping reaction to the ^{28}Si ground state is 0.44. With the naive assumption that the ^{27}Al ground state consists of a ^{28}Si ground state core with a $d_{5/2}$ hole, the stripping data account for only 44% of the calculated strength. This is a large departure from the single particle shell model. If S^2_{ph} equals 0.31, then the $J^\pi = 6^-$ resonance must be a fairly pure single particle state with a proton spectroscopic factor, $S_p = 0.31/0.44 = 0.70$.

The width of the $J^\pi = 6^-$ resonance located at $E_p = 2.876$ MeV was determined in the present experiment to be $\Gamma_p = 3.7 \pm 0.3$ keV. This value is in reasonable agreement with the width, $\Gamma_p = 4.0 \pm 0.2$, determined from the (p,γ) reaction (Snover 1983). The single particle fraction may be determined from this width by using a Woods-Saxon potential to calculate the width of a single particle state of the proper spin and excitation energy. Halderson performed such a calculation and obtained the value $\Gamma_{sp} = 5.4$ keV. This yields a single particle fraction $\Gamma_p/\Gamma_{sp} = 3.7/5.4 = 0.68 \pm 0.07$, in agreement with the value obtained from the (^{3}He, d) results and S^2_{ph}. Snover, on the other hand, calculated the single particle width for the $J^\pi = 6^-$ state using the potential well parameters employed in a DWBA analysis of ^{27}Al(^{3}He, d)^{28}Si stripping to the $J^\pi = 6^-$ state. A range of possible values for the single particle width were calculated by Snover; $6.7 < \Gamma_{sp} < 8.9$ keV, all of which are higher than the value obtained by Halderson. Our analog state calculation yields an estimate of 6.4 keV for Γ_{sp}.

Using Snover's values for the single particle width the single particle

fraction is 0.49 ± 0.08. A more detailed analysis was performed by Snover in which the fractionation of the $d_{5/2}$ pickup strength to $J^{\pi} = 5/2^{+}$ levels other than the ground state of ^{27}Al was accounted for, and a more recent value of the mass 27 ground state stripping spectroscopic factor was employed. In Snover's analysis the spectroscopic strengths of the low energy and intermediate energy data do not agree quantitatively, and the independent verification of the assumptions made in the intermediate energy inelastic scattering is only qualitatively successful.

It is important to try to obtain similar low energy data on other stretched states so that more comparisons can be made. Unfortunately this is difficult with proton elastic scattering. Excluding ^{27}Al, ^{11}B and ^{59}Co are the only stable targets for which the ground state spin is large enough to form the stretched state, and for which the Coulomb barrier is not extremely high. In both cases the stretched state resonances are located over one MeV above the (p,n) threshold so that neutron decay may be significant. In addition, the observed broad resonances in ^{11}B(p,p) would make determination of the width of the stretched state difficult. The $J^{\pi} = 8^{-}$ states should show up as $\ell = 4$ resonances in ^{59}Co(p,p). An attempt was made to locate these states, but no resonance structure was observed for the regions $E_p = 3.03 - 3.07$ MeV or $4.47 - 4.53$ MeV, where the two strongest stretched states in ^{60}Ni should be located.

C. Entrance Channel ℓ-Mixing for a 2^{+} Resonance in ^{28}Si

At present the only evidence for the violation of time reversal invariance (TRI) at the subatomic level is in the two observed decay modes of the neutral K particle. The amplitude of the T-odd decay relative to the T-even decay is 2×10^{-3}. To date, the underlying physical cause of this violation of TRI has not been determined. Many different types of

experiments may be performed to test the time reversal invariance of the different interactions. One test (Pearson 1975) which had been overlooked until recently was the study of detailed balance for an isolated resonance in low energy nuclear reactions.

A test of detailed balance was performed utilizing the $^{27}Al(p,\alpha)^{24}Mg$ reaction and its inverse (Driller 1979). The implications of this experiment for the violation of time reversal invariance depend upon the value of the mixing ratio of two partial waves. Driller et al. assumed a value of this mixing ratio in order to interpret their experimental results. Since the ratio is crucial for the analysis of this experiment, an accurate determination of the (-mixing ratio seemed worthwhile. First the theory will be briefly summarized, followed by a description of the experiments.

For nuclear reactions proceeding via an isolated resonance it is well known that the angle integrated cross sections automatically satisfy detailed balance independent of the time reversal invariance of nuclear forces. Following Pearson (1975) it can be shown, that for the differential cross sections, a test of time reversal invariance is possible with an isolated resonance. The deviation from detailed balance will be measured by the asymmetry parameter

$$\Delta = k_\alpha^2 \frac{d\sigma_{\alpha\alpha'}}{d\Omega}(\theta) - k_{\alpha'}^2 \frac{d\sigma_{\alpha'\alpha}}{d\Omega}(\theta) = C^L P_L(\theta)$$

where

$$C^L = \sum_{J_1 J_2 c_1 c_2 c_1' c_2'} b^L_{J_1 J_2 c_1 c_2 c_1' c_2'} \cdot \mathrm{Re}\left(U^{J_1}_{c_1' c_1} U^{J_2 *}_{c_2' c_2} - U^{J_1}_{c_1 c_1'} U^{J_2 *}_{c_2 c_2'}\right) \qquad 5.1$$

and

$$b^{L}_{J_1 J_2 c_1 c_2 c_1' c_2'} = \frac{1}{4}\,(-)^{s-s'}\,\bar{Z}(\ell_1 J_1 \ell_2 J_2; sL)\,\bar{Z}(\ell_1' J_1 \ell_2' J_2; s'L).$$

Except where noted the notation is the same as that in chapter 2.

According to Lane and Thomas (1958) the γ_c are real if time reversal invariance holds. If one assumes the form $\gamma_c = |\gamma_c| \exp(i\xi_c)$, then the phase angles ξ_c will be a measure of the violation of time reversal invariance. Substituting the single level collision matrix elements with the phases ξ included into eqn. 5.1 the result is

$$C^{L} = \frac{2}{(E_o - E)^2 + (\Gamma_o/2)^2} \sum_{c_1 c_2 c_1' c_2'} b^{L}_{J_1 J_2 c_1 c_2 c_1' c_2'}$$
$$\cdot \left|\Gamma^{1/2}_{c_1} \Gamma^{1/2}_{c_1'} \Gamma^{1/2}_{c_2} \Gamma^{1/2}_{c_2'}\right| \sin(\bar{\phi}_{c_1} + \bar{\rho}_{c_1'} - \bar{\rho}_{c_2} - \bar{\rho}_{c_2'})$$
$$\cdot \sin(\xi_{c_1} - \xi_{c_2} + \xi_{c_2'} - \xi_{c_1'}),$$

where the $\bar{\rho}$ include the usual Coulomb and hard sphere phase shifts.

In general, there is no reason why the phase angles ξ_c for the different subchannels should be equal. Thus, C^L will be non-zero if there is a violation of time reversal invariance. Since the phases $\bar{\phi}_c$ are independent of the channel spin, C^L will vanish unless two different ℓ values contribute to the entrance or exit channel. Because the two ℓ values must have the same parity, the spin of the resonance must be at least $J = 1$, and the minimum value of the either the entrance or exit channel spin must be $s = 1$.

Since $L = 0$ is the only multipole that survives angle averaging, the result that the angle integrated cross section automatically satisfies detailed balance is obtained by noting that the $\bar{Z}$ coefficients for $L = 0$ vanish unless $\ell_1 = \ell_2$ and $\ell_1' = \ell_2'$. All of the above results also apply in the case of overlapping (partially or completely) resonances provided none

have the same spin and parity.

In their test of detailed balance, Driller et al. (1979) used the $J^{\pi} = 2^{+}$, $E_x = 12.901$ MeV resonance in ^{28}Si through the $^{27}Al(p,\alpha)^{24}Mg$ reaction and its inverse. For this resonance the possible ℓ values are $\ell = 0$, 2, and 4. Due to the extremely small penetrabilities the $\ell = 4$ partial waves may be neglected. Since the exit channel spin is zero, $\ell_1' = \ell_2' = J$, and there is only one exit channel. In the entrance channel there are three possible channels $s = 2$ with $\ell = 0$ or 2, and $s = 3$ with $\ell = 2$. Since coherent interference occurs only between the $s = 2$ scattering amplitudes, these restrictions greatly simplify the analysis.

It is easier to accurately measure a relative cross section than an absolute cross section. In this experiment a $J^{\pi} = 1^{-}$ resonance, for which ℓ-mixing should be negligible, was employed to compare the relative cross sections of the two reactions. In this case the asymmetry parameter $\bar{\Delta}$ is defined in terms of relative instead of absolute cross sections. Driller et al. obtain the result

$$\bar{\Delta} = -4\left[10\,\Gamma_{22}/7\,\Gamma_{20}\right]^{1/2}\sin(\bar{\varphi}_0 - \bar{\rho}_2)\sin(\xi_0 - \xi_2) \ .$$

From this equation it is clear that the magnitude of any possible asymmetry is proportional to $\varepsilon_2 = \left[\Gamma_{22}/\Gamma_{20}\right]^{1/2}$. Since there was no experimentally determined value of ε_2 it was assumed that $\varepsilon_2^2 = 0.01$, approximately the ratio of the penetrabilities for $\ell = 2$ to $\ell = 0$. With $\varepsilon_2 = 0.1$ the experimentally measured value of the asymmetry parameter ($\bar{\Delta} = 0.0025 \pm 0.0192$) yields a difference in the TRI violating phases $\xi_{p0} - \xi_{p2} = 0.3^{\circ} \pm 3.0^{\circ}$. While this result is consistent with TRI, the sensitivity of the result to any possible TRI violation depends on the actual value of ε_2. For example, if ε_2 were extremely small, then the results of the experiment

would be very insensitive to a TRI violating phase difference. If, on the other hand, ε_2 turned out to have a much larger value than that assumed, then the results would be much more sensitive to any TRI violating phase difference.

To obtain an accurate determination of ε_2 the alpha angular distribution and the elastic scattering excitation functions are required. This method also provides the magnitude of ε_3; a polarization measurement is required to obtain the sign of ε_3. The angular distribution was measured with silicon surface barrier detectors at five laboratory angles: 90°, 120°, 135°, 150°, and 160°. The measured 90° spectrum is shown in figure 5.4. The presence of an uneven background in the spectrum from pileup of elastic scattering pulses was the major difficulty encountered in measuring the angular distribution well. In addition, the small $^{19}F(p,\alpha_2)$ peak partially overlapped the $^{27}Al(p,\alpha_0)$ peak at 160°. The pileup was reduced to a negligible amount by using pulse pileup rejection electronics and also by reducing the beam current and thus the counting rate.

The data were fit to a Legendre polynomial expression of the form

$$W(\theta) \propto 1 + a_2 P_2 + a_4 P_4 \ .$$

The data and fit are shown in figure 5.5. The 2% error bars represent the 1% error in counting statistics and an estimated error from the small background and other uncertainties. The extracted normalized Legendre coefficients are $a_2 = -0.08 \pm 0.02$ and $a_4 = 0.00 \pm 0.02$.

The Legendre coefficients of the angular distribution for the $^{27}Al(p,\alpha_0)$ reaction for a $J^\pi = 2^+$ excited state were calculated using the computer program CORR (Wells 1978). The resulting expressions for the a coefficients are

Figure 5.4 The 90^{o} spectrum for the $^{27}Al(p,\alpha_0)$ reaction at E_p = 1.365 MeV showing the pileup peak and the $^{19}F(p,\alpha_2)$ peak.

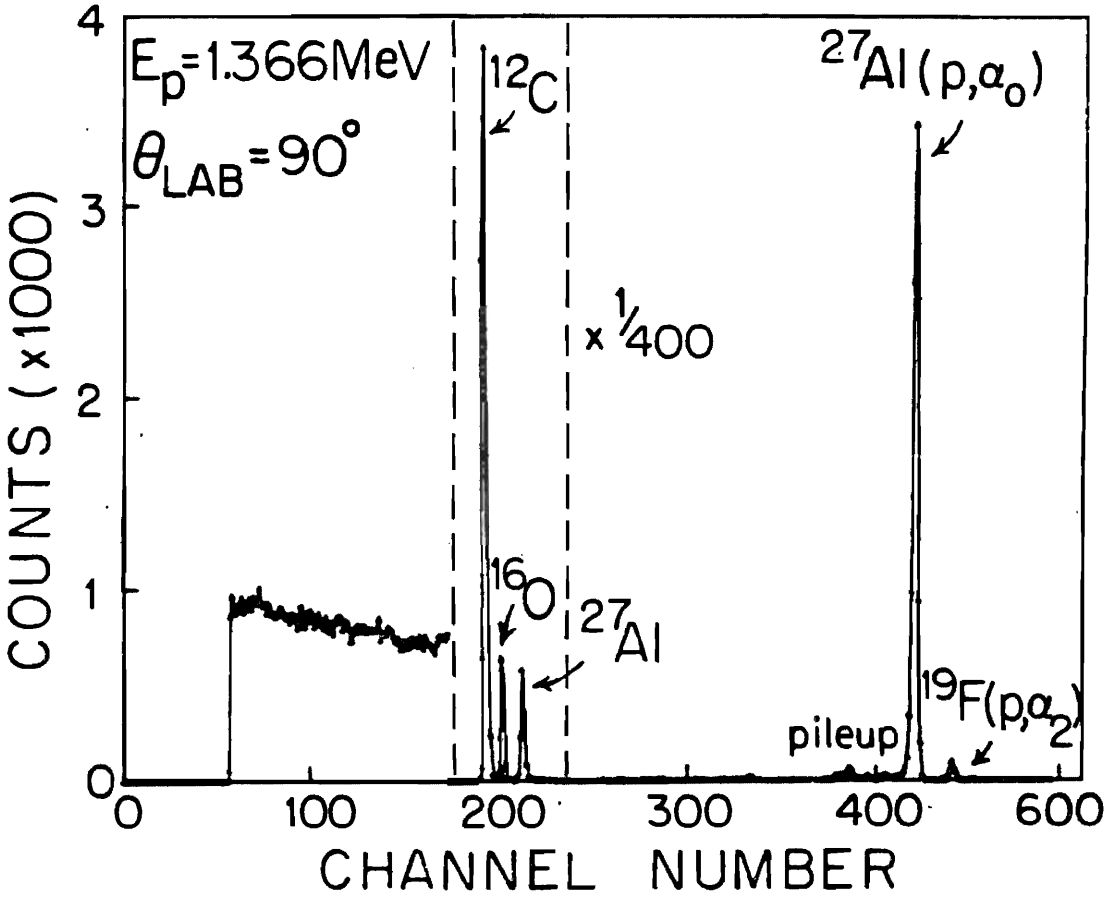
E_p=1.366MeV
θ_{LAB}=90°
^{12}C
$^{27}Al(p,\alpha_0)$
x 1/400
^{16}O
^{27}Al
pileup
$^{19}F(p,\alpha_2)$
COUNTS (x1000)
CHANNEL NUMBER
0
1
2
3
4
0
100
200
300
400
600

Figure 5.5 Angular distribution data and Legendre polynomial fit versus $\cos^2(\theta)$ for the $^{27}Al(p,\alpha_0)$ resonance at E_p = 1.365 MeV.

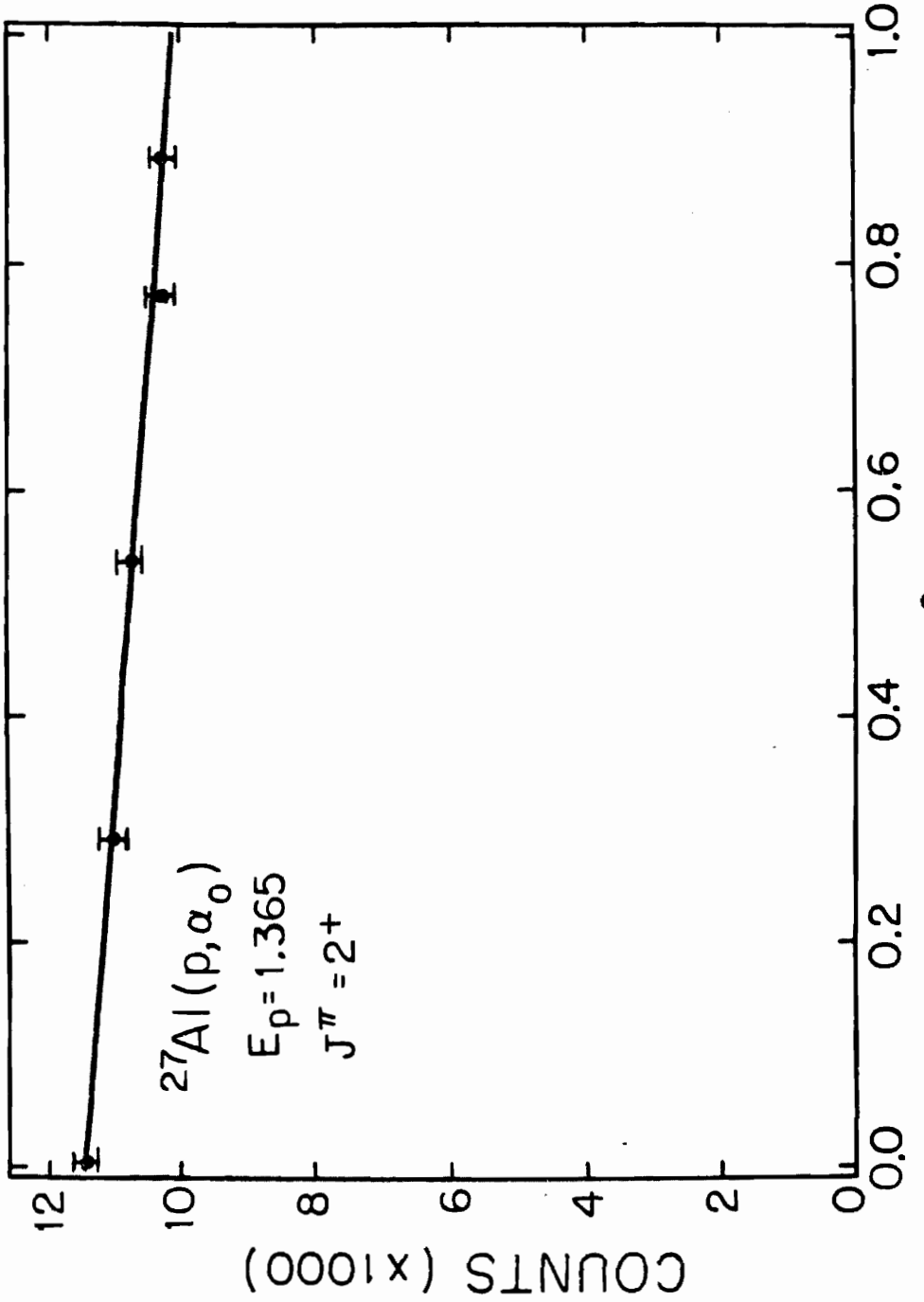
COUNTS (x1000)
0
2
4
6
8
10
12
0.0
0.2
0.4
0.6
0.8
1.0
cos² (θ)
27Al (p,α0)
Ep= 1.365
Jπ = 2+

$$a_2 = \frac{-\frac{15}{49}\varepsilon_2^2 - \frac{40}{49}\varepsilon_3^2 - \frac{2}{7}\sqrt{70}\cos(\bar{\phi}_0-\bar{\rho}_2)\varepsilon_2}{1+\varepsilon_2^2+\varepsilon_3^2}$$

and

$$a_4 = \frac{\frac{36}{49}\varepsilon_2^2 - \frac{9}{49}\varepsilon_3^2}{1+\varepsilon_2^2+\varepsilon_3^2}$$

where $\ell = 4$ has been neglected. Using the experimentally determined values for a_2 and a_4, and the value $\cos(\bar{\phi}_0 - \bar{\rho}_2) = -.22$ calculated for protons at 1.365 MeV with $r_0 = 1.25$ fm, two pairs of solutions are obtained.

$$\varepsilon_2 = -0.11,\ \varepsilon_3 = \pm 0.18 \text{ and } \varepsilon_2 = 0.28,\ \varepsilon_3 = \pm 0.54.$$

Notice that, as expected, the sign of the s = 3 amplitude is not determined. The elastic scattering data are used to choose between the two solutions for ε_2, since the difference in the amount of ℓ-mixing between the two solutions leads to different elastic scattering resonance shapes. Figure 5.6 shows the 160° data and R-matrix fits corresponding to the two solutions obtained above (the sign of the s = 3 amplitude does not affect the cross sections). The total width of the resonance was varied to achieve the best possible fit to the data for each solution. The fit in the upper figure is definitely better than that in the lower and thus the solution $\varepsilon_2 = -0.11$, $\varepsilon_3 = \pm 0.18$ is preferred. Thus the assumption by Driller et al. of $\varepsilon_2 = 0.1$ appears to have been a fortuitously good one, and their conclusions are unchanged.

Other resonances should be studied to further test for violations of detailed balance since it is possible that the TRI violating phases were large here but of nearly the same magnitude. This survey of resonances in ^{28}Si provides several other choices. Ideally, a resonance for which ε_2 is very large is desired. Unfortunately, such resonances are rare in the lower

Figure 5.6 The 160° data and R-matrix fits for the $J^{\pi} = 2^{+}$ resonance at E_p = 1.365 MeV. The fit in the top figure corresponds to the solution with $\varepsilon_2 = -0.11$, while the lower figure corresponds to the solution with $\varepsilon_2 = 0.28$.

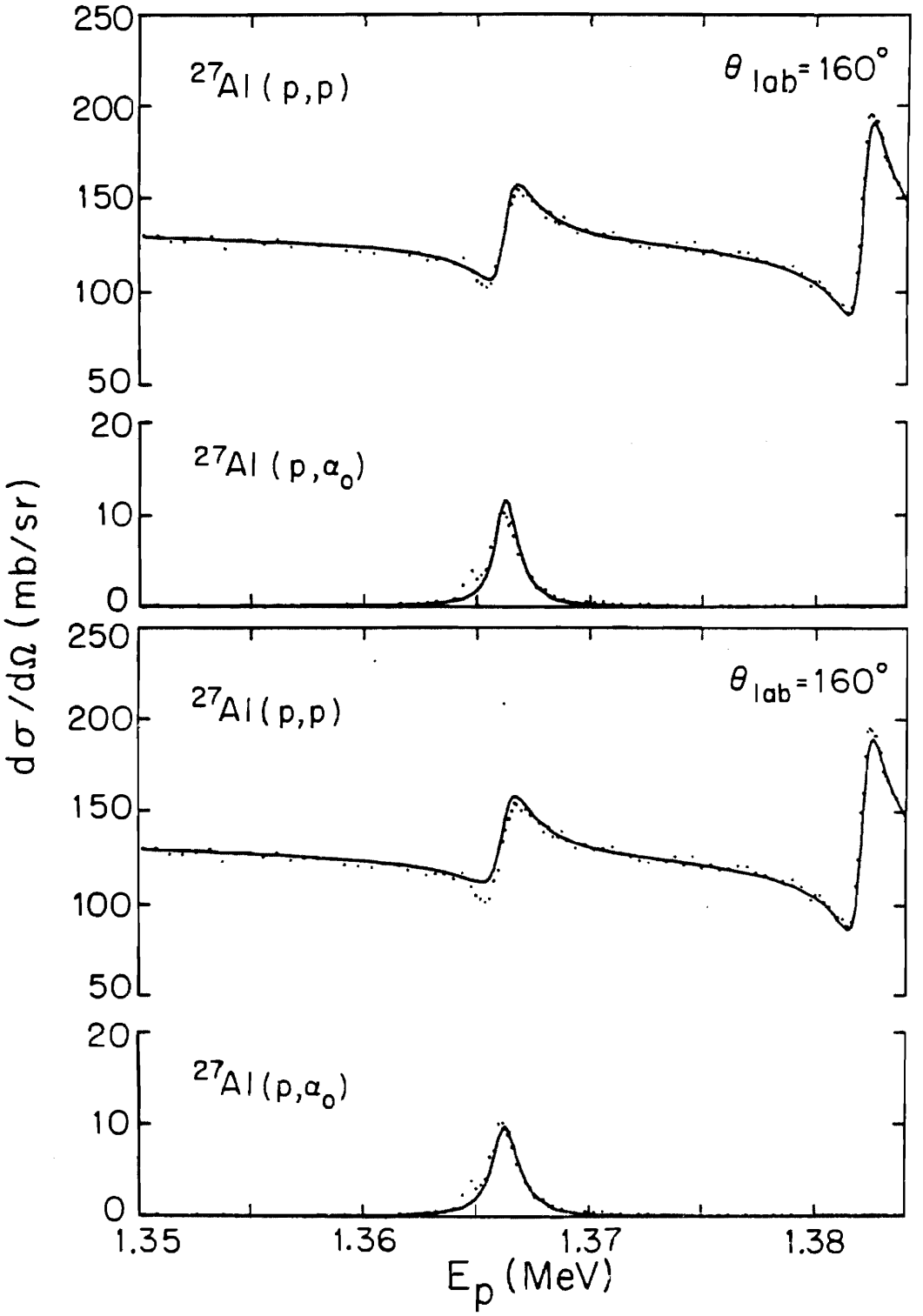
250
200
150
100
50
^{27}Al (p,p)
θ_{lab}= 160°
20
10
0
^{27}Al (p,α_0)
250
200
150
100
50
^{27}Al (p,p)
θ_{lab}= 160°
20
10
0
^{27}Al (p,α_0)
dσ /dΩ (mb/sr)
1.35
1.36
1.37
1.38
E_p (MeV)

energy region where the states are well isolated. Because the detailed balance experiments are difficult and tedious it seems important to first identify suitable resonances for further study. Thus accurate measurements of the coherent ℓ mixing for the $J^{\pi} = 2^{+}$ states should be carried out, and more (p,α) data should be obtained on other odd mass targets.

CHAPTER VI

SUMMARY

Differential cross sections were measured for $^{29}Si(p,p)$, (p,p_1), and (p,p_2) in the range E_p = 1.29 to 3.30 MeV, and for $^{27}Al(p,p)$, (p,p_1), (p,p_2), (p,α_0), and (p,α_1) in the range E_p = 0.92 to 3.05 MeV. Resonance parameters were extracted for 66 resonances in ^{30}P and for 104 resonances in ^{28}Si with a multi-level, multi-channel R-matrix analysis code; these parameters include resonance energies, spins and parities, partial elastic and reaction widths, and channel spin and orbital angular momentum mixing ratios.

The R-matrix theory was discussed as it relates to the present analysis, and the dependence of the resonance shapes on channel spin mixing and on ℓ-mixing were investigated for target nuclei with $J^\pi = \frac{1}{2}^+$ and $\frac{5}{2}^+$.

Seven analog states were identified in ^{30}P and eighteen analogs were identified in ^{28}Si. The extra complexity involved in calculating single particle widths and in comparing the spectroscopic strengths of the parent and analog states was examined.

Two applications of the spectroscopic results were described. The relation between the measured proton elastic scattering width of the 6^-, T = 1, stretched state in ^{28}Si and the strength of this state in intermediate energy inelastic scattering was outlined, and the relevance of a precise determination of the ℓ-mixing ratio to a previous test of time reversal invariance was discussed.

The results of the present study have demonstrated that the analysis of

proton elastic scattering from odd-mass targets is feasible. The acquisition of more proton resonance data with odd-mass targets will provide important spectroscopic information. This information will allow selection of resonances most suitable for more detailed study such as symmetry tests.

APPENDIX

THE HIGH RESOLUTION SYSTEMS

The basic accelerator and analyzer systems were described in chapter II. The operation of the present analyzer and homogenizer electronics is presented in section A of this appendix. In section B the recently completed terminal stabilizer system is discussed, and suggestions are made for its operation.

A. The Electrostatic Analyzer and Homogenizer Systems

The present double-sided analyzer-homogenizer system is shown in figure A.1. The basis for absolute energy measurement is provided by the calibrated voltage reference and associated Kelvin-Varley resistive divider in the Fluke digital differential voltmeter (DVM). The accuracy and stability of the analyzer for energy measurement depends upon accurate measurement of the voltage difference applied to the inner plate and the outer plate driver.

The Bertan positive and negative high voltage power supplies provide well regulated equal and opposite voltages which may be remotely controlled from a switch panel in the accelerator control room. Accurate and convenient measurement of the large voltages applied to the analyzer are made with the aid of precision resistive dividers. The dividers are shielded, have precision temperature coefficient compensated resistors, and are provided with anti-corona toroids. These features minimize voltage measurement errors which may be caused by stray electromagnetic fields,

Figure A.1 Block diagram of the high resolution system electronics.

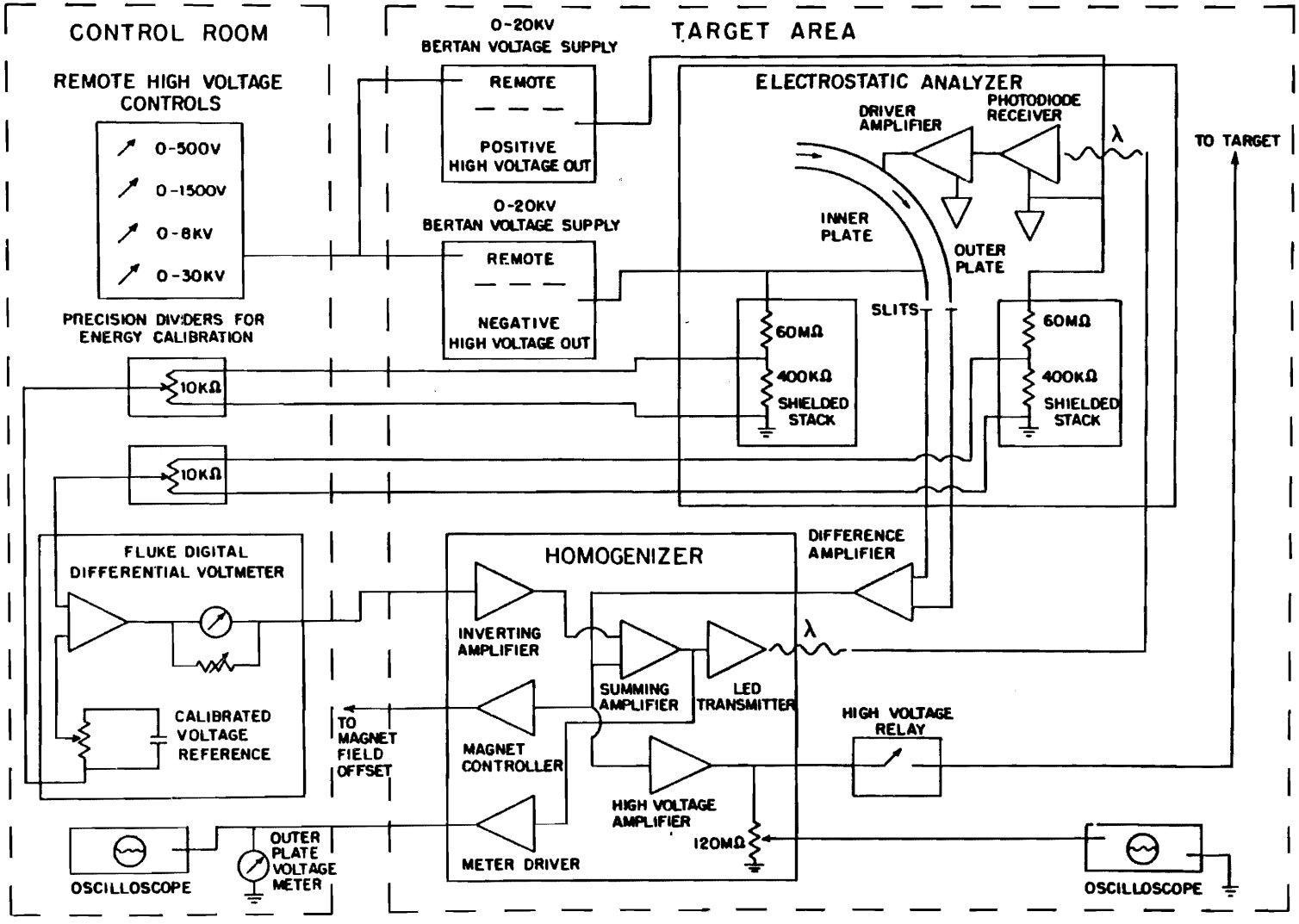
CONTROL ROOM
TARGET AREA
REMOTE HIGH VOLTAGE CONTROLS
0-500V
0-1500V
0-8KV
0-30KV
PRECISION DIVIDERS FOR ENERGY CALIBRATION
10KΩ
10KΩ
0-20KV BERTAN VOLTAGE SUPPLY
REMOTE
POSITIVE HIGH VOLTAGE OUT
0-20KV BERTAN VOLTAGE SUPPLY
REMOTE
NEGATIVE HIGH VOLTAGE OUT
ELECTROSTATIC ANALYZER
DRIVER AMPLIFIER
PHOTODIODE RECEIVER
λ
TO TARGET
INNER PLATE
OUTER PLATE
SLITS
60MΩ
400KΩ
SHIELDED STACK
60MΩ
400KΩ
SHIELDED STACK
FLUKE DIGITAL DIFFERENTIAL VOLTMETER
CALIBRATED VOLTAGE REFERENCE
HOMOGENIZER
DIFFERENCE AMPLIFIER
INVERTING AMPLIFIER
SUMMING AMPLIFIER
LED TRANSMITTER
λ
TO MAGNET FIELD OFFSET
MAGNET CONTROLLER
HIGH VOLTAGE RELAY
HIGH VOLTAGE AMPLIFIER
120MΩ
METER DRIVER
OSCILLOSCOPE
OUTER PLATE VOLTAGE METER
OSCILLOSCOPE

temperature changes, and corona current.

As mentioned in chapter III, the ratio of the analyzer voltage difference to the energy is 1 to 111. The voltage on each analyzer plate is divided by $10^6/111 = 9009$, so that the voltage difference measured by the Fluke DVM equals 10^{-6} times the beam energy. Thus if the system has been calibrated on the $^{44}Ca(p,p)$ resonance at $E_p = 1.8840$ MeV, the DVM will read 1.8840 V. For energies away from the calibration point, minor corrections must be made for relativistic effects. These corrections are given by Westerfeldt (1977) for the single-sided analyzer system, thus his correction equations include a term for the acceleration of the beam into the analyzer due to the non-zero potential at the entrance. The corresponding equations for double-sided operation are given by Adams (1983). For double-sided operation the net potential due to the voltages on the analyzer plates is zero and there is no acceleration of the beam into the analyzer. This assumes that the voltages are actually equal and that the beam is entering the center of the analyzer.

Occasionally energy calibration of the analyzer system is necessary. Possible causes for recalibration are: slight changes in the analyzer plate separation (from vibration or temperature changes), changes in the resistive dividers (from temperature changes or aging), or drifting of the tolerances in the DVM. When a change of calibration is made, both of the calibration potentiometers should be changed in equal increments to preserve the two divider ratios and hence the equality of the analyzer voltages. As a check, the dividers may be matched in value by connecting the same potential to both plates and nulling the DVM with the calibration potentiometers.

Any drift in the Bertan power supplies will cause the DVM to go off of null. To correct for this without affecting the beam energy the recorder output of the DVM is fed back through an inverting amplifier to the outer

plate to keep the analyzer voltage difference constant and the beam centered.

The difference amplifier is a Princeton Applied Research (PAR) model 113 low noise, linear preamplifier. The analyzer slit currents are converted to voltages by resistors, and the voltages are amplified by the PAR. The PAR has adjustable gain and low and high pass filters. Since DC stability is required, the low pass filter is always set at DC. The high pass filter and the gain are adjusted as high as possible without causing the system to oscillate. Usually the high frequency roll-off was set at 300 Hz, while the gain varied from 100 to 5000 depending upon the slit resistors in use and the amount of analyzer beam.

Because the magnitude of the voltages produced by the slit resistors depend upon the beam intensity on the slits, the feedback gain is affected by intensity fluctuations of the beam. Long term changes in the beam intensity such as a decrease in transmitted beam due to changing beam optics will result in lower feedback gain unless the gain of the PAR is changed. Conversely, an increase in transmitted beam results in increased feedback gain and feedback oscillations may occur, requiring the operator to lower the PAR gain. In addition, faster intensity fluctuations from ion source instabilities will result in spurious correction signals.

Recently these problems have been overcome through the design and construction of an automatic-gain-control (AGC) preamplifier. This preamplifier employs an Analog Devices integrated circuit divider to produce an output proportional to the slit current difference divided by the total slit current. This produces a correct difference signal independent of the beam intensity so the feedback gain need only be set once. Ideally the difference amplifier output should be a linear function of the beam position. For a pair of vertical slits and with the beam profiles normally

obtained, some nonlinearity is introduced. The AGC preamplifier eliminates the nonlinear characteristics of the slit system due to the non-uniformity of the beam current density.

The output of the difference amplifier is summed with the DVM recorder output signal and is applied via an optical fiber system to the outer plate driver amplifier. The optical fiber system is necessary due to the high potential on the analyzer outer plate. The fiber optics system consists of a Math Associates XA-1000 light emitting diode transmitter and an RA-1000 photodiode receiver, connected with a Belden 100 μm diameter fiber optic cable. The transmitter incorporates optical feedback to achieve excellent DC stability. The transmitter and receiver pair have a bandwidth of DC to 5 MHz.

The receiver and associated driver amplifier are both floating at the outer plate potential. They receive their power from an isolation transformer. The fiber optics system is adjusted for unity gain, while the driver amplifier has a gain of 10.

Once the difference signal is returned to the outer plate the feedback loop is closed and the difference signal will represent a true measure of the energy fluctuations of the beam. These are the energy fluctuations to be corrected, thus the signal is amplified by a high voltage amplifier and applied to the target rod.

The design of the high voltage amplifier has recently been changed. The current version uses a triode as a class A amplifier with negative feedback to stabilize the gain at 111. The new high voltage amplifier operates at lower plate currents than the previous one, allowing the use of a lower wattage plate resistor, and reducing the danger from electric shock.

The calibration of the high voltage amplifier is made by driving the difference amplifier with a low frequency (~ 15 Hz) sinusoidal signal. The

outer plate voltage and the target rod voltage are measured at several different amplitudes of the input signal and a plot is made of the target rod voltage versus the outer plate voltage. The high voltage gain is adjusted to achieve a slope of 111.

The difference amplifier signal is also sent to the magnet controller, a low pass (< . 02 Hz) amplifier, which is connected to the field offset input of the magnet power supply. If the plate voltage on the analyzer is changed, the beam moves off center generating a difference signal. This signal changes the magnet current and, through the corona circuit, forces a change in the accelerator energy. This feedback system allows the entire system to be controlled by the analyzer high voltage power supplies and the DVM over a limited energy range of about 20 keV.

Finally, the summing amplifier output and the target rod signal are sent to buffer amplifiers to drive oscilloscopes in the control room and the target area. The summing amplifier signal also drives a meter in the control room to indicate the DC signal on the outer plate.

Currently an automated data aquisition system is being designed. Implementation of this system should improve the reliability of the data and make operation of the system easier. The major changes necessary for automated operation include: (1) replacement of the old Fluke DVM with a new highly accurate programmable Fluke DVM, (2) addition of a computer interface for the Bertan high voltage power supplies, including a sample and hold feedback system which will replace the present analog feedback from the DVM recorder output, (3) replacement of the present magnet power supply with a programmable power supply and a Hall probe interface. It is hoped that such a system can be installed in the near future.

B. The Terminal Stabilizer System

As mentioned in chapter III, a terminal stabilizer similar to the one designed by Bloch (1968) has been constructed. The goals in designing the system were: (1) the weight was to be less than 5 kg to avoid loading the accelerator column, (2) the components were to withstand cycling of the ambient pressure from 0 psia (vacuum) to 320 psia, (3) the system should be resistant to damage from vibration and tank sparks, and (4) normal accelerator operation must be possible when the terminal stabilizer is off. Although testing of the system is not complete it appears that these goals have been achieved.

The terminal stabilizer circuits are shown in figures A.2 and A.3. The power supplies shown in figure A.2 provide the necessary DC and AC voltages for operation of the amplifier circuits. The 6.3 V transformer powers the tube filaments and is rectified to provide 4.5 VDC for the shorting relay on the output. The 486 V transformer with rectification and filtering provides the plate voltage for the 12AX7 triode. Transient protection and regulation are provided in the 15 VDC power supply to protect the solid state components of the photodiode receiver. A time delay relay (TD060 with 60 s delay) and the KRP14AG relay ensure that the 5.8 kVDC supply is not energized until the tube filaments are hot. The output also remains shorted by the high voltage reed relay until the high voltage is energized. The reed relay protects the output circuit when the system is not in use and allows normal accelerator operation. The AC supply lines are provided with surge suppressors (s.s.) to help protect the stabilizer from sparks.

The high voltage amplifier (figure A.3) consists of a 12AX7 triode driving the grid of a cathode biased 8755 triode. Both of the triodes are operated as class A amplifiers. Although the 8755 triode is operated far below its rated plate current, good linearity of the plate current versus grid voltage is characteristic of this tube. The low frequency roll-off of

Figure A.2 Schematic diagram of the terminal stabilizer power supplies.

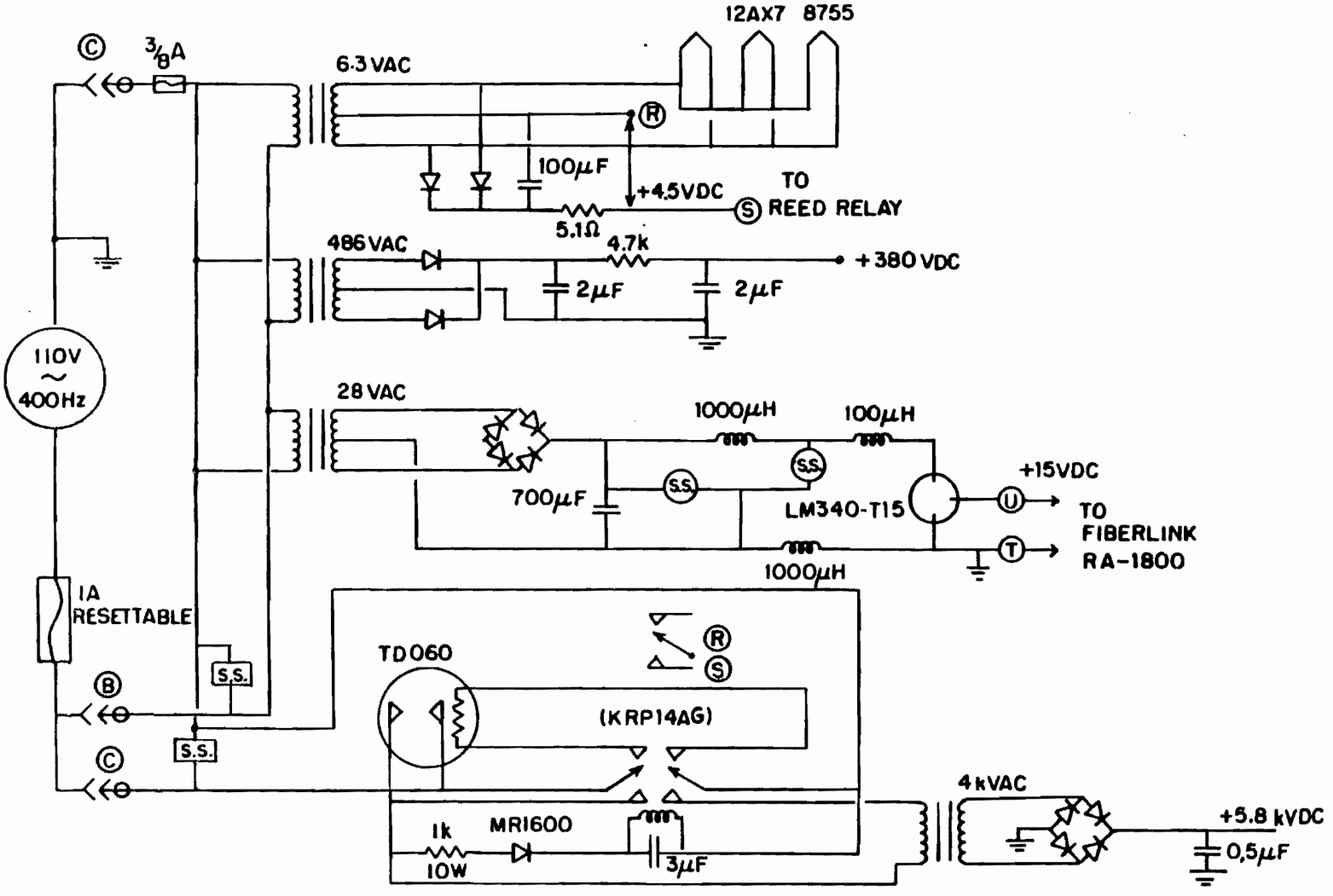
12AX7 8755
6.3 VAC
100μF
+4.5VDC
TO
REED RELAY
5.1Ω
486 VAC
4.7k
+380 VDC
2μF
2μF
110V
~
400Hz
28 VAC
1000μH
100μH
700μF
+15VDC
LM340-T15
TO
FIBERLINK
RA-1800
1000μH
1A
RESETTABLE
TD060
(KRP14AG)
4 kVAC
+5.8 kVDC
1k
10W
MR1600
3μF
0,5μF

Figure A.3 Schematic diagram of the terminal stabilizer high voltage amplifier.

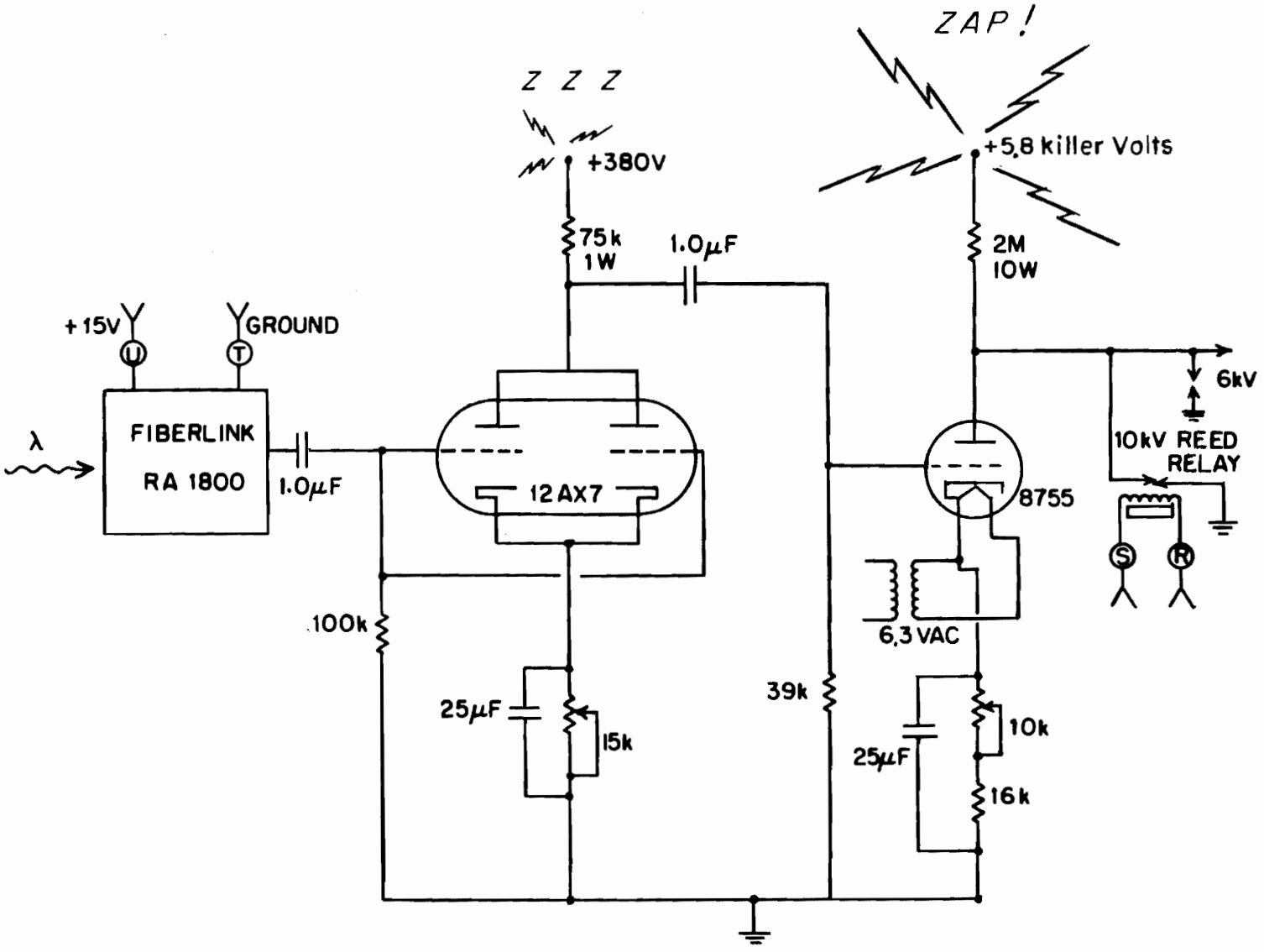
ZAP!
Z Z Z
+380V
+5.8 killer Volts
75k
1W
1.0μF
2M
10W
+15V
GROUND
U
T
λ
FIBERLINK
RA 1800
1.0μF
12AX7
8755
6kV
10kV REED
RELAY
S
R
100k
6.3 VAC
39k
25μF
15k
25μF
10k
16k

the amplifier is about 30 Hz. The high frequency roll-off is around 1 kHz when the system is coupled to the RF source.

The system is similar to the terminal stabilizer installed in the TUNL FN Tandem Van de Graaff accelerator. Terminal stabilizer systems provide negative feedback at the accelerator dome to reduce the beam energy fluctuations at the accelerator. In the present system the feedback signal from a pair of slits in located front of the scattering chamber is amplified and transmitted via an optical fiber to a receiver in the terminal of the accelerator. At the terminal the signal is amplified by a high voltage amplifier and applied to the RF ion source with respect to the dome. With negative feedback, the beam energy fluctuations are reduced as the beam leaves the ion source.

To keep the terminal stabilizer from competing with the corona feedback circuit the high frequency roll-off of the corona circuit and the low frequency roll-off of the terminal stabilizer system should cross over at around 30 Hz. The corona circuit removes low frequency energy fluctuations and the terminal stabilizer removes higher frequency ($<$ 1 kHz) fluctuations. The feedback signal for the terminal stabilizer is taken from the experimental beam line rather than the corona slits to take advantage of the greater dispersion available in front of the scattering chamber. The correction signal from the analyzer should not be used with the stabilizer unless the analyzer feedback is disabled (with the loss of DC stability except for that provided by the corona control), otherwise the two systems will compete, resulting in degraded performance.

BIBLIOGRAPHY

Adams, G. "Proton Resonance Spectroscopy in ^{26}Al." M.S. thesis, North Carolina State University, 1983.

Barnard, R.W. and Jones, G.D. Nucl. Phys., A108, 641 (1968).

Biedenharn, L.C., Blatt, J.M. and Rose, M.E. Rev. Mod. Phys. 24, 249 (1952).

Bilpuch, E.G., Lane, A.M., Mitchell, G.E. and Moses, J.D. Phys. Reports 28, 145 (1976)

Bloch, R., Pixley, R.E., Reichart, W. and Zamboni, F. Nucl. Instrum. and Methods 59, 325 (1968).

Browne, J.C. "Fine Structure of Analog States in ^{61}Cu, ^{63}Cu, and ^{65}Cu." Ph.D. dissertation, Duke University, 1969.

Chandler, J.R. "Channel Spin Mixing Ratios in High Resolution Proton Inelastic Scattering on ^{46}Ti." Ph.D. dissertation, North Carolina State University, 1978.

Condon, E.U. and Shortley, G.H. The Theory of Atomic Spectra. Cambridge: Cambridge University Press, 1951.

Cseh, J., Koltay, E., Máté, Z., Somorjai, E. and Zolnai, L. Nucl. Phys. A385, 43 (1982).

Devons, S., and Goldfarb, L.J.B. "Angular Correlations" in Handbuch der Physik, Vol. 42, 1957.

Driller, H. Blanke, E., Genz, H., Richter, A., Schrieder, G. and Pearson, J.M. Nucl. Phys. A317, 300 (1979).

Endt, P.M. and Van der Leun, C. Nucl. Phys. A310, 1 (1978).

Halderson, D., Kemper, K.W., Fox, J.D., Nelson, R.O., Bilpuch, E.G., Westerfeldt, C.R. and Mitchell, G.E. Phys. Rev. C24, 786 (1981).

Harney, H.L. and Weidenmüller, H.A. Nucl. Phys. A139, 241 (1969).

Harris, G.I., Hyder, A.K., Jr. and Walinga, J. Phys. Rev. 187, 1413 (1969).

Hemsky, J.W., Ling, S.C. and Wolfe, P.J. Phys. Rev. C8, 192 (1973).

Huby, R. Proc. Phys. Soc. A67, 1103 (1954).

Jahnke, E., Emde, F. and Lösch, F. Tables of Higher Functions. New York: McGraw-Hill, 1960.

Kapur, P.L. and Peierls, R.E. Proc. Roy. Soc. A166, 277 (1938).

Keyworth, G.A. "A High Resolution Study of Isobaric Analogue States in ^{41}K and ^{23}Na." Ph.D. dissertation, Duke University, 1968.

Lane, A.M. and Thomas, R.G. Rev. Mod. Phys. 30, 257 (1958).

Lindgren, R.A. "Very High Magnetic Multipolarity Transitions (M4 to M14) to Stretched Particle-Hole States" in Bertrand, F.E. Giant Multipole Resonances Nucl. Sci. Research Conference Series, 1 (1979).

Maas, J.W., Somorjai, E., Graber, H.D., Van den Wijngaart, C.A., Van der Leun, C. and Endt, P.M. Nucl. Phys. A301, 213 (1978).

Marion, J.B., Rev. Mod. Phys. 38, 660 (1966).

Mitchell, G.E., Bilpuch, E.G., Shriner, J.F., Jr. and Lane, A.M. "Amplitude Correlations in Nuclear Resonance Spectroscopy," to be published (1983).

Moon, P.B. and Tillman, R. Proc. Roy. Soc. 153, 421 (1936).

Outlaw, D.A. "A High-Resolution Study of Proton Resonances in ^{31}P, ^{35}Cl, and ^{93}Tc." Ph.D. dissertation, North Carolina State University, 1974.

Outlaw, D.A., Mitchell, G.E. and Bilpuch, E.G. Nucl. Phys. A269, 99 (1976).

Parks, P.B., Newson, H.W. and Williamson, R.M. Rev. Sci. Instrum. 29, 834 (1958).

Pearson, J.M. and Richter, A. Phys. Lett. 56B, 112 (1975).

Poirier, C.P., Walinga, J., Manthuruthil, J.C. and Harris, G.I. Phys. Rev. C1, 1982 (1970).

Roush, M.L., West, L.A. and Marion, J.B. Nucl. Phys. A147, 235 1970.

Sales, K.B. "A High Resolution Study of Proton Resonances in ^{65}Ga and ^{67}Ga" Ph.D. dissertation, North Carolina State Univesity, 1980.

Sellin, D.L. "Excited States in ^{19}F." Ph.D. dissertation, Duke University, 1968.

Snover, K.A., Feldman, G., Hindi, M.M., Kuhlmann, E., Harakeh, M.N., Sasao, M., Noumachi, M., Fujita, Y., Fujiwara, M. and Hosono, K. Phys. Rev. C27, 993 (1983).

Tveter, A. Nucl. Phys. A185, 433 (1972).

Vorona, J., Olness, J.W., Haeberli, W. and Lewis, H.W. Phys. Rev. 116, 1563 (1959).

Wapstra, A.H. and Bos, K. Atomic and Nucl. Data Tables 19, 175 (1977).

Watson, W.A. "A High Resolution Study of Proton Resonances in ^{57}Co." Ph.D. dissertation, Duke University, 1980.

Wells, W.K. "High Resolution Proton Inelastic Scattering on ^{56}Fe and ^{48}Ti." Ph.D. dissertation, Duke University, 1978.

Westerfeldt, C.R. "A High Resolution Study of Proton Resonances in ^{27}Al." M.S. thesis, North Carolina State University, 1977.

Westerfeldt, C.R. private communication (1981).

Wigner, E.P. Phys. Rev. 70, 15 (1946).

Wigner, E.P. Phys. Rev. 70, 606 (1946).

Wigner, E.P. and Eisenbud, L. Phys. Rev. 72, 29 (1947).

Wilkerson, J.F. "Isospin Mixing in Light Nuclei." Ph.D. dissertation, University of North Carolina, 1982.

Wilson, W.M. "A High Resolution Study of Proton Resonances in ^{41}Sc, ^{43}Sc, and ^{45}Sc." Ph.D. dissertation, Duke University, 1973.

Wimpey, J.F. "Electromagnetic Decay of Fragmented Analogue States in ^{45}Sc and ^{63}Cu." Ph.D. dissertation, North Carolina State University, 1974.

Yang, C.N. Phys. Rev. 74, 764 (1948).

BIOGRAPHY

RONALD OWEN NELSON

Personal: Born August 16, 1956, Austin, Texas

Education: B.A. in Physics, Florida State University, 1978

Positions: Teaching Assistant, 1978-1979
Research Assistant, 1979-present

Abstracts:

"A High Resolution Study of the ^{29}Si(p,p) Reaction," C.R. Westerfeldt, R.O. Nelson, E.G. Bilpuch, G.E. Mitchell, and K.B. Sales, Bull. Am. Phys. Soc. 25, 596 (1980).

"A High Resolution Study of Proton Resonances in ^{28}Si," R.O. Nelson, E.G. Bilpuch, C.R. Westerfeldt, and G.E. Mitchell, Bull. Am. Phys. Soc. 26, 1222 (1981).

"Levels of ^{30}P from High Resolution Proton Scattering," R.O. Nelson, C.R. Westerfeldt, E.G. Bilpuch, and G.E. Mitchell, Bull. Am. Phys. Soc. 27, 712 (1982).

"Statistical Properties of $3/2^+$ Resonances in ^{49}V," J.F. Shriner, Jr., E.G. Bilpuch, R.O. Nelson, C.R. Westerfeldt, P. Ramakrishnan, B.H. Chou, and G.E. Mitchell, Bull. Am. Phys. Soc. 27, 712 (1982).

Articles:

"Width of the 6^-, T=1, E_x=14.36 MeV State in ^{28}Si and Its Relationship to Intermediate Energy Inelastic Scattering," Dean Halderson, K.W. Kemper, J.D. Fox, R.O. Nelson, E.G. Bilpuch, C.R. Westerfeldt, and G.E. Mitchell, Phys. Rev. C24, 786 (1981).

"Proton Resonances in ^{30}P," R.O. Nelson, E.G. Bilpuch, C.R. Westerfeldt, and G.E. Mitchell, Phys. Rev. C27, 930, (1983).

"Statistical Properties of $3/2^+$ Resonances in ^{49}V," P. Ramakrishnan, B.H. Chou, G.E. Mitchell, E.G. Bilpuch, R.O. Nelson, J.F. Shriner, Jr., and C.R. Westerfeldt, Z. Phys. A311, 157 (1983).

Memberships: American Physical Society
Sigma Pi Sigma

ERRATA

p9, in the third and fourth equations replace F_c with iF_c.

p15, in the first equation the summation should be over $(2s+1)d\sigma_{\alpha s,\alpha' s'}/d\Omega$.

p48, first line should end "... barn/sr".

p65, third paragraph, change 2.7 to 2.4 MeV.

p66, in table 4.2 for $J^\pi = 5^-$ and p_0 add $\ell = 3$, $s = 3$.

p106, the end of footnote e should read "eqn. 2.3".

pp114-23, replace tables 4.9, 4.10, and 4.11 with the data published in Phys. Rev. C 29, 1656 (1984) table I and 30, 755 (1984) tables II, III, and IV.

p130, in fig. 4.20 add left parenthesis to E_p(MeV).

p165, in table 5.1 the column label S_p should be $(2T_z+1)S_p$.

pp166-7, replace table 5.2 with the data published in Phys. Rev. C 29, 1656 (1984) table III and 30, 755 (1984) table V.

p176, paragraph 2 replace ε_3 with δ_3 where $\delta_3^2 = \Gamma_{\ell+2,s=3}/\Gamma_{\ell,s=2}$.

p178, in fig. 5.4 change 600 to 500 on the abcissa.

p181, paragraph one, change ε_3 to δ_3 in all equations and text. Add: $\delta_3^2 = \Gamma_{\ell+2,s=3}/\Gamma_{\ell,s=2}$.

p191, paragraph 3, line 2 should read, "depends upon ... "

p199, paragraph 2, line 5 should read, "slits located in front of ... "

R.O. Nelson
December 1984